LOAD FLOW SOLVERS
FOR DC AND HYBRID AC/DC GRIDS

ZAHID JAVID

PhD

The Hong Kong Polytechnic University

2024

The Hong Kong Polytechnic University

Department of Electrical and Electronics Engineering

Load Flow Solvers for DC and Hybrid AC/DC Grids

ZAHID JAVID

A thesis submitted in partial fulfillment of the requirements for the degree of Doctor of Philosophy

August 2023

CERTIFICATE OF ORIGINALITY

I hereby declare that this thesis is my own work, to the best of my knowledge and belief. It reproduces no material previously published or written, nor material that has been accepted for the award of any other degree or diploma, except where due acknowledgment has been made in the text.

________________________ (Signed)

Zahid Javid (Name of Student)

Abstract

The main objective of this dissertation is the establishment of fast and robust power flow (PF) solvers for DC and hybrid AC/DC distribution networks. The developed PF solvers can employ all types of converters and handle any arbitrary DC and hybrid AC/DC network configurations. All PF solvers are tested on various test systems for different loading conditions and R/X ratios of the AC lines. The accuracy of the PF solutions is validated with Electromagnetic Transient (EMT) simulations.

First the DC/DC converter models are developed for DC PF solution and integrated into DC PF solvers. The Laplacian Matrix (LM) based DC PF solvers offer the widest convergence range. The convergence and PF solution uniqueness of LM based DC PF solvers are demonstrated with the Banach Fixed Point Theorem (BFPT) using contraction mapping. However, they are non-derivative PF solvers and their computational speeds are well below then the DC PF solver which uses modified augmented nodal analysis (MANA) formulation and Newton Raphson (NR) algorithm (MANA-DC). The uniqueness of solution and the conditions for guaranteed convergence of MANA-DC are derived using the Kantorovich's theorem. The calculated guaranteed convergence range of MANA-DC PF solver for the test networks is also well above the practical loading conditions. The Holomorphic Embedding PF (HE-PF) solver is the slowest one.

This thesis also developed AC/DC converter models and applied the MANA formulation to obtain a unified PF solver for hybrid AC/DC networks. The proposed PF solver does not need the existence of a DC slack bus, nor does it have network topology constraints. The superior convergence characteristics of the MANA with NR (MANA-NR) over the classical nodal analysis (NA) with NR (NA-NR) is illustrated through simulations and explained by inspecting the condition number of the Jacobian matrix. The formulation is further extended to include solid-state transformer (SST) model (MANA-SST) and the accuracy is validated with OpenDSS model available in literature.

Acknowledgments

First, I am thankful to almighty Allah for his countless blessings on me.

Dr. Karaagac Ulas, my research supervisor and excellent mentor, deserves my heartfelt thanks for his extreme patience, technical expertise, continuous mentorship, opportunities he generated, and selecting me as a PhD student.

I am grateful to Professor Ilhan Kocar for the technical knowledge, wise guidance, and support. I would also like to thank Professor William Holderbaum for his insightful talks and encouragement.

I would like to thank my parents and my wife for their unwavering support and encouragement.

I want to acknowledge the financial support from Hong Kong PhD Fellowship Scheme (HKPFS) for my PhD.

Finally, I would like to thank all my PolyU friends.

TABLE OF CONTENTS

List of PhD Publications

[1] **Z. Javid**, U. Karaagac, I. Kocar, and K. W. Chan, "Laplacian matrix-based power flow formulation for LVDC grids with radial and meshed configurations," *Energies,* vol. 14, no. 7, p. 1866, 2021.

[2] **Z. Javid**, U. Karaagac, and I. Kocar, "Improved Laplacian Matrix based power flow solver for DC distribution networks," *Energy Reports,* vol. 8, pp. 528-537, 2022.

[3] **Z. Javid**, U. Karaagac, and I. Kocar, "MANA Formulation Based Load Flow Solution for DC Distribution Networks," *IEEE Transactions on Circuits and Systems II: Express Briefs, 2023*. *early access article*, doi: 10.1109/TCSII.2023.3238132.

[4] **Z. Javid**, T. Xue, U. Karaagac, and I. Kocar, "Efficient Graph Theory Based Load Flow Solver for DC Distribution Networks Considering DC/DC Converter Models," presented at the 9th International Conference on (PESA) Power Electronics Systems and Applications 2022, Hong Kong, 22/9, 2022, 7143.

[5] **Javid, Z.**, Xue, T., Karaagac, U. and Kocar, I., "Unified Power Flow Solver for Hybrid AC/DC Distribution Networks," *IEEE Transactions on Power Delivery* (2023). *early access article,* doi: 10.1109/TPWRD.2023.3271311.

[6] **Z. Javid**, U. Karaagac, I. Kocar, and T. Xue, "DC Grid Load Flow Solution Incorporating Generic DC/DC Converter Topologies," *Enery Reports, 9 (2023): 951-961.*

[7] **Z. Javid**, U. Karaagac, I. Kocar, and W. Holderbaum, "Future Distribution Grids: A Review, submitted in : *International Journal of Electrical Power & Energy Systems.*

[8] **Z. Javid**, U. Karaagac, I. Kocar, and W. Holderbaum, "Solid-State Transformer Modelling in Power Flow Calculation," *Energy Reports, accepted paper,* to be published in 2023.

List of Figures

List of Tables

List of Abbreviations

AC:	Alternating Current
AVM:	Average Value Model
BESS:	Battery Energy Storage System
BFS:	Backward/Forward Sweep
BFPT:	Banach Fixed-point Theorem
CCL:	Constant Current Load
CCM:	Continuous Conduction Mode
CPL:	Constant Power Load
CRL:	Constant Resistive Load
DC:	Direct Current
DN:	Distribution Network
DG:	Distributed Generator
ESS:	Energy Storage System
EV:	Electric Vehicle
e-ILM:	Extended Improved Laplacian Matrix
EMT:	Electromagnetic Transients
FS:	Flat Start
GS	Gauss Seidel
HE-PFM:	Holomorphic Embedding Power Flow Method
HVAC:	High Voltage Alternating Current
HVDC:	High Voltage Direct Current
IBR:	Inverter-Based-Resource
ILM:	Improved Laplacian Matrix
KCL:	Kirchoff Current Law
KVL:	Kirchoff Voltage Law
LV:	Low Voltage
LCC:	Line Commutating Converter
LM:	Laplacian Matrix
MT-DC:	Multi-terminal DC
MV:	Medium Voltage
MG:	Microgrid
MNA:	Modified Nodal Analysis
MANA:	Modified Augmented Nodal Analysis
M-DC-SST:	Multiport DC SST
NCE:	Non-constitutive Elements
NR:	Newton Raphson

NA:	Nodal Analysis
PV:	Photovoltaics
POI:	Point of Interconnection
PFA	Power Flow Analysis
PF:	Power Flow
RES:	Renewable Energy Source
SST:	Solid-state Transformer
TS:	Tune Start
TSE	Taylor Series Expansion
UTM	Upper Triangular Matrix
VSC:	Voltage Source Converter
V2G:	Vehicle to Grid
WT:	Wind Turbine

List of Symbols

A_1, A_2, A_3:	Network Block Matrices (represent the voltage-current relationship of the NCEs)
a, b, c:	Load Characteristic Coefficients
B:	Bus Type
BT:	Binary Bus Type Vector for Buck-Boost Converter
C:	Connectivity Matrix
C_v:	Column of Connectivity Matrix for Ideal Voltage Sources
C_d:	Connectivity Matrix of Constant Power Buses
D:	Duty Cycle Ratio of DC/DC converter
E:	Binary Line Type Matrix for DC/DC Converter Operation
f_L, f_d:	Load Constraint/Demand Constraint
f_v:	Ideal Voltage Source Constraint
f_{kcl}:	Network Power Balance Constraint
G:	Conductance Matrix
G_{aug}:	Augmented Conductance Matrix
H:	Incidence Matrix
I_{sc}:	Short Circuit Current
I_{cpt}:	Augmented Vector of Currents of Constant Power Terminals
I_{gen}:	Augmented Vector of Currents of Generator Buses
I_{PQ}:	Augmented Vector of Currents for PQ Loads
J:	Jacobian Matrix
K:	Binary Bus Type Vector for Buck Converter
L:	Binary Line Type Matrix for AC/DC Line
M:	Modulation index of VSC
m:	Sending Bus
n:	Receiving Bus
N:	Total Number of Buses
P:	Active Power
Q:	Reactive Power
$\mathcal{R}_{thv}$:	Thevenin Equivalent Resistance
$\mathfrak{R}_{\mathrm{p}}$:	Primitive Resistive Matrix
T:	Binary Bus Type Vector for Boost Converter
t:	Iteration Counter
U:	Unity Vector
W:	Vector of Independent Voltage Sources
x:	Vector of State Variables

Y:	Admittance Matrix
Y_{aug}:	Augmented Admittance Matrix
α, β:	Converter Efficiency Coefficients
ς:	Converter Constant.
η_c:	Converter Efficiency
η_{SST}:	SST Efficiency
φ_c:	Converter Power Factor Angle
θ:	Bus Voltage Angle
λ:	Load Type
ρ:	Maximum Load
Φ:	Laplacian Matrix
Ψ:	Contraction Constant of BFPT
ξ:	Lipschitz Inequality
σ:	Boundary Value of the Network
δ:	Newton`s Basin of Attraction
$\gamma,\ \bar{\gamma}$:	Binary Coefficients of Battery Charging and Discharging
$\tau,\ \bar{\tau}$:	Binary Coefficients of EV Charging and Discharging
Γ:	Binary Bus Type Vector for AC or DC Bus

CHAPTER 1. Introduction

1.1 Recent Trends in Power System

There have been numerous developments in power distribution systems throughout the globe. One of them involves reducing the carbon footprint by integrating renewable energy sources (RESs), such as wind and solar. The distribution networks (DNs) are undergoing a transformation into active networks, establishing bidirectional power flows, and paving the way for the integration of distributed energy resources based on RESs and the implementation of the smart grid in practice. Recently, there is an open debate on whether to use alternating current (AC) or direct current (DC) in DNs. This matter can be traced back to the heated dispute gushed around the start of the twentieth century, on the best method for generating, transmitting, and distributing electrical power. This conflict, known as the "War of Currents," was waged between G. Westinghouse and N. Tesla, supporting AC, versus T. Edison, an ardent supporter of DC. The argument was settled by the universal adoption of AC system for reasons that made perfect sense at the time [1]. The advent of transformers, which offered a simple and effective way of changing the AC voltage levels, was one of the reasons. The DC technology was not matured enough at that time to change voltage levels for transmission and distribution [2]. AC system utilization has become the standard for more than a century due to (a) the ease of changing voltage levels using transformers and (b) the development of machines based on poly-phase AC systems. Nevertheless, it would be prudent to regularly re-evaluate our engineering methods. In fact, such re-evolution on paradigm shift led to the efficient and cost-effective high voltage DC (HVDC) transmission system over long distances [3]. HVDC transmission has established its merit in the modern power system. The HVDC transmits more power than high voltage AC (HVAC) as HVDC lines can carry higher voltage with the same wire thickness (no skin and proximity effect). The HVDC offers an inherent active power control, which makes it more flexible in use and easier to limit the overloads in the system. Moreover, the AC cables experience high charging current which limits their length [3, 4].

Since the advent of advanced electronics, most of the daily use devices, such as phones, televisions, laptops, computers, and even automobiles, have transitioned to DC [5]. The DC motors have found their way into washing machines, refrigerators, fans, and heating and cooling systems, enabling greater speed control and efficiency [6]. The widespread adoption of renewable energy power systems based on solar and wind energy is another factor that shifting the power system paradigm to solely DC or hybrid AC/DC networks [7]. In developed countries, the primary motivations for DC are to increase energy efficiency and conversion to RESs [8]. However, DC provides the chance to significantly raise their standard of life in developing countries. Three significant developments in the last two decades have led to this surge in interest in DC-DNs. First, the power from solar photovoltaics (PV) has dropped dramatically in price and is likely to fall more [9]. Second, LED lighting has swept the globe, rendering traditional incandescent and fluorescent light bulbs obsolete [10, 11]. The third and possibly the most significant development is the shift away from fossil fuels in favor of more environmentally friendly and efficient methods for generating electricity [12]. The authors of [13] examined how low voltage (LV) DN have evolved through time, beginning with the use of conventional AC passive networks and on to the anticipated use of hybrid AC/DC networks. Last-mile distribution systems now have the technical and financial wherewithal to revive DC networks to integrate the new technologies. However, the authors believe that the most cost-effective method of incorporating the new technologies into the existing AC networks is the harmonious cohabitation of both systems via the development of hybrid AC/DC networks.

1.2 Motivations to Reconsider DC

The possibility of using DC for power distribution has drawn the attention of many researchers in recent years. The feasibility of supplying DC to commercial facilities is analyzed in [14]. In addition to doing an economic analysis of DC networks, the authors included estimations for voltage drop and power loss for DC at 326, 120, 230 and 48 DC voltage levels. The research in [15] presented a comprehensive examination for the energy transfer efficiency of AC and DC distribution topologies. According to this research, 2.5% of the energy is lost at each energy conversion stage and these conversion losses can be reduced significantly with DC system utilization in presence of fuel cells and/or other local DC sources. The review on the DC power distribution efficiency in [16] emphasized on the same trend. The case studies involving the implementation of a DC-DN for household appliances have been empirically examined in [17], along with the associated risks and potential solutions. In [18], it is demonstrated that the DC distribution is practicable for commercial buildings with electronic loads and it can also be employed in industrial applications with appropriate system design [19]. The overall efficiency and reliability can be improved by interconnecting the AC microgrids (MGs) through DC links [20].

The recent advances in semiconductor technology combined with the increase in penetration levels of DC loads, RESs and energy storage systems (ESSs) played an important role for deciding to shift from AC distribution to DC or hybrid AC/DC. The DC system usage improves the efficiency in energy distribution, makes it easier to integrate the decentralized RESs and contributes indirectly to reducing the dependency on fossil fuels and greenhouse gas emissions. Furthermore, the Vehicle-to-grid (V2G) operation of electric vehicles (EVs) will become simple with a DC system usage [21]. The conversion stages can be reduced significantly by directly connecting the EV to a DC bus [22]. Interestingly, DC requires a smaller number of outlets because of the widespread usage of USB connections to power portable electronic devices like smartphones, laptops, and tablets etc. Power transfer up to 100W is possible through the USB Type-C connection, which is compliant with the new USB Power Delivery 2.0 Standard (20V at 5A). Due to the different standards of AC worldwide, universal sockets and plugs can only be utilized with DC [23].

1.2.1 DC loads

Most electronic devices at home and/or workplace need DC power (such as computers, laptops, tablets, phones, printers, TVs, microwave ovens, and lights etc.) [24-26] and powering up these loads with AC needs AC/DC conversion stages which results in conversion losses [27]. Several industrial loads also require AC/DC conversion such as pumps, fans, elevators, mills, and traction systems etc. The DC electric arc furnaces are more efficient and produce less light flicker when compared to the AC ones [28]. The electrochemical industry is almost entirely based on DC [29, 30]. Most of the loads are DC these days and most of the electronic loads have their own AC/DC converter. Such redundancies can be eliminated with DC system usage. In 2004, researchers at the Lawrence Berkley National Laboratory started investigating the effectiveness of DC distribution in data centers. The study revealed that DC distribution uses 28% less power than the traditional AC distribution in data centers [31-33].

The Water and Energy Research Laboratory, in collaboration with Nanyang Technological University and Schneider Electric in Singapore, built a hybrid AC/DC network as a test bed to examine different grid topologies and determine appropriate DC voltage levels for the connection of various DC sources and loads [34]. It also serves as a benchmark system for identifying any potential issues regarding DC protection and metering equipment. The power conversion road map for shifting from AC to DC power networks are also presented in [34]. The literature contains several references that illustrated the superiority of DC over AC system for EV charging in smart charging parks, such as [21, 35, 36]. According to the research in [37-39], up to 15% energy can be saved in commercial buildings if they ceased employing the DC-AC-DC conversion process. A research in [40], modelled the loads for steady-state and transient analysis of DC networks and concluded that most of the loads used today can operate equally well with DC as with AC supply.

1.2.2 RESs and DGs

The typical AC power distribution scheme is supported by large-scale power plants, which is then transmitted by HV lines. The "last mile" of the public power distribution network is supplied by a last LV conversion after the energy is distributed by medium voltage (MV) network. There is a worldwide trend toward increasing the utilization rate of RESs at distribution level, driven by economic and environmental factors [41, 42]. Most RESs inherently have DC output at distribution voltage levels like PV and fuel cell. Even wind turbines (WTs), which are inherently AC generators, can be incorporated into a DC network more efficiently since extra conversions can be avoided [43].

The recent advancements in the generation (to produce energy using RES close consumption points), load characteristics and are likely to have a profound impact on the future power system. Many energy consumers have already started producing their own electricity. The existing structure is being challenged by distributed generators (DGs). The presence of DC will make it easier to integrate decentralized DGs and RESs into the in DNs.

1.2.3 Energy storage systems (ESSs)

The ESSs and batteries are DC devices as well. Batteries and ultracapacitors are the two most common energy storage types. The DC has become the most common type of energy storage with the recent advances in battery technology [44]. A comprehensive overview of battery energy storage system (BESS) integration in DC-DNs can be found in [45]. The DC voltage levels 24, 48, and 125 are gaining popularity in lighting applications due to their compatibility with battery storage and solar PV panels [11, 46]. Moreover the flywheels, which are mechanical energy storage devices, can be connected to a DC-DN [47]. The Nippon Telegraph and Telephone Corporation, a Japanese telecommunications company, reported that DC uninterruptible power supplies (UPS) are more reliable in terms of availability than their AC counterparts [48]. Figure 1-1 illustrates the reduction of conversion stages by shifting from AC to DC distribution system.

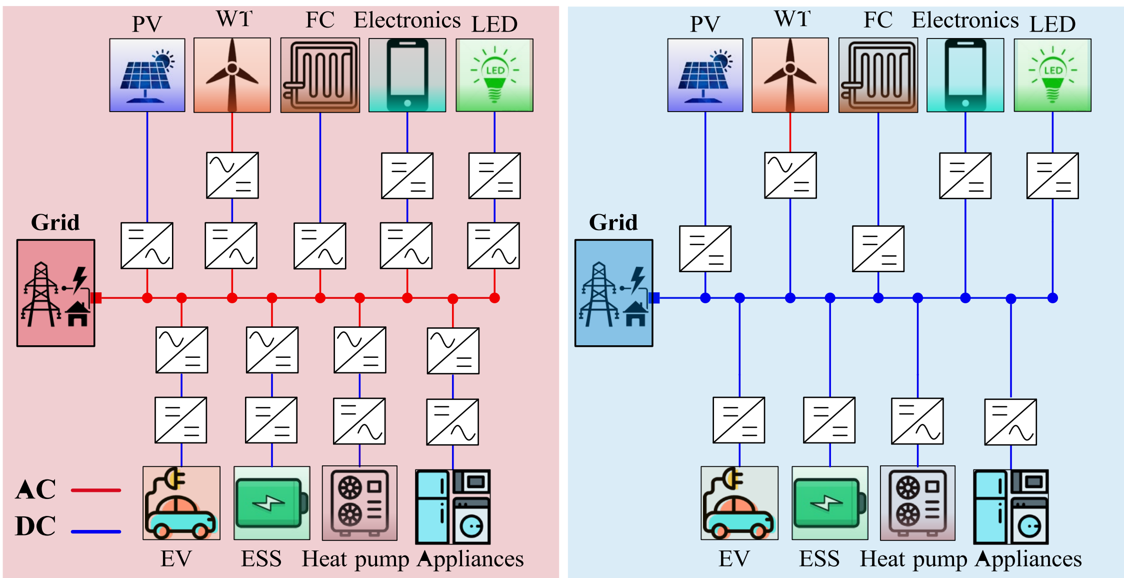

Figure 1-1. Reduction of conversion stages; (a) AC distribution system, (b) DC distribution system

1.3 Research Background

1.3.1 Power flow solvers for DC grids

The widespread use of DC looks to be a major factor in accelerating progress toward sustainability, efficiency, and the reduction of sentient climate change. Further studies are required to ensure their correct design and functionality in terms of interface, topology, and control before they can be successfully integrated into the conventional AC grids. It is feasible to shift gradually from AC to DC in the distribution system, starting with hybrid AC/DC networks and advancing to fully DC-DNs at certain parts of electric power system. Power flow analysis (PFA) in AC grids has been one of the most studied topics since the 1960s. However, the PFA in DC networks is being explored due to the revitalization of the DC networks. It is important to note that the PFA in DC networks is different from DC PFA in conventional AC power systems in which the AC grid PF equations are linearized considering the analogy between the bus voltage angles in AC grids and bus voltage magnitudes in DC networks [49]. The Y_{bus} matrix in DC networks is always diagonally dominant and the Z_{bus} is monotone. The unknown variables in DC networks are only the voltage magnitudes at each bus.

Several PFA methods have been proposed in the literature for DC networks that have origins based on the well-established AC PFA methods. These are upper triangular matrix (UTM) based method [50], linear approximation based methods [51-55], linear loop analysis based method [56], backward/forward sweep (BFS) based method [57], successive approximations (SA) based methods [58, 59] and classical Newton Raphson (NR) based methods [60-62]. The details of these methods are further forth below.

The UTM method [50] cannot handle the meshed network configuration. The Taylor series expansion (TSE) based linear formulation is first proposed in [52] for radial network configuration, and then extended to account for the meshed and bipolar DC network configurations in [53] and [55], respectively. The speed and accuracy of the TSE methods depend on the order of terms used in PF equations for linearization. The lower order terms may result in fast simulation speed at the cost of accuracy and vice versa for the higher order terms [63]. Alternative linear approximation based methods proposed in [51] and [54] have similar precision with the TSE method (first order approximation) and offer better simulation speed. Like the TSE method, the precision of the alternative methods also deteriorates with the increase in loading conditions.

The loop analysis based PF solver proposed in [56] employs injected power rather than injected currents for both radial and mesh DC networks. This method offers better precision compared to the linear approximation based method proposed in [51] but it requires more processing time. The accuracy problem has been eliminated with the successive approximations-based methods [58, 59] through an iterative solution. However, these methods have computational performance disadvantage compared to the classical NR method [64]. It should be noted that, the classical NR method suffers from the disadvantages of classical nodal analysis (NA) formulation as explained in [65] and [66]. The classical NR method is utilized for DC networks in [60-62].

The BFS based PF solver proposed in [57] only considered radial DC network configuration. The BFS class of solvers are initially developed for radial networks and then extended to meshed networks at the expense of additional iterations and/or increased divergence risks. In addition, they have topological limitations and lack of generality, which is reflected in numerous case-by-case treatments in literature [67]. The PF solver based on the convergence conditions and the amount of constant-power generation and load for DC meshed networks is proposed in [68]. The study used the contraction mapping to verify the uniqueness of the solution but did not define the conditions for the contraction constant. Moreover, the uniqueness of the solution can only be established if the PF equations are strictly convex. It is important to note that the PF equations become non-linear and/or non-convex in the presence CPLs in DC networks. The uniqueness of the solution cannot be taken for granted due to the non-linear and non-convex nature of the PF equations. A review of classical and emerging methods for DC PFA can be found in [69]. A comparative study on numerical convergence and processing time of different DC PFA methods is presented in [70].

There are some other PFA methods that have been successfully applied to AC grids. However, their application to DC networks needs further research. For instance, the graph-theory based PF methods [71-73], and Holomorphic Embedding PF method (HE-PFM) [74, 75] and Modified Augmented Nodal Analysis (MANA) [76]. In general, most of the studies in the literature did not consider the uniqueness of the PF solution. Furthermore, no study considered DC/DC converter models in the PF formulation.

1.3.2 Power flow solvers for hybrid AC/DC grids

Hybrid AC/DC DNs are gaining popularity due to their potential to conflate the benefits of both AC and DC networks. Such DNs have very distinct features compared to traditional transmission and DNs. The inclusion of different type converters, interconnections between AC and DC networks and buses imposes new PF calculation challenges. Two good examples of hybrid AC/DC networks that already exist in power systems are hybrid AC/DC MGs and HVDC networks. There are two approaches for hybrid AC/DC network PF solution: 1-AC and DC networks are solved iteratively and sequentially; 2- AC and DC networks are solved simultaneously. The sequential approach is easy to implement. However, it encounters convergence problems, and the solution is time consuming.

A sequential PF solver based on BFS method for hybrid AC/DC MGs is proposed in [77]. In parallel to the research on AC/DC MGs, the PFA have been studied for HVDC networks as well. Initial work using a sequential algorithm is presented in [78] for multi-terminal DC (MT-DC) networks. The work in [79] is based on mismatch equations and accounts for AC and DC networks, and VSC station models. The limitations of BFS techniques are well known. The derivation of mismatch equations is often complicated. The NR based sequential approaches are proposed to solve the multi-terminal VSC-HVDC PF problem in [80, 81]. The convergence characteristics of the NR method are undermined due to the sequential iterative solution adopted. The open source MATLAB-based AC/DC PFA tool MatACDC [82] employs a sequential approach. It uses AC PF routines of MATPOWER [83] and DC subsystem solution is obtained assuming the presence of a DC slack bus. A slack bus in the DC network makes the solution easier in sequential PFA, as the PF of each subsystem is calculated individually. Furthermore, the constant power case can be used when DC power losses are neglected [84]. This assumption also simplifies the coupling mechanism in the AC PF, as the converter active power balance is independent of the DC side and must be known in advance when active power flow is constant. However, this assumption requires a specific available active power, which may not be possible in specific PF conditions.

The unified PF method for HVDC networks with VSCs is first reported in [85]. In

[86], the converter is modeled as a voltage-dependent load to eliminate the DC variables from the PF equations. Hence, the DC system dynamics are not represented completely. The AC/DC coupling is modeled by an admittance building block to convert the DC network parameters to equivalent AC grid parameters in [87]. The implementation of this approach is very complex, and it requires significant modifications for each different network configuration. A generalized reduced gradient (GRG) method is proposed to solve hybrid AC/DC networks in [88]. The NR method exhibits better convergence characteristics compared to GRG method because GRG method uses the steepest descent while NR method uses curvature descent. In addition, the NR method is a higher order method compared to GRG, hence it builds a better approximation of the non-linear function.

The increase in power demand has pushed the power systems closer to their limits, in addition to the growing intermittent in power generation due to RES without a proportionate expansion in transmission network infrastructure. Despite the possibility of a PF solution under these conditions, the classical NR-based PF techniques may fail due to computational difficulties caused by the singularity of the Jacobian matrix under critical conditions and have difficulties solving ill-conditioned systems [89-91]. A power system may become ill-conditioned due to the high R/X ratio of the lines, radial structure of the network and/or the loading of the system approaching towards maximum loading point [92-95]. The implementation of classical NR method with traditional NA approach may effect it convergence performance [65, 66]. Hence, efforts are made in literature to improve the traditional NA approach. For instance, the Modified Nodal Analysis (MNA) formulation is extended to accommodate various component models and PF constraints, yielding the MANA PF solver [76]. This formulation can handle arbitrary DN topologies and devices with arbitrary constraints and variables [96]. It is demonstrated in [76, 96] that MANA formulation has the inherited properties to solve unbalanced networks and provide multiphase PF solution. An extension of MANA is proposed in [97] by adding the reactive power of DGs in the formulation as state variables. However, these references are only considered AC networks.

The PF solver in [98] is based on HE-PFM for VSC-based AC/DC networks. A general embedded model is established for AC/DC PF with VSCs to accommodate various bus types, VSC configurations, control strategies and operating conditions. Although HE-PFM gives an early indication about the solution convergence or divergence, a major problem with HE-PFM is its computational burden of finding roots. The implementation of HE-PFM in terms of time is mainly comprised of power series calculation and rational approximations. The calculation of the Pade approximation only makes sense when the roots of the denominator are also calculated and the root searching of high polynomials incurs a significant additional computational burden. In addition, if the number of power terms are large, numerical errors in calculating the Pade approximation may lead to spurious poles [99].

1.4 Problem Statement

The analysis of DC-DNs brings several challenges that must be addressed using the most up-to-date methods. When a power converter operates in constant power mode to supply a constant power load (CPL), the PF equations in DC network become non-linear and non-convex. Hence, the solution of the PF equations requires iterative techniques. Numerous operational and control optimization problems need accurate and efficient PF solvers. Typically, the PF equations are nonlinear, hence the convergence of the PFA method is not always guaranteed. Moreover, the existing DC PFA methods disregard the DC/DC converters which may exist in future DC networks.

Most of the available literature on AC/DC PF solution is for transmission networks (HVDC applications). Despite the simplicity of the methods proposed for point-to-point HVDC, their application is limited to the point-to-point DC connection of two VSCs The DNs are different from transmission networks in many aspects such as high R/X ratios, radial feeders, more connection points for loads, generators, and different converter. Hence, the proposed methods for transmission networks with AC/DC interconnections may not be sufficient for hybrid AC/DC DNs. The classical NA formulation and NR based PF solver may fail to converge while simulating stressed DNs with tight voltage regulation requirements. The existing literature disregards the AC/DC and DC/DC converter models in PF formulation. In addition, the convergence of PFA methods to a unique solution is also overlooked in literature.

The power converters (AC/DC and/or DC/DC) may be an integral part of future power systems, so the representation of these converters in PF equations is a research gap that should be addressed with most up to date and robust PF methods. The objective of this thesis is not only to develop generic converter PF models but also to consider their associated controls and to integrate them into robust PF methods. The key contributions of the thesis are listed below.

1.5 Key Contributions

- A novel Laplacian Matrix (LM) based PF solver for DC networks hosting different load types including CPLs for both radial and meshed configurations. This method has network topology constraints as it requires an extra matrix to solve a meshed network, which increases the processing time. This method is further extended where a generalize formulation is proposed based on improved LM (ILM). The ILM method does not have network topology constraints. The uniqueness of the solution of both LM and ILM methods is demonstrated by contraction mapping using the Banach fixed-point theorem (BFPT). Related research outputs are [100] and [101].
- A PF solver based on MANA formulation with NR algorithm (MANA-NR) for DC networks. The uniqueness of the solution of MANA-NR is demonstrated by Kantorovich's theorem. Related research output is [102].
- Implementation of DC/DC converter models into PF formulation for DC networks with ILM method. Related research output is [103].
- Implementation of DC/DC converter models into PF formulation for DC networks with MANA-NR method. Related research output is [104].
- Unified PF solver for hybrid AC/DC networks with MANA-NR with AC/DC and DC/DC converter models. The superior convergence characteristics of the MANA-NR over the classical NA-NR is also demonstrated through simulations and explained by inspecting the condition number of the Jacobian matrix. Related research output is [105].
- Implementation of Solid State Transformer (SST) model into PF formulation for hybrid AC/DC networks with MANA-NR method. Related research output is [106].
- Literature survey on future distribution networks.

1.6 Software Used

All solvers are coded in MATLAB (2020b) language on a desktop PC with the following specifications: CPU (Intel Core i7 @ 3.21 and 3.19 GHz), 16 GB RAM, 64-bit operating system. To validate the accuracy of the proposed PF solvers time domain simulation are performed in EMT software [65].

1.7 Assumptions and Limitations

The following assumptions are made for this study.

1. It is assumed that the network's graph is connected and free from any instances of islanding within the feeder. This assumption guarantees the non-singularity of the admittance matrix.

2. It is assumed that there exists at least one node within the system that embodies a CPL. This assumption introduces nonlinearity into the PF equations and necessitates the utilization of an iterative solver.

3. For a steady state solution, the converter angle α is constant and can be found via PF solution. For non-linear simulator the value of α is constant at each iteration. For AC/DC analysis it is assumed that angle α is constant but unknown quantity.

The limitations of the solvers are listed below.

1. The graph-based methods (LM, ILM, and e-ILM) demonstrate a wide convergence range but their usage is not recommended in the applications which require fast computation speed. Conversely, the MANA-based PF solver offers fast and robust performance, albeit with a conservative theoretical convergence range.

2. The converter models employed in this study are designed for positive sequence solvers. However, they can be adapted and integrated into an unbalanced/multi-phase MANA formulation, considering the control strategy for the positive sequence.

1.8 Thesis Organization

The subsequent sections of the thesis are structured in the following manner. Chapter 2 presents various hybrid AC/DC network component models for PF formulation. These models include DC/DC and AC/DC converters, SST, and load. Chapter 3 outlines the development of graph theory-based PF solvers, namely the LM, ILM, and e-ILM, for DC grids. Chapter 3 also encompasses the discussion on the convergence proof of these solvers. In Chapter 4, a PF solver for DC grids with MANA formulations is presented, and the convergence proof is derived using the Kantorovich theorem. Furthermore, the formulation is expanded (e-MAMA) to integrate DC/DC converter models into the PF equations. Chapter 4 also evaluates the numerical performance of various PF solvers for DC grids. Chapter 5 focuses on the development of a unified PF solver based on MANA formulation for hybrid AC/DC grids. This solver accounts for AC/DC converters, DC/DC converters and SST models, providing a robust tool for PFA. Finally, in Chapter 6, the conclusions drawn from the research efforts are presented. Chapter 6 also outlines potential future research directions that can be explored in relation to the topic at hand.

CHAPTER 2. System Modelling

Converter models are very important building blocks in the PF formulation to achieve accurate solutions. In the framework of unified AC/DC PF, various modelling approaches are introduced to represent the accurate VSC behavior in AC/DC PF calculation [107-110]. To handle the converter reactive power balance and losses, the VSC is represented by a complex-valued tap changer with parallel impedances in [107-110]. This model can fully address the VSC DC side through a variable admittance. This means an additional state for each VSC beyond the MTDC conventional bus voltage magnitudes and angles used in traditional AC PF formulation. In addition to the increased complexity due to the additional state variable, converter reactive power calculation is a challenge in PF simulation [111]. In [18], the entire point-to-point HVDC link is represented with an equivalent PI model. Despite its simplicity, its application is limited to the point-to-point DC connection of two VSCs. The focus is mainly on HVDC applications in the existing literature. The aim of this chapter is to develop generic AC/DC network component models for PF solvers.

2.1 AC/DC Converter Models

Two types of AC/DC converters are discussed in this section viz: VSC and thyristor-based line commutating converter (LCC). In VSCs, the AC active and reactive currents can be controlled independently through vector control [112, 113]. The active current channel can be used to control either active power output (P) or DC terminal voltage ($\mathrm{V_{dc}}$). The reactive current channel can be used to control either reactive power output (Q) or AC terminal voltage ($\mathrm{V_{ac}}$). However, either P or $\mathrm{V_{dc}}$ can be controlled in an LCC terminal. The reactive power (i.e., power factor) is determined by the firing angle. To eliminate the AC/DC voltage ratios, per unit (*pu*)values are used in converter models.

2.1.1 VSC and LCC Converter models

The active and reactive power outputs of a VSC can be controlled independently [112, 113]. However, the LCC active and reactive power outputs are not independent. The power factor angle is the same as the firing angle which is used to control the active power output.

The steady state model of a VSC connecting an AC bus with a DC bus is shown in Figure 2-1.

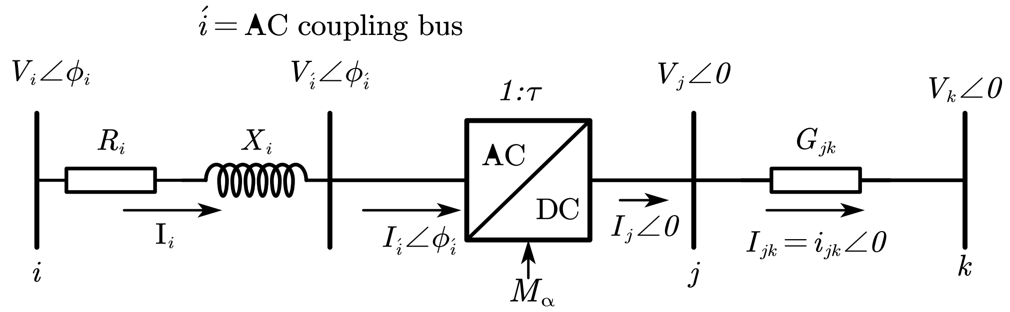

Figure 2-1. VSC Model

The model of the VSC shown in Figure 2-1 can be represented as follows.

$$V_j = \tau V_i' \tag{2-1}$$

where τ: converter constant. M_α: modulation index of the converter, α: Converter angle

It is important to note that the converter constant depends on the converter type. To simplify the complications associated with AC/DC voltage ratios, we use per unit values. Consequently, the base voltage at the AC bus is smaller than that of the corresponding DC bus by a factor $\left(\frac{\sqrt{3}}{2\sqrt{2}}\right)M_\alpha = 0.612M_\alpha$ for a two-level PWM. There are two viable approaches that can be adopted to address the discrepancy in base voltage levels.

Method 1: The value of M_i can be chosen as 1 for all converters, resulting in the base voltage on the DC side being 1.634 times that of the line-to-line voltage on the AC side. Any subsequent adjustments to M_i can be made in a manner akin to tap changers in the conventional power flow algorithm, by modifying the admittance.

Method 2: As an alternative, the base voltage on the DC side can be set to $\left(\frac{1.634}{M_i}\right)$ times the line-to-line AC voltage without making any changes to the admittance matrix. This adjustment will result in the values of $V_j = v_j\angle\theta$ (expressed in per unit) being modified.

Remark 1: Here, the angle θ is an arbitrary angle that is applied to all DC buses (voltages and currents). For instance, option is chosen θ equal to the phase angle of the corresponding AC coupling bus. Another way around is to set $\theta = 0$, for all DC buses, and it will create a phase difference between voltages at corresponding AC buses. This phase difference is equal to the AC coupling bus phase angle.

The relationship between the input voltage angle and the output DC voltage can be influenced by the modulation index and the control strategy employed. Depending on the control strategy, the phase matching between AC network and its corresponding DC side is achieved using a phase shifter. The angle of the phase shifter is not a state, rather it is adjusted as a function of other states to achieve zero reactive power in DC side.

The voltage and current relationship between AC bus (i) and AC coupling bus (i') is a function of τ ($V_j = \tau V_{i'}$ and $I_j = (\tau^{-1})^* I_{i'}$); where, $\tau = \frac{1}{M_i} \measuredangle \delta$ (using **Method 1**) or $\tau = 1 \measuredangle \delta$ (using **Method 2**); δ: is the phase shift between AC coupling bus and DC bus; X_i: converter series reactance; R_i: converter resistive loss.

The current I_j maintains the same phase shift ($\measuredangle \delta$) w.r.t to $I_{i'}$ as that of the corresponding voltage V_j w.r.t $V_{i'}$. Thus, we have $V_j = |V_j| \measuredangle \phi_j = |V_{i'}| \measuredangle \phi_{i'}$ as the voltage phasor of AC coupling bus (converter AC voltage phasor) and δ cancels the phase of AC coupling bus (yielding $\phi_j = \theta = 0$, as explained in Remark 1) as $\delta = -\phi_{i'}$ ($\delta = \phi_j - \phi_{i'} = \alpha - \phi_i$).

Remark 2: When a constant reactive power injection is considered at the AC coupling bus, it is treated as a load bus within the context of PFA. The voltage and phase angle at this bus can be determined. The voltage of both the AC coupling bus and the DC bus are regarded as variables and are obtained through the PF solution. However, it is also possible to assign a constant voltage to the AC coupling bus, allowing the PFA to determine the necessary reactive power injection (referred to as a P-V Bus in the PF context). After PF is conducted the converter angle $\alpha = \phi_i - \phi_{i'}$ can be obtained directly.

Remark 3: For a steady state solution, the converter angle $\alpha = \phi_i - \phi_{i'}$ is constant and can be found via PF solution. For non-linear simulator the value of α is constant at each time step. For AC/DC analysis it is assumed that angle α is constant but unknown quantity. The model can be simplified by neglecting the filter impedance and considering the efficiency parameter into play to account for the converter losses.

Remark 4: Method 2 (used in this study) and synthesized voltage phasor $|V_j| \measuredangle \phi_j$ suggest that a Jacobian matrix for voltages and phase angles can be build based on nodal power balance.

The value of converter constant for 6 pulse LCC converter, and 12 pulse LCC will be equal to $3\sqrt{2}/\pi$, and $6\sqrt{2}/\pi$, respectively. In the rest of the chapter VSC model is utilized, any other model can easily be replaced in the formulation as explained above. The relationship between AC voltage and DC voltage base at unity modulation index is given below.

$$V_{j,base} = \tau M_i^{-1} V_{i,base} \tag{2-2}$$

As 1 *pu* AC voltage is equal to 1 *pu* DC voltage at unity modulation index, a general expression in per unit between AC and DC voltages can be written as follows.

$$V_{j,pu} = M_i^{-1} V_{i,pu} \tag{2-3}$$

The relationship between DC power and the AC active power is a function of converter`s efficiency.

$$P_{i,pu} = P_j / \eta_c = (V_{j,pu} I_{jk,pu}) / \eta_c \tag{2-4}$$

The DC current can be written as follows.

$$I_{jk,pu} = G_{jk,pu}(V_{j,pu} - V_{k,pu}) \tag{2-5}$$

By substituting (2.3) and (2.5) in (2.4) we can get.

$$P_{ik,pu} = G_{jk,pu}\left(\frac{\gamma}{\eta_{c-rec}} + \beta\eta_{c-inv}\right)\left(\left(\frac{V_{i,pu}}{M_i}\right)^2 - \frac{V_{i,pu}V_{k,pu}}{M_i}\right) \tag{2-6}$$

$$\text{where} \quad \begin{array}{l} \gamma = 1, \quad \beta = 0 \;\rightarrow\; if \quad M_i^{-1}V_i > V_k \\ \gamma = 0, \quad \beta = 1 \;\rightarrow\; if \quad M_i^{-1}V_i < V_k \\ \gamma = \tfrac{1}{2}, \quad \beta = \tfrac{1}{2} \;\rightarrow\; if \quad M_i^{-1}V_i = V_k \end{array}$$

The reactive power at the AC side of the converter can be calculated as follows:

$$Q_i = P_i tan(\varphi) \tag{2-7}$$

where, φ is the converter power factor angle.

2.2 DC/DC Converter Models

Although DC/DC converters are mostly employed for voltage regulation, additional control techniques exist such as constant current, constant power, and constant duty cycle

(D). The DC/DC converters are modelled based on the assumption that the converter conductance is greater than critical inductance, which implies that the converter is operating in continuous conduction mode (CCM).

2.2.1 Buck converter model

The buck converter, also known as a step-down converter, provides an output voltage that is lower than its input voltage. The duty cycle ratio (D) of the converter can be adjusted to modify the output voltage. The steady state buck converter model is shown in Figure 2-2.

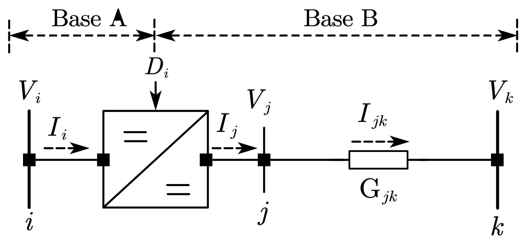

Figure 2-2. Buck converter model

The duty cycle ratio of a buck converter can be calculated with the following expression.

$$D_i = \frac{t_{on}}{t_{on} + t_{off}} \tag{2-8}$$

where, t_{on} and t_{off} are the time intervals for the converter switch at *ON* and *OFF* positions, respectively, in one cycle.

The voltage and current input/output relationships are given below.

$$V_j = D_i V_i \tag{2-9}$$

$$I_j = D_i^{-1} I_i \tag{2-10}$$

At $D_i = 1$, the voltage base will be the same on both side of the converter.

$$V_{j,base} = V_{i,base} \tag{2-11}$$

Typically, D is less than unity for buck converter, hence the voltage base will not be the same on both sides of the converter. To keep the same base on both sides of the converter, we need to modify the conductance coupling on the output side of the converter according to the new base. The rated voltage of both sides of the converter can be set as base voltage. After modifying the admittance matrix, the input/output relationships in *pu* can be written as follows.

$$V_{j,pu} = D_i V_{i,pu} \tag{2-12}$$

$$P_{i,pu} = P_{j,pu} / \eta_i = (V_{j,pu} I_{jk,pu}) / \eta_i \tag{2-13}$$

$$I_{jk,pu} = G_{jk,pu}(V_{j,pu} - V_{k,pu}) = G_{jk,pu}(D_i V_{i,pu} - V_{k,pu}) \tag{2-14}$$

The power flow between bus "*i*" and "*k*" can be calculated as follows.

$$P_{ik,pu} = G_{jk,pu}\left(\gamma_i/\eta_i + \beta_i\eta_i\right)\left(\left(D_i V_{i,pu}\right)^2 - D_i V_{i,pu} V_{k,pu}\right) \tag{2-15}$$

where
$$\begin{array}{l} \gamma_i = 1, \quad \beta_i = 0 \quad \rightarrow \quad if \quad D_i V_i > V_k \\ \gamma_i = 0, \quad \beta_i = 1 \quad \rightarrow \quad if \quad D_i V_i < V_k \\ \gamma_i = \frac{1}{2}, \quad \beta_i = \frac{1}{2} \quad \rightarrow \quad if \quad D_i V_i = V_k \end{array}$$

2.2.2 Boost converter model

The boost converter, also known as a step-up converter, provides an output voltage that is higher than its input voltage. The steady state model of a boost converter is shown in Figure 2-3.

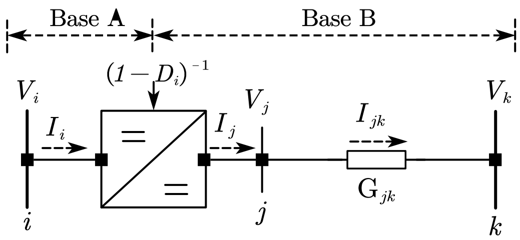

Figure 2-3. Boost converter model

The input/output relationships of boost converter are given below.

$$V_j = \left(1 - D_i\right)^{-1} V_i \tag{2-16}$$

$$I_j = (1 - D_i) I_i \tag{2-17}$$

At the $D_i = 0$ voltage base will be the same on both side of the converter.

$$V_{j,base} = V_{i,base} \tag{2-18}$$

Like buck converter, the rated voltage of both sides of the converter are set as base voltages. After modifying the conductance coupling on the output side of the converter according to the new base conductance as explained earlier, the relationship between voltages in *pu* can be written as follows:

$$V_{j,pu} = 1/(1-D_i)V_{i,pu} \tag{2-19}$$

$$P_{i,pu} = P_{j,pu}/\eta_i = (V_{j,pu}I_{jk,pu})/\eta_i \tag{2-20}$$

$$I_{jk,pu} = G_{jk,pu}(V_{j,pu} - V_{k,pu}) = G_{jk,pu}\left(\frac{V_{i,pu}}{1-D_i} - V_{k,pu}\right) \tag{2-21}$$

$$P_{ik,pu} = G_{jk,pu}\left(\frac{\gamma_i}{\eta_i} + \beta_i\eta_i\right)\left(\left(\frac{V_{i,pu}}{1-D_i}\right)^2 - \frac{V_{i,pu}}{1-D_i}V_{k,pu}\right) \tag{2-22}$$

$$\text{where} \quad \begin{array}{l} \gamma_i = 1, \quad \beta_i = 0 \quad \rightarrow \quad if \quad (1-D_i)^{-1}V_i > V_k \\ \gamma_i = 0, \quad \beta_i = 1 \quad \rightarrow \quad if \quad (1-D_i)^{-1}V_i < V_k \\ \gamma_i = \tfrac{1}{2}, \quad \beta_i = \tfrac{1}{2} \quad \rightarrow \quad if \quad (1-D_i)^{-1}V_i = V_k \end{array}$$

2.2.3 Buck-Boost converter model

The buck-boost converter has both the characteristics of buck and boost. The output voltage can be lower or higher than the input voltage. The steady state model of buck-boost converter is shown in Figure 2-4.

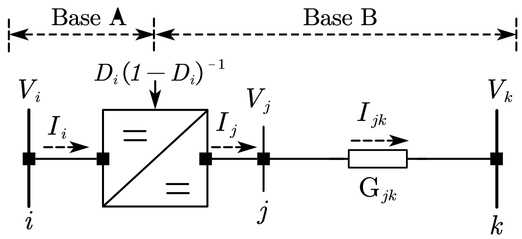

Figure 2-4. Buck-Boost Converter Model

The input/output relationships of boost converter are given below.

$$V_j = D_i(1-D_i)^{-1}V_i \tag{2-23}$$

$$I_j = (1-D_i)D_i^{-1}I_i \tag{2-24}$$

After modifying the conductance coupling on the output side of the converter according to the new base conductance, the relationship between voltages can be written as follows:

$$V_{j,pu} = \frac{D_i}{1-D_i}V_{i,pu} \tag{2-25}$$

$$P_{i,pu} = \frac{P_{j,pu}}{\eta_i} = \frac{(V_{j,pu} I_{jk,pu})}{\eta_i} \tag{2-26}$$

$$I_{jk,pu} = G_{jk,pu}(V_{j,pu} - V_{k,pu}) = G_{jk,pu}\left(\frac{D_i}{1-D_i} V_{i,pu} - V_{k,pu}\right) \tag{2-27}$$

$$P_{ik,pu} = G_{jk,pu}\left(\frac{\gamma_i}{\eta_i} + \beta_i \eta_i\right)\left(\left(\frac{D_i}{1-D_i} V_{i,pu}\right)^2 - \left(\frac{D_i}{1-D_i} V_{i,pu} V_{k,pu}\right)\right) \tag{2-28}$$

$$\text{where} \quad \begin{array}{l} \gamma_i = 1, \quad \beta_i = 0 \ \rightarrow \ if \quad D_i(1-D_i)^{-1} V_i > V_k \\ \gamma_i = 0, \quad \beta_i = 1 \ \rightarrow \ if \quad D_i(1-D_i)^{-1} V_i < V_k \\ \gamma_i = \tfrac{1}{2}, \quad \beta_i = \tfrac{1}{2} \rightarrow \ if \quad D_i(1-D_i)^{-1} V_i = V_k \end{array}$$

2.2.4 DC branch model

As previously stated, the conductance coupling between the buses must be modified to maintain the same base on both sides of the converter. To generalize the approach so that a straightforward DC/DC converter model can be used in PF formulation. Let's consider the DC branch model with a DC/DC converter model given in Figure 2-5, with *N* off nominal voltage ratio between two sides of the converter. Please note that starting from this point onwards, the formulation in per unit and the subscript *p.u.* is omitted.

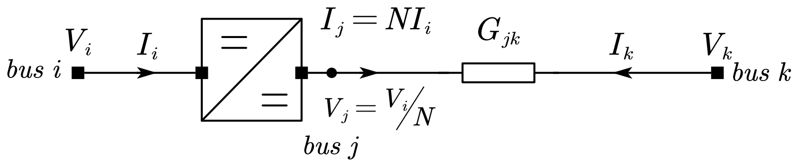

Figure 2-5. DC branch model with DC/DC converter

The current injection can be written as a function of the bus voltage as follows.

$$\begin{bmatrix} I_i \\ I_k \end{bmatrix} = G_{jk} \begin{bmatrix} V_i \\ V_k \end{bmatrix} \tag{2-29}$$

The admittance matrix can be modified as follows:

$$G_{jk} = \begin{bmatrix} G_{jk}/N^2 & -G_{jk}/N \\ -G_{jk}/N & G_{jk} \end{bmatrix} \tag{2-30}$$

2.3 Line Flows in Hybrid AC/DC DN

In hybrid AC/DC DN, a connection between two different types of buses is conceivable. An illustration is shown in Figure 2-6. Instead of developing a universal bus power injection formulation, the sum of line flows and their respective partial derivatives are considered (for MANA formulation).

The total injected power at bus “*a*” is the sum of all line flows connected to bus “*a*”.

$$P_a = P_{ab} + P_{ac} + P_{ad} \tag{2-31}$$

The partial derivatives of active power injection at bus "*a*" with respect to the magnitudes of the bus voltages will be as follows.

$$\frac{\partial P_a}{\partial V_a} = \frac{\partial P_{ab}}{\partial V_a} + \frac{\partial P_{ac}}{\partial V_a} + \frac{\partial P_{ad}}{\partial V_a} \tag{2-32}$$

$$\frac{\partial P_a}{\partial V_b} = \frac{\partial P_{ab}}{\partial V_b} + 0 + 0 \tag{2-33}$$

$$\frac{\partial P_a}{\partial V_c} = 0 + \frac{\partial P_{ac}}{\partial V_c} + 0 \tag{2-34}$$

$$\frac{\partial P_a}{\partial V_d} = 0 + 0 + \frac{\partial P_{ad}}{\partial V_d} \tag{2-35}$$

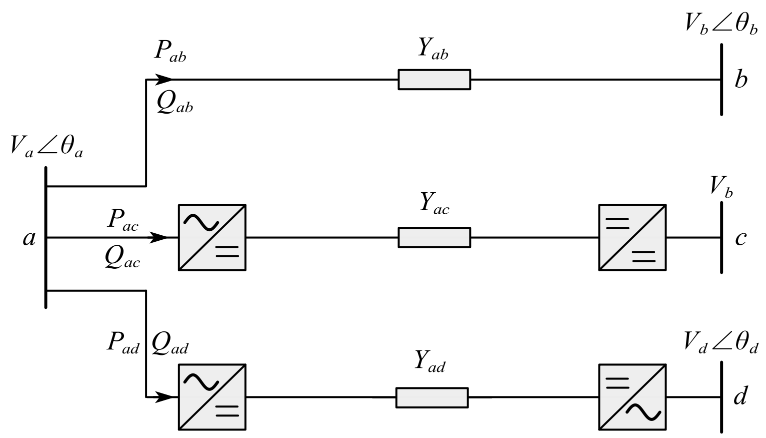

Figure 2-6. Connection of an AC bus with different type of buses

The detailed line flow equations for all possible interconnections in DC and hybrid AC/DC DNs are derived in the next section. Please note that reactive power is not defined for the DC network.

2.4 Bus Injection Equations

As the DC and hybrid AC/DC DNs may have a variety of bus connections, the derivation of power injection equations along with their partial derivatives for each possible configuration is presented in this section.

2.4.1 Case 1 (AC-AC-AC)

In this case, the AC bus is connected to an AC bus through AC line. This case can also be used to incorporate the power plant substation (such as converter filters, step-up transformers etc.) between the AC bus and the AC/DC converter connection point. The configuration is shown in Figure 2-27.

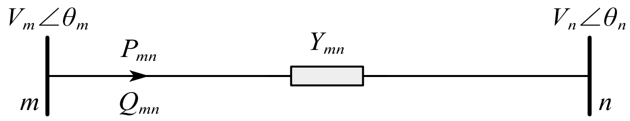

Figure 2-7. Case 1 (AC bus, AC line, AC bus)

For the above case line flows will be as follows.

$$P_{mn} = V_m^2 G_{mn} - V_m V_n (G_{mn}\cos\theta_{mn} + B_{mn}\sin\theta_{mn}) \tag{2-36}$$

$$Q_{mn} = -V_m^2 B_{mn} - V_m V_n (G_{mn}\theta_{mn}\sin\theta_{mn} - B_{mn}\cos\theta_{mn}) \tag{2-37}$$

Partial derivatives of line flows with respect to the bus unknowns ($\theta_m, \theta_n, V_m, V_n$) are given below.

$$\frac{\partial P_{mn}}{\partial\theta_m} = -V_m V_n (-G_{mn}\sin\theta_{mn} + B_{mn}\cos\theta_{mn}) \tag{2-38}$$

$$\frac{\partial P_{mn}}{\partial\theta_n} = -V_m V_n (G_{mn}\sin\theta_{mn} - B_{mn}\cos\theta_{mn}) \tag{2-39}$$

$$\frac{\partial P_{mn}}{\partial V_m} = 2V_m G_{mn} - V_n (G_{mn}\cos\theta_{mn} + B_{mn}\sin\theta_{mn}) \tag{2-40}$$

$$\frac{\partial P_{mn}}{\partial V_n} = -V_m (G_{mn}\cos\theta_{mn} + B_{mn}\sin\theta_{mn}) \tag{2-41}$$

$$\frac{\partial Q_{mn}}{\partial\theta_m} = -V_m V_n (G_{mn}\cos\theta_{mn} + B_{mn}\sin\theta_{mn}) \tag{2-42}$$

$$\frac{\partial Q_{mn}}{\partial \theta_n} = V_m V_n (G_{mn} \cos\theta_{mn} + B_{mn} \sin\theta_{mn}) \tag{2-43}$$

$$\frac{\partial Q_{mn}}{\partial V_n} = -2V_m B_{mn} - V_n (G_{mn} \sin\theta_{mn} - B_{mn} \cos\theta_{mn}) \tag{2-44}$$

$$\frac{\partial Q_{mn}}{\partial V_n} = -V_m (G_{mn} \sin\theta_{mn} - B_{mn} \cos\theta_{mn}) \tag{2-45}$$

2.4.2 Case 2 (AC– DC– AC)

In this case, two AC buses are connected with a DC line through converters on each end as illustrated in Figure 2-8.

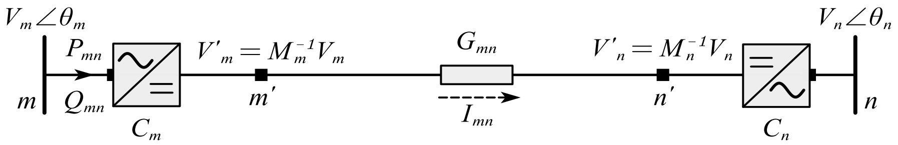

Figure 2-8. Case 2 (AC bus, DC line, AC bus)

$$P_{mn} = G_{mn}(M_m^{-2}V_m^2 - M_n^{-1}V_n) \tag{2-46}$$

The converter efficiency depends on the direction of PF direction. If the direction of PF is from bus *m* to bus *n*, then the converter C_m will operate in rectifier (*rec*) mode and the converter C_n will operate in inverter (*inv*) mode, and the equation for line flow can be written as follows.

$$P_m = P'_m \times \frac{1}{\eta_{rec}} \quad if \quad V'_m > V'_n \tag{2-47}$$

If the direction of PF is from bus *n* to bus *m*, then converter C_n will operate in rectifier mode and the converter C_m will operate in inverter mode, the equation for line flow can be written as follows.

$$P_m = P'_m \times \eta_{inv} \quad if \quad V'_m < V'_n \tag{2-48}$$

If voltages are equal at point m' and n', the equation for line flow can be written as follows.

$$P_m = P'_m \times \left(\frac{1}{2\eta_{rec}} + \frac{1}{2}\eta_{inv} \right) \quad if \quad V'_m = V'_n$$

(2-49)

A generalized expression of line flows incorporating the convertor efficiency can be written as follows.

$$P_{mn} = G_{mn}(M_m^{-2}V_m^2 - M_m^{-1}V_m M_n^{-1}V_n) \times (\frac{\alpha_m}{\eta_{mn}} + \beta_m \eta_{nm}) \tag{2-50}$$

$$Q_{mn} = P_{mn} \times tan\varphi_c \tag{2-51}$$

where, φ_c: Power factor angle, α and β are the convertor coefficients and their values is dependent on the direction of power flow as given below.

$$\begin{aligned} (\alpha_m, \beta_m) &= (1,0) \quad \rightarrow \quad V'_m < V'_n \\ (\alpha_m, \beta_m) &= (0,1) \quad \rightarrow \quad V'_m < V'_n \\ (\alpha_m, \beta_m) &= (\tfrac{1}{2}, \tfrac{1}{2}) \quad \rightarrow \quad V'_m = V'_n \end{aligned} \tag{2-52}$$

As the line flow equations do not contain bus voltage angles, the partial derivatives with respect to (w.r.t) bus voltage angles will be zero. Partial derivatives of the active power line flow w.r.t bus voltage magnitudes and the modulation index *M* are given below. The partial derivatives of reactive power flow can be achieved from the active power derivatives using (2-51).

$$\frac{\partial P_{mn}}{\partial V_m} = G_{mn}(M_m^{-2} \times 2V_m - M_m^{-1}M_n^{-1}V_n) \times (\frac{\alpha_m}{\eta_{mn}} + \beta_m \eta_{nm}) \tag{2-53}$$

$$\frac{\partial P_{mn}}{\partial V_n} = G_{mn}(-M_m^{-1}V_m M_n^{-1}) \times (\frac{\alpha_m}{\eta_{mn}} + \beta_m \eta_{nm}) \tag{2-54}$$

$$\frac{\partial P_{mn}}{\partial M_m} = G_{mn}(-2M_m^{-3}V_m^2 + M_m^{-2}V_m M_n^{-1}V_n) \times (\frac{\alpha_m}{\eta_{mn}} + \beta_m \eta_{nm}) \tag{2-55}$$

$$\frac{\partial P_{mn}}{\partial M_n} = G_{mn}(M_m^{-1}V_m M_n^{-2}V_n) \times (\frac{\alpha_m}{\eta_{mn}} + \beta_m \eta_{nm}) \tag{2-56}$$

2.4.3 Case 3 (AC-DC-DC)

In this case, the AC bus is connected to a DC bus through a DC line with an AC/DC converter connected to an AC bus as shown in Figure 2-9.

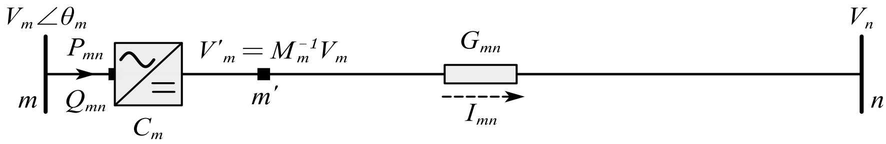

Figure 2-9. Case 3 (AC bus, DC line, DC bus)

The line flows from AC side can be written as below.

$$P_{mn} = G_{mn}(M_m^{-2}V_m^2 - M_m^{-1}V_mV_n)\times(\frac{\alpha_m}{\eta_{mn}} + \beta_m\eta_{nm}) \tag{2-57}$$

$$Q_{mn} = P_{mn}\times tan\varphi_c$$

(2-58)

The values of the converter efficiency coefficients will be as given in (2.52). In this case the possible unknowns are the AC bus voltage magnitudes and angles, the DC bus voltage magnitude, and the modulation index of the AC/DC converter.

$$\frac{\partial P_{mn}}{\partial\theta_m} = \frac{\partial Q_{mn}}{\partial\theta_m} = 0 \tag{2-59}$$

$$\frac{\partial P_{mn}}{\partial V_m} = G_{mn}(M_m^{-2}\times 2V_m - M_m^{-1}V_n)\times(\frac{\alpha_m}{\eta_{mn}} + \beta_m\eta_{nm}) \tag{2-60}$$

$$\frac{\partial P_{mn}}{\partial V_n} = G_{mn}(-M_m^{-1}V_m)\times(\frac{\alpha_m}{\eta_{mn}} + \beta_m\eta_{nm}) \tag{2-61}$$

$$\frac{\partial P_{mn}}{\partial M_m} = G_{mn}(-2M_m^{-3}V_m^2 + M_m^{-2}V_mV_n)\times(\frac{\alpha_m}{\eta_{mn}} + \beta_m\eta_{nm}) \tag{2-62}$$

2.4.4 Case 4 (AC-DC-Buck DC)

In this case, the AC bus is connected to a buck DC bus through a DC line as shown in Figure 2-10.

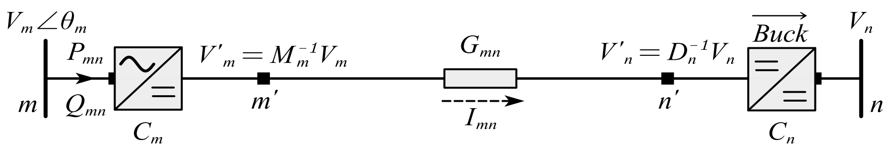

Figure 2-10. Case 4 (AC bus, DC line, Buck DC bus)

The line flows from AC side are given below.

$$P_{mn} = G_{mn}(M_m^{-2}V_m^2 - M_m^{-1}V_mD_n^{-1}V_n)\times(\frac{\alpha_m}{\eta_{mn}} + \beta_m\eta_{nm})$$

(2-63)

The expression in (2.63) only considered AC/DC converter efficiency as the equation is derived from AC side. The reactive power flow can be calculated as described in the previous cases (see Eqn. 2-51). The values of converter efficiency coefficients will be as given in (2-52). Partial derivatives for the active power with respect to the possible unknowns can be written as follows.

$$\frac{\partial P_{mn}}{\partial V_m} = G_{mn}(2M_m^{-2}V_m - M_m^{-1}D_n^{-1}V_n) \times (\frac{\alpha_m}{\eta_{mn}} + \beta_m \eta_{nm}) \tag{2-64}$$

$$\frac{\partial P_{mn}}{\partial V_n} = G_{mn}(-M_m^{-1}V_m D_n^{-1}) \times (\frac{\alpha_m}{\eta_{mn}} + \beta_m \eta_{nm}) \tag{2-65}$$

$$\frac{\partial P_{mn}}{\partial M_m} = G_{mn}(-2M_m^{-3}V_m^2 + M_m^{-2}V_m D_n^{-1}V_n) \times (\frac{\alpha_m}{\eta_{mn}} + \beta_m \eta_{nm}) \tag{2-66}$$

$$\frac{\partial P_{mn}}{\partial D_n} = G_{mn}(M_m^{-1}V_m D_n^{-2}V_n) \times (\frac{\alpha_m}{\eta_{mn}} + \beta_m \eta_{nm}) \tag{2-67}$$

2.4.5 Case 5 (AC-DC-Boost DC)

In this case, the AC bus is connected to a boost DC bus through a DC line as shown in Figure 2-11.

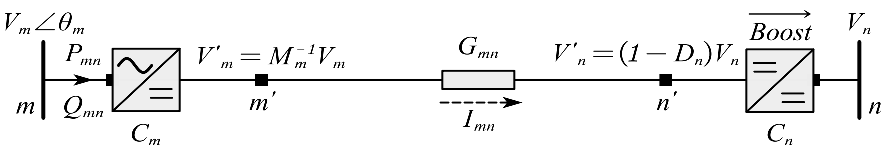

Figure 2-11. Case 5 (AC bus, DC line, Boost DC bus)

The line flows from the AC side are given below.

$$P_{mn} = G_{mn}(M_m^{-2}V_m^2 - M_m^{-1}V_m(1-D_n)V_n) \times (\frac{\alpha_m}{\eta_{mn}} + \beta_m \eta_{nm}) \tag{2-68}$$

The values of converter efficiency coefficients will be as given in (2.52). Partial derivatives for the active power are given below.

$$\frac{\partial P_{mn}}{\partial V_m} = G_{mn}(M_m^{-2} \times 2V_m - M_m^{-1}(1-D_n)V_n) \times (\frac{\alpha_m}{\eta_{rec}} + \beta_m \eta_{inv}) \tag{2-69}$$

$$\frac{\partial P_{mn}}{\partial V_n} = G_{mn}(-M_m^{-1}V_m(1-D_n)) \times (\frac{\alpha_m}{\eta_{rec}} + \beta_m \eta_{inv}) \tag{2-70}$$

$$\frac{\partial P_{mn}}{\partial M_m} = G_{mn}(-2M_m^{-3}V_m^2 + M_m^{-2}V_m(1-D_n)V_n)\times(\frac{\alpha_m}{\eta_{rec}} + \beta_m\eta_{inv}) \tag{2-71}$$

$$\frac{\partial P_{mn}}{\partial D_n} = G_{mn}(M_m^{-1}V_mV_n)\times(\frac{\alpha_m}{\eta_{rec}} + \beta_m\eta_{inv}) \tag{2-72}$$

2.4.6 Case 6 (AC-DC-Buck-Boost DC)

In this case, the AC bus is connected to a buck-boost DC bus through a DC line as shown in Figure 2-12.

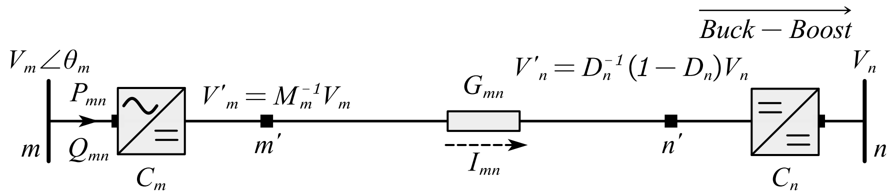

Figure 2-12 Case 6 (AC bus, DC line, Buck-Boost DC bus)

The line flows and partial derivatives of the possible unknowns are given below.

$$P_{mn} = G_{mn}(M_m^{-2}V_m^2 - (M_m^{-1}V_mD_n^{-1}(1-D_n)V_n))\times(\frac{\alpha_m}{\eta_{rec}} + \beta_m\eta_{inv}) \tag{2-73}$$

$$\frac{\partial P_{mn}}{\partial V_m} = G_{mn}(M_m^{-2}\times 2V_m - M_m^{-1}(1-D_n)V_n)\times(\frac{\alpha_m}{\eta_{rec}} + \beta_m\eta_{inv}) \tag{2-74}$$

$$\frac{\partial P_{mn}}{\partial V_n} = G_{mn}(-M_m^{-1}V_m(1-D_n))\times(\frac{\alpha_m}{\eta_{rec}} + \beta_m\eta_{inv}) \tag{2-75}$$

$$\frac{\partial P_{mn}}{\partial M_m} = G_{mn}(-2M_m^{-3}V_m^2 + M_m^{-2}V_m(1-D_n)V_n)\times(\frac{\alpha_m}{\eta_{rec}} + \beta_m\eta_{inv}) \tag{2-76}$$

$$\frac{\partial P_{mn}}{\partial D_n} = G_{mn}(M_m^{-1}V_mV_n)\times(\frac{\alpha_m}{\eta_{rec}} + \beta_m\eta_{inv}) \tag{2-77}$$

2.4.7 Case 7 (DC-DC-AC)

In this case, the DC bus is connected to an AC bus through a DC line as shown Figure 2-13. Basically, this configuration is a mirror image of case 3, but this time equations are derived from the DC side. Furthermore, there is no converter connected to the DC bus and the efficiency constants are omitted in this derivation. As the derivation is from the DC side, the reactive power is not defined, and the related term is set to zero in the formulation.

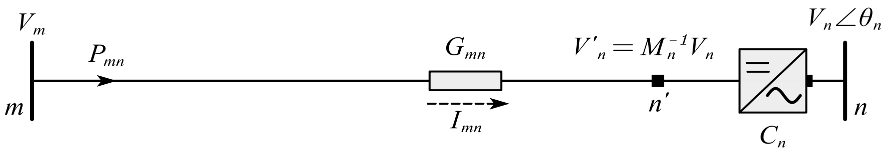

Figure 2-13. Case 7 (DC bus, DC line, AC bus)

The line flows and partial derivatives of the possible unknowns are given below.

$$P_{mn} = G_{mn}(V_m^2 - V_m M_n^{-1} V_n) \tag{2-78}$$

$$Q_m = Q_{mn} = 0 \tag{2-79}$$

$$\frac{\partial P_{mn}}{\partial V_m} = G_{mn}(2V_m - M_n^{-1}V_n) \tag{2-80}$$

$$\frac{\partial P_{mn}}{\partial V_n} = G_{mn}(-M_n^{-1}V_m) \tag{2-81}$$

$$\frac{\partial P_{mn}}{\partial M_n} = G_{mn}(M_n^{-2}V_m V_n) \tag{2-82}$$

2.4.8 Case 8 (Buck DC-DC-AC)

This case is the mirror image of case 4. The equations are derived from the DC side as shown in Figure 2-14, and only the DC/DC converter efficiency parameters are considered in this formulation.

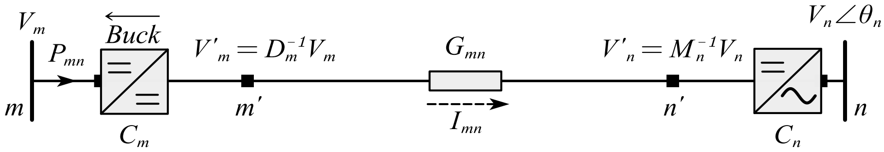

Figure 2-14. Case 8 (Buck DC bus, DC line, AC bus)

The line flows and partial derivatives of the possible unknowns are given below.

$$P_{mn} = G_{mn}(D_m^{-2}V_m^2 - D_m^{-1}V_m M_n^{-1}V_n) \times (\frac{\alpha_m}{\eta_{mn}} + \beta_m \eta_{nm}) \tag{2-83}$$

$$\frac{\partial P_{mn}}{\partial V_m} = G_{mn}(2D_m^{-2}V_m - D_m^{-1}M_n^{-1}V_n) \times (\frac{\alpha_m}{\eta_{mn}} + \beta_m \eta_{nm}) \tag{2-84}$$

$$\frac{\partial P_{mn}}{\partial V_n} = G_{mn}(-D_m^{-1}V_m M_n^{-1}) \times (\frac{\alpha_m}{\eta_{mn}} + \beta_m \eta_{nm}) \tag{2-85}$$

$$\frac{\partial P_{mn}}{\partial D_m} = G_{mn}(-2D_m^{-3}V_m^2 + D_m^{-2}V_m M_n^{-1}V_n) \times (\frac{\alpha_m}{\eta_{mn}} + \beta_m \eta_{nm}) \tag{2-86}$$

$$\frac{\partial P_{mn}}{\partial M_n} = G_{mn}(D_m^{-1}V_m M_n^{-2}V_n) \times (\frac{\alpha_m}{\eta_{mn}} + \beta_m \eta_{nm}) \tag{2-87}$$

The α_m, β_m are the DC converter efficiency parameter and their value depends on the direction of the power flow as given below.

$$\begin{aligned} (\alpha,\beta) &= (1,0) \quad \rightarrow \quad V_m' < V_n' \\ (\alpha,\beta) &= (0,1) \quad \rightarrow \quad V_m' < V_n' \\ (\alpha,\beta) &= (\tfrac{1}{2},\tfrac{1}{2}) \quad \rightarrow \quad V_m' = V_n' \end{aligned} \tag{2-88}$$

The subscripts with converter efficiency indicate the direction of the power flow ("*mn*" means the direction is from sending bus towards receiving bus and vice versa).

2.4.9 Case 9 (Boost DC-DC-AC)

This case is the mirror image of case 5 and the equations are derived from DC side as shown in Figure 2-15.

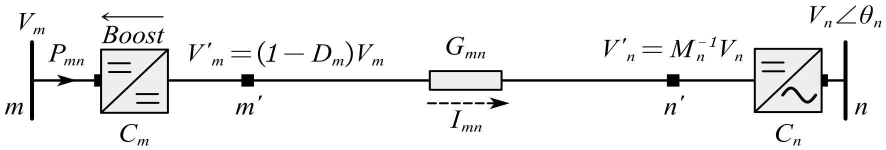

Figure 2-15. Case 9 (Boost DC bus, DC line, AC bus)

The line flows and partial derivatives of the possible unknowns are given below.

$$P_{mn} = G_{mn}((1-D_m)^2 V_m^2 - (1-D_m)V_m M_n^{-1}V_n) \times (\frac{\alpha_m}{\eta_{mn}} + \beta_m \eta_{nm}) \tag{2-89}$$

$$\frac{\partial P_{mn}}{\partial V_m} = G_{mn}(2(1-D_m)^2 V_m - (1-D_m)M_n^{-1}V_n) \times (\frac{\alpha_m}{\eta_{mn}} + \beta_m \eta_{nm}) \tag{2-90}$$

$$\frac{\partial P_{mn}}{\partial V_n} = G_{mn}(-V_m(1-D_m)M_n^{-1}) \times (\frac{\alpha_m}{\eta_{mn}} + \beta_m \eta_{nm}) \tag{2-91}$$

$$\frac{\partial P_{mn}}{\partial D_m} = G_{mn}(-2(1-D_m)V_m^2 + V_m M_n^{-1}V_n) \times (\frac{\alpha_m}{\eta_{mn}} + \beta_m \eta_{nm}) \tag{2-92}$$

$$\frac{\partial P_{mn}}{\partial M_n} = G_{mn}((1-D_m)V_m M_n^{-2}V_n) \times (\frac{\alpha_m}{\eta_{mn}} + \beta_m \eta_{nm}) \tag{2-93}$$

2.4.10 Case 10 (Buck-Boost DC- DC-AC)

This case is the mirror image of case 6 and equations are derived from the DC side as shown in Figure 2-16. The line flows and partial derivatives of the possible unknowns are given below.

$$P_{mn} = G_{mn}\left(\frac{(1-D_m)^2}{D_m^2}V_m^2 - \frac{(1-D_m)}{D_m}V_m\frac{1}{M_n}V_n\right)\times\left(\frac{\alpha_m}{\eta_{mn}}+\beta_m\eta_{nm}\right) \tag{2-94}$$

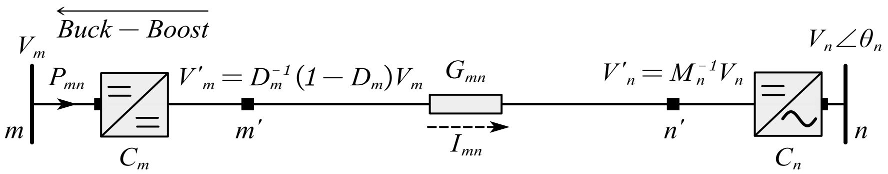

Figure 2-16. Case 10 (Buck-Boost DC bus, DC line, AC bus)

$$\frac{\partial P_{mn}}{\partial V_m} = G_{mn}\left(2\frac{(1-D_m)^2}{D_m^2}V_m - \frac{(1-D_m)}{D_m}\frac{1}{M_n}V_n\right)\times\left(\frac{\alpha_m}{\eta_{mn}}+\beta_m\eta_{nm}\right) \tag{2-95}$$

$$\frac{\partial P_{mn}}{\partial D_m} = G_{mn}\left[-2V_m^2\left(\left(\frac{(1-D_m)}{D_m^2}\right)+\left(\frac{(1-D_m)^2}{D_m^3}\right)\right)-V_mV_n\frac{1}{M_n}\left(\frac{1}{D_m}+\frac{(1-D_m)}{D_m^2}\right)\right]\left(\frac{\alpha_m}{\eta_{mn}}+\beta_m\eta_{nm}\right) \tag{2-96}$$

$$\frac{\partial P_{mn}}{\partial M_n} = G_{mn}\left(\frac{(1-D_m)}{D_m}V_m\frac{1}{M_n^2}V_n\right)\times\left(\frac{\alpha_m}{\eta_{mn}}+\beta_m\eta_{nm}\right) \tag{2-97}$$

2.4.11 Case 11 (DC-DC-DC)

In this case, the unknown variables are only the voltage magnitudes of the buses. The configuration is shown in Figure 2-17.

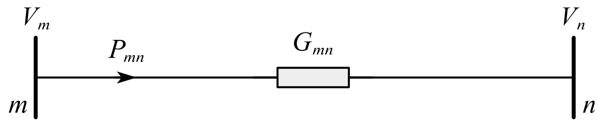

Figure 2-17. Case 11 (DC bus, DC line, DC bus)

The line flows and partial derivatives of the possible unknowns are given below.

$$P_{mn} = G_{mn}(V_m^2 - V_mV_n) \tag{2-98}$$

$$\frac{\partial P_{mn}}{\partial V_m} = G_{mn}(2V_m - V_n) \tag{2-99}$$

$$\frac{\partial P_{mn}}{\partial V_n} = G_{mn}(-V_n) \tag{2-100}$$

2.4.12 Case 12 (Buck DC – DC-DC)

In this case, the DC buck bus is connected to a DC bus through a DC line as shown in Figure 2-18. The line flows and partial derivatives of the possible unknowns are given below.

$$P_{mn} = G_{mn}(D_m^{-2}V_m^2 - D_m^{-1}V_mV_n)\times(\frac{\alpha_m}{\eta_{mn}} + \beta_m\eta_{nm}) \tag{2-101}$$

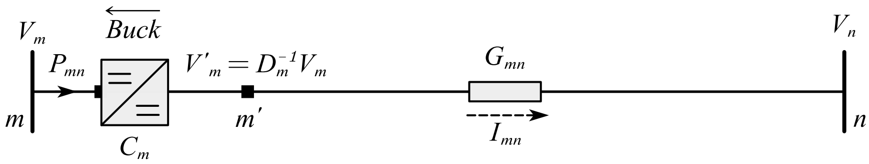

Figure 2-18. Case 12 (Buck DC bus, DC line, DC bus)

$$\frac{\partial P_{mn}}{\partial V_m} = G_{mn}(2D_m^{-2}V_m - D_m^{-1}V_n)\times(\frac{\alpha_m}{\eta_{mn}} + \beta_m\eta_{nm}) \tag{2-102}$$

$$\frac{\partial P_{mn}}{\partial V_n} = G_{mn}(-D_m^{-1}V_m)\times(\frac{\alpha_m}{\eta_{mn}} + \beta_m\eta_{nm}) \tag{2-103}$$

$$\frac{\partial P_{mn}}{\partial D_m} = G_{mn}(-2D_m^{-3}V_m^2 + D_m^{-2}V_mV_n)\times(\frac{\alpha_m}{\eta_{mn}} + \beta_m\eta_{nm}) \tag{2-104}$$

2.4.13 Case 13 (Boost DC – DC-DC)

In this case, the DC boost bus is connected to a DC bus through a DC line as shown in Figure 2-19. The line flows and partial derivatives of the possible unknowns are given below.

$$P_{mn} = G_{mn}(V_m^2(1-D_m)^2 - V_m(1-D_m)V_n)\times(\frac{\alpha_m}{\eta_{mn}} + \beta_m\eta_{nm}) \tag{2-105}$$

$$\frac{\partial P_{mn}}{\partial V_m} = G_{mn}(2V_m(1-D_m)^2 - (1-D_m)V_n)\times(\frac{\alpha_m}{\eta_{mn}} + \beta_m\eta_{nm}) \tag{2-106}$$

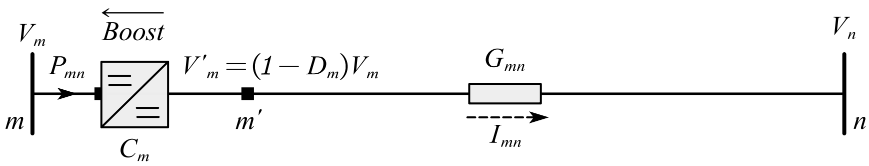

Figure 2-19. Case 13 (Boost DC bus, DC line, DC bus)

$$\frac{\partial P_{mn}}{\partial V_n} = G_{mn}(-V_m(1-D_m))\times(\frac{\alpha_m}{\eta_{mn}} + \beta_m\eta_{nm}) \tag{2-107}$$

$$\frac{\partial P_{mn}}{\partial D_m} = G_{mn}(-2V_m^2(1-D_m)+V_mV_n)\times(\frac{\alpha_m}{\eta_{mn}}+\beta_m\eta_{nm}) \tag{2-108}$$

2.4.14 Case 14 (Buck-Boost DC – DC-DC)

In this case, the DC buck-boost bus is connected to a DC bus through a DC line as shown in Figure 2-20.

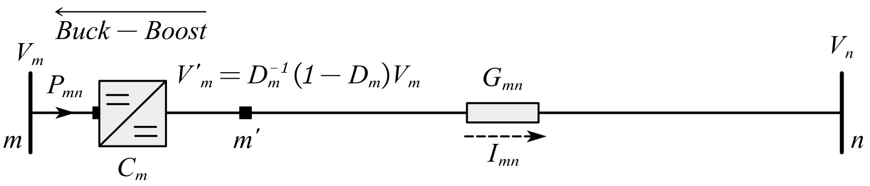

Figure 2-20. Case 14 (Buck-Boost DC bus, DC line, DC bus)

The line flows and partial derivatives of the possible unknowns are given below.

$$P_{mn} = G_{mn}(V_m^2\left(\frac{1-D_m}{D_m}\right)^2 - V_m\left(\frac{1-D_m}{D_m}\right)V_n)\times(\frac{\alpha_m}{\eta_{mn}}+\beta_m\eta_{nm}) \tag{2-109}$$

$$\frac{\partial P_{mn}}{\partial V_m} = G_{mn}(2V_m\left(\frac{1-D_m}{D_m}\right)^2 - \left(\frac{1-D_m}{D_m}\right)V_n)\times(\frac{\alpha_m}{\eta_{mn}}+\beta_m\eta_{nm}) \tag{2-110}$$

$$\frac{\partial P_{mn}}{\partial V_n} = G_{mn}\left(-V_m\left(\frac{1-D_m}{D_m}\right)\right)\times(\frac{\alpha_m}{\eta_{mn}}+\beta_m\eta_{nm}) \tag{2-111}$$

2.4.15 Case 15 (DC – DC- Buck DC)

In this case, the DC bus is connected to a buck DC bus through a DC line as shown in Figure 2-21. This is the mirror image of case 12, but in this case the equations are derived from the other side (the bus not connected to the converter).

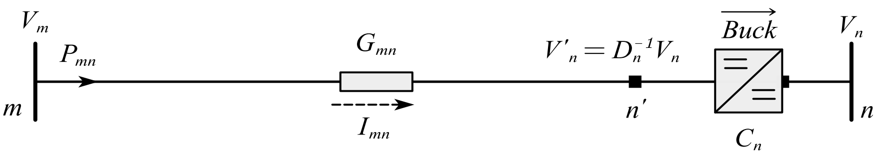

Figure 2-21. Case 15 (DC bus, DC line, Buck DC bus)

The line flows and partial derivatives of the possible unknowns are given below.

$$P_{mn} = G_{mn}(V_m^2 - V_mD_n^{-1}V_n) \tag{2-112}$$

$$\frac{\partial P_{mn}}{\partial V_m} = G_{mn}(2V_m - D_n^{-1}V_n) \tag{2-113}$$

$$\frac{\partial P_{mn}}{\partial V_n} = G_{mn}(-V_m D_n^{-1}) \tag{2-114}$$

$$\frac{\partial P_{mn}}{\partial D_n} = G_{mn}(V_m D_n^{-2} V_n) \tag{2-115}$$

2.4.16 Case 16 (DC – DC- Boost DC)

In this case, the DC bus is connected to a boost DC bus through a DC line as shown in Figure 2-22. This is the mirror image of case13. The line flows and partial derivatives of the possible unknowns are given below.

$$P_{mn} = G_{mn}(V_m^2 - V_m(1-D_n)V_n) \tag{2-116}$$

$$\frac{\partial P_{mn}}{\partial V_m} = G_{mn}(2V_m - (1-D_n)V_n) \tag{2-117}$$

$$\frac{\partial P_{mn}}{\partial V_n} = G_{mn}(-V_m(1-D_n)) \tag{2-118}$$

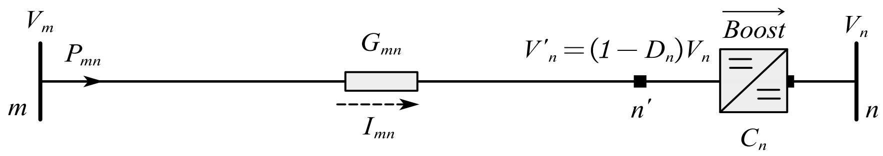

Figure 2-22. Case 16 (DC bus, DC line, Boost DC bus)

2.4.17 Case 17 (DC – DC- Boost DC)

In this case, the DC bus is connected to a boost DC bus through a DC line as shown in Figure 2-23. This is the mirror image of case14.

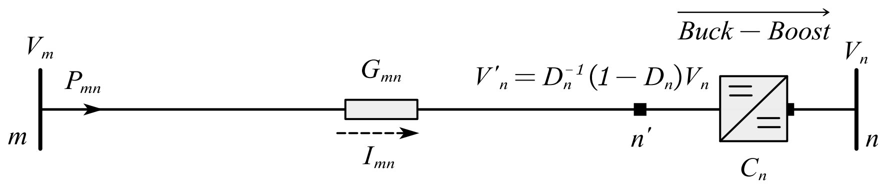

Figure 2-23. Case 17 (DC bus, DC line, Buck-Boost DC bus)

The line flows and partial derivatives of the possible unknowns are given below.

$$P_{mn} = G_{mn}(V_m^2 - V_m D_n^{-1}(1-D_n)V_n) \tag{2-119}$$

$$\frac{\partial P_{mn}}{\partial V_m} = G_{mn}(2V_m - D_n^{-1}(1-D_n)V_n) \tag{2-120}$$

$$\frac{\partial P_{mn}}{\partial V_n} = G_{mn}(-V_m D_n^{-1}(1 - D_n)) \tag{2-121}$$

$$\frac{\partial P_{mn}}{\partial D_n} = G_{mn}\left(V_m\left(\frac{1}{D_n} + \frac{1 - D_n}{D_n^2}\right)V_n\right) \tag{2-122}$$

2.5 Solid-State Transformer (SST) Model

2.5.1 SST Background

The solid-state transformer (SST) is a versatile device that can offer new power quality solutions to the future smart grids. McMurray initially suggested the notion of SST in 1968, proposing a device based on solid-state switches with high frequency isolation that behaves like a conventional transformer [114]. The practical use for SST emerged in the 1990s, in traction systems where weight and volume reduction is essential. The SST is capable of compensating voltage sags and harmonic distortion, interconnecting asynchronous networks, interfacing DC and A) port(s), compensating reactive power, regulating voltage magnitude, isolating disturbances from source and load or vice versa, and eliminates the need for mechanical actuators or tap changers.

A DN that has both Low Voltage DC (LVDC) and Medium Voltage DC (MVDC) buses and DC units connected to LVDC such as PV, ESSs, and DC loads. In such circumstances, no galvanic isolation is maintained, and two power conversion stages are required to connect the DC units to the MVDC network. As a result, more converters are required, which raises the overall cost. Reference [115] suggested a novel multiport DC SST (M-DC-SST) to interface the DC units directly to the MVDC bus. On the MV side of the MVDC bus, multiple modules are connected in series, but on the LV side of the M-DC-SST, the DC units are connected independently. The proposed approach connects the DC units to the MVDC bus without using an additional converter or an LVDC bus, saving money and lowering the number of converters when compared to a DC-DN without SST. The SST technology is one of the developing technologies that will be used widely in the future to integrate LV and MV networks with control circuitries and power electronics converters, thereby facilitating the integration of RESs in smart grid applications [116]. The increasing electrification of transportation and heating will impose a greater demand on LV networks, which could cause MV/LV transformers and LV cables to become overloaded. Deploying an SST at MV/LV substations and utilizing LVDC DNs have the potential to effectively address these issues.

The SST has many advantages over the conventional transformer, but it also brings some operational challenges. For instance, accurate SST modelling in PF calculation. The SST model in OpenDSS [117] is case specific and offers limited SST control options. A planning approach based on particle swarm optimization (PSO) is presented for optimally locating and sizing SST installations with the objective of reducing radial DN losses in [118]. This research also investigated various reactive power support schemes of SST. The PF solution in [118] is based on BFS method. However, the BFS method has topological limitations and lacks generality [76].

The MANA is a powerful technique in electric circuit analysis [66]. The MANA formulation is explored in literature for PF studies due to its flexibility to model any arbitrary device with arbitrary constraints [76, 96, 97]. As MANA formulation is superior to the traditional NA formulation [105], SST model is developed with MANA. The representation of losses is a facet of the SST that needs special consideration. An SST model capable of estimating the SST losses for all operating scenarios (including load and generation mode) is a topic under research which needs further investigation. The SST losses are extremely dependent on the SST configuration and switching strategies of the semiconductors. Consequently, the purpose of this study is to propose a general SST PF model with MANA formulation that could reflect any SST configuration.

The detailed model of the commonly used three-stage SST is shown in Figure 2-24, while Figure 2-25 shows the simplified models of different SSTs. TABLE 2-1 provides an overview of the converter ratings and functionalities of each stage. It should be noted that each stage of the SST may have different power ratings.

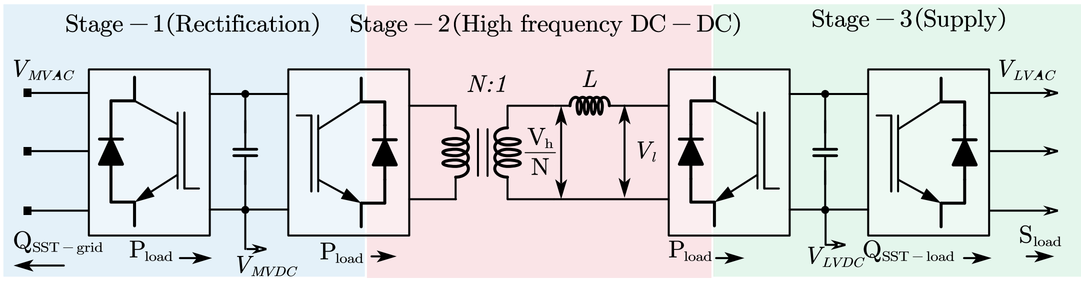

Figure 2-24. Three-stage SST model

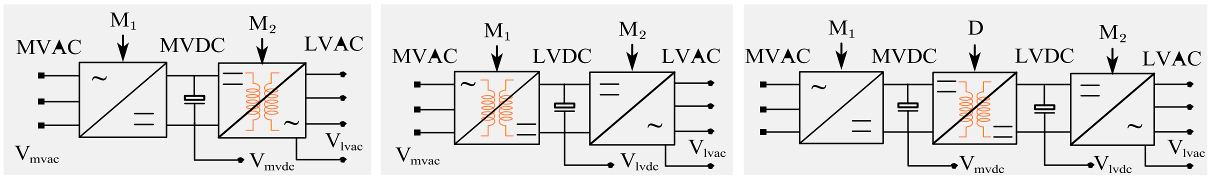

(a) (b) (c)

Figure 2-25. Simplified SST models: (a) two-stage SST with MV DC-link; (b) two-stage SST with LV DC-link; (c) three-stage SST with MV and LV DC-links.

TABLE 2-1. SST functionalities and ratings overview

Stage	Function	Input	Output	Rating
1	Controlled rectification	MVAC	MVDC	$\sqrt{P_{load}^2 + Q_{SST-Grid}^2}$
2	DC-DC conversion	MVDC	LVDC	P_{load}
3	Load supply voltage	LVDC	LVAC	S_{load}

2.5.2 SST PF model

To derive the PF formulation, consider the connections of three stage SST as shown in Figure 2-26. The first two topologies in Figure 2-25 can easily be extracted from the presented formulation. The objective is to calculate the total power injection at sending bus.

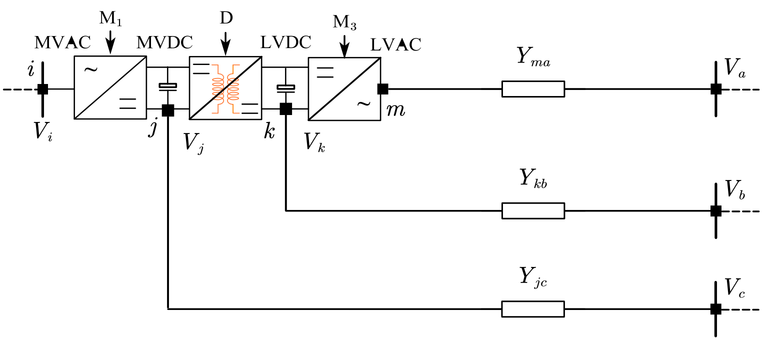

Figure 2-26. SST connection in a hybrid AC/DC network

The voltage and power relationships between different stages are given below.

Stage 1:

$$V_j = \varsigma_1 M_1^{-1} V_{i,LL_{rms}} \tag{2-123}$$

where, M_1 is the modulation index and ς_1 is the converter constant of stage 1 converter.

$$V_{base}^{mvdc} = \varsigma_1 V_{base}^{mvac} \tag{2-124}$$

With the above base selection, 1 *pu* AC voltage become equal to 1 *pu* DC voltage at $M_1 = 1$. The relationship between the DC power and AC active power is a function of rectifier efficiency as given below.

$$P_i = \eta_1^{-1} P_j \tag{2-125}$$

Stage 2:

$$V_k = DV_j \tag{2-126}$$

$$P_j = \eta_2^{-1} P_k \tag{2-127}$$

Stage 3:

$$V_{m,LL_{rms}} = \varsigma_3 M_3^{-1} V_k \tag{2-128}$$

where M_3 is the modulation index and ς_3 is the converter constant of stage 3 converter.

$$V_{base}^{lvdc} = \varsigma_3 V_{base}^{lvac} \tag{2-129}$$

With the above base selection, 1 *pu* AC voltage become equal to 1 *pu* DC voltage at $M_3 = 1$. The relationship between DC power and AC active power is a function of rectifier efficiency as given below.

$$P_k = \eta_3 P_m \tag{2-130}$$

Finally, overall efficiency of the SST can be calculated as follows.

$$\eta_{SST} = \eta_3 / \eta_1 \eta_2 \tag{2-131}$$

The above expressions are derived for the load model of SST and can be modified easily for the generation mode as explained in next section.

2.5.3 Line flows with SST

The objective is to calculate the total power injection at each bus. Due to multiple SST connections between the buses, the line flows and their associated partial derivatives are summed up instead of conventional power injection equation. The total power injection at bus "*i*" in Figure 2-26 is given below.

$$P_i = P_{ia} + P_{ib} + P_{ic} \tag{2-132}$$

$$P_{ia} = Y_{ma}\,\eta_{SST}\left(M_3^2 V_m^2 - M_3 V_m V_a\right) \tag{2-133}$$

$$P_{ib} = Y_{kb}\,/\eta_1\,\eta_2\left(D^2 V_k^2 - D V_k V_b\right) \tag{2-134}$$

$$P_{ic} = Y_{jc}\,/\eta_1\,\left(M_1^{-2} V_j^2 - M_1^{-1} V_j V_c\right) \tag{2-135}$$

2.5.4 SST load and generation models

As seen in Figure 2-27, the SST acts as a two-terminal element. The secondary LV side provides both active and reactive power to the LV loads while maintaining the secondary terminal's voltage constant (for example, at 1 *pu*). The SST requires only the active power from the primary MV side. Due to the dual directionality of the SST, there are two distinct operating modes: load and generation.

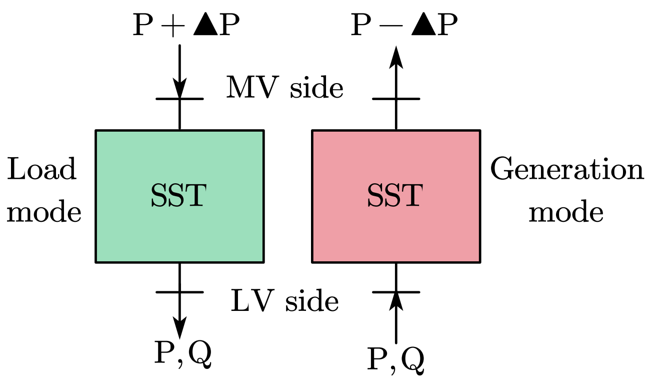

Figure 2-27. Load and generation modes of SST

The basic relationships between the active powers at both sides of the SST for the load and generation modes are as follows:

$$P_p = P_{s/\eta_{SST}}\ ;\ Q_p = 0\ \text{ Load mode} \tag{2-136}$$

$$P_p = \eta_{SST} P_s\ ;\ Q_p = 0\ \text{ Generation mode} \tag{2-137}$$

where, subscripts *p* and *s* are the primary (MV) and secondary (LV) terminals of the SST.

2.6 Load Model

Three types of load models are common in a typical DN [3]:

1. Constant power load (CPL)
2. Constant current load (CCL)
3. Constant impedance load (CIL)

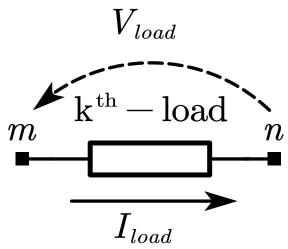

Figure 2-28. Generic load model

Consider the generic load model illustrated in Figure 2-28, where *m* and *n* represent the bus numbers and *k* represent the load index. The direction of the load current is determined by the arrow from bus *m* to bus *n*. The equations that define the load model are given below.

$$P_k^{(t)} = P_{rated}\left(\frac{\left|\vec{V}_{load}^{(t)}\right|}{V_{rated}}\right)^{\lambda_p} \tag{2-138}$$

$$Q_k^{(t)} = Q_{rated}\left(\frac{\left|\vec{V}_{load}^{(t)}\right|}{V_{rated}}\right)^{\lambda_q} \tag{2-139}$$

where, $P_k^{(t)}$ and $Q_k^{(t)}$ are the real and reactive power constraints for the k^{th} load at t^{th} iteration; P_{rated} and Q_{rated} are the real and reactive power ratings at rated voltage (V_{rated}); λ_p and λ_q are the load characteristics such that:

For CPL: $\lambda_p = \lambda_q = 0$;

For CCL: $\lambda_p = \lambda_q = 1$;

For CIL: $\lambda_p = \lambda_q = 2$;

The load constraint equation will remain the same for all types of loads. If k_p and k_q are the indices for the real and reactive power constraint $\boldsymbol{f}_L$, and the real and reactive power load constraints can be written as follows.

$$\mathbf{f}_{\mathrm{L}}(k_p) = P_k^{(t)} - \mathrm{Re}(\vec{\mathrm{I}}_{load}^{*}\vec{\mathrm{V}}_{load}) \tag{2-140}$$

$$\mathbf{f}_{\mathrm{L}}(k_q) = Q_k^{(t)} - \mathrm{Img}(\vec{\mathrm{I}}_{load}^{*}\vec{\mathrm{V}}_{load}) \tag{2-141}$$

where, “Re”, and “Img” are the real and imaginary parts respectively.

The load voltage and current in Figure 2-28 can be expressed in terms of the circuit unknowns as follows.

$$\vec{V}_{load} = \vec{V}_m - \vec{V}_n \tag{2-142}$$

The load current is also an independent variable in MANA formulation.

$$I_{load} = \vec{\mathbf{I}}_{\mathrm{L}}(k) \tag{2-143}$$

The load model developed for a load connected between two buses of the circuit. If a load is connected between a bus and the ground (single phase AC or DC networks), the terms which contains *n* will disappear.

2.7 Chapter Summary

In this chapter, various component models are developed for both DC and hybrid AC/DC networks. These models encompass DC/DC and AC/DC converters, SST, and load model, accounting for all potential interconnections within DC/DC or hybrid AC/DC network configurations. Subsequently, these models are utilized in the following chapters for PFA employing both derivative-based (MANA) and non-derivative-based (graph-theory) methods.

CHAPTER 3. Graph Theory Based PF Solvers for DC Grids

3.1 Introduction to graphs and graph Laplacians

Before moving towards the PF formulation, it is important to get familiar with basic graph-theory terminology and concepts.

3.1.1 Graphs

A "directed graph" is a pair $G = (V, E)$, where $V = \{v_1, \ldots, v_m\}$ is set of "nodes" or "vertices", and $E \subseteq V \times V$ is a set of ordered pairs of distinct nodes knows as "edges" (e.g., pairs $(u, v) \in V \times V$ with $u \neq v$). As an edge is a pair (u, v) with $u \neq v$, so there will be no self-loops. Moreover, there will be at most one edge from node u to node v.

For every node $v \in V$, the degree $d(v)$ of v is the number of edges leaving or entering v as defined below.

$$d(v) = \left| \left\{ u \in V \,\middle|\, (v,u) \in E \ or \ (u,v) \in E \right\} \right| \tag{3-1}$$

The "degree matrix" D of graph G is a diagonal matrix as defined below.

$$D(G) = \operatorname{diag}(d_1, \cdots, d_m) \tag{3-2}$$

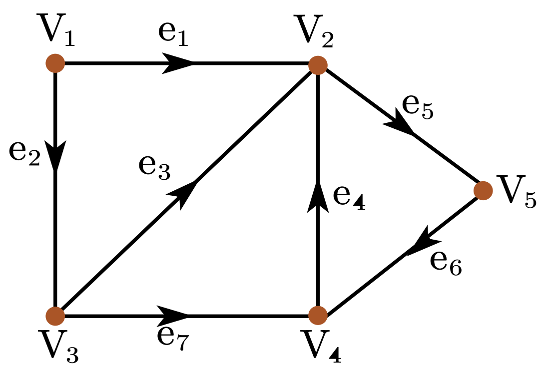

Figure 3-1. Arbitrary graph G

For directed graph shown in Figure 3-1 the degree matrix will be as follows.

$$\mathrm{D(G)} = \begin{bmatrix} 2 & 0 & 0 & 0 & 0 \\ 0 & 4 & 0 & 0 & 0 \\ 0 & 0 & 3 & 0 & 0 \\ 0 & 0 & 0 & 3 & 0 \\ 0 & 0 & 0 & 0 & 2 \end{bmatrix} \tag{3-3}$$

For a directed graph $G = (V, E)$, for any nodes $u, v \in V$, a "path" from u to v is a sequence of nodes $(v_0, v_1, \dots, v_k)$ such that $v_0 = u, v_k = v$, and (v_i, v_{i+1}) is an edge in E for all i with $0 \leq i \leq k-1$. The integer k is the "length" of the path. For a closed path $u = v$. The graph G is strongly connected if for any two distinct nodes $u, v \in V$, and there is a path from u to v and there is path from v to u as well.
Mostly authors use "walk" instead of "path" in graph-theory.

3.1.2 Incidence matrix

For any edge $e = u, v$, let $s(e) = u$ be the "source" of edge e and $t(e) = v$ be the "target" of edge e. For a graph $G = (V, E)$, with $V = \{v_1, \dots, v_m\}$, if $E = \{e_1, \dots, e_n\}$, then the "incidence matrix" or "connectivity matrix" (C) of graph G will be as follows with $m \times n$ dimensions.

$$c_{ij} = \begin{cases} +1 \text{ if } e_{\mathrm{j}} = \{v_i, v_k\} \text{ for some } k \\ 0 \qquad \text{otherwisew.} \end{cases} \tag{3-4}$$

Unlike the case of directed graphs, the entries in the incidence matrix of undirected graph are nonnegative.

3.1.3 Adjacency matrix

For both directed and undirected graphs, the concept of an adjacency matrix is fundamentally the same. For a given graph (directed or undirected) $G = (V, E)$, with $V = \{v_1, \dots, v_m\}$, the adjacency matrix *A*(*G*) is the symmetric $m \times m$ matrix (a_{ij}) such that.

- For directed graph

$$a_{ij} = \begin{cases} +1 \text{ if there is some edge} \left(v_i, v_j\right) || \left(v_j, v_i\right) \in E \\ 0 \qquad \text{otherwisew.} \end{cases} \tag{3-5}$$

- For undirected graph

$$a_{ij} = \begin{cases} +1 \text{ if there is some edge} \left(v_i, v_j\right) \in E \\ 0 \qquad \text{otherwisew.} \end{cases} \tag{3-6}$$

The adjacency matrix of graph shown in Figure 3-1 is given below.

$$A(G)=\begin{bmatrix} 0 & 1 & 1 & 0 & 0 \\ 1 & 0 & 1 & 1 & 1 \\ 1 & 1 & 0 & 1 & 0 \\ 0 & 1 & 1 & 0 & 1 \\ 0 & 1 & 0 & 1 & 0 \end{bmatrix} \tag{3-7}$$

3.1.4 Graph Laplacians

For a directed graph G if C is the incidence matrix, A is the adjacency matrix and D is the degree matrix such that $D_{ii} = D(v_i)$, then.

$$BB^{\mathrm{T}} = D - A \tag{3-8}$$

Thus, BB^T is independent of orientation of G and D-A is symmetric, positive, semidefinite (eigen values are real and non-negative).

The matrix $\Phi = BB^T = D - A$ is graph Laplacian of graph G.

3.2 LM based PF solver

Although graph-based methods have been previously reported in the literature for AC networks [119-124], their application to DC networks considering meshed configuration has not been studied. First, a formulation for radial networks is established, and then it is extended to mesh networks. The PF formulation is based on graph-theory with the following conditions.

C-1: The graph is connected and there is no islanding in the feeder which guarantees that the bus matrix is a non-singular matrix.

C-2: There is at least one CPL, and one constant voltage bus in the system, moreover constant voltage bus has the capability to provide the combined power demand of loads and network losses.

C-3: In steady state operation of the DC network, voltages remain within the boundary of $(0 < v_{min} \leq v \leq v_{max})$, this condition is required for voltage regulation and stability.

C-4: Short circuit currents are larger than the normal operating currents (this condition is a useful observation for any electrical power system and helpful in the proof of convergence).

3.2.1 Graph theory for DC grids

Let us consider a DC network with n number of nodes, b number of branches and l number of loops; for this network let us also define the primitive resistance matrix as follows.

$$\Re_p = \mathrm{diag}\left(\left[R_{12},\dots,R_{ij},\dots,R_{mn}\right]\right) \tag{3-9}$$

where, R_{ij} is the resistance of the branch connected between bus i and bus j and $\Re_p \in \mathbb{R}^{b\times b}$ space.

As we will modify AC networks to validate the PF solvers, we need equivalent DC resistance. The DC resistance can be calculated from AC resistance as follows [125].

$$R_{dc} = \frac{\pi r^2 - \pi(r-\delta)^2}{\pi r^2} R_{ac} \tag{3-10}$$

where R_{dc} is the DC resistance, R_{ac} is the AC resistance, δ is the skin depth of the conductor and r is the conductor radius.

Figure 3-2 shows the graph for an arbitrary simple DC network with 6 buses, 5 branches and 2 loops. By taking advantage of graph theory for the DC resistive network, a relationship can be developed between branch currents ($B \in \mathbb{R}^{b\times 1}$) and nodal injected currents ($I \in \mathbb{R}^{(n-1)\times 1}$) with an incidence matrix ($H \in \mathbb{R}^{b\times(n-1)}$).

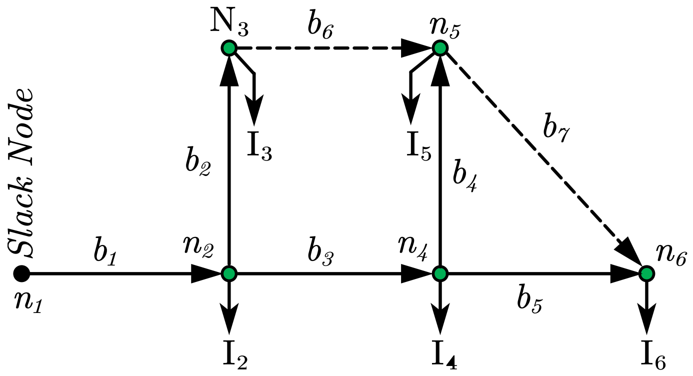

Figure 3-2. Graph of a simple DC network to demonstrate ILM formulation.

The algorithm to construct the incidence matrix H is as follows.

Step 1. Construct matrix $H \in \mathbb{R}^{b\times(n-1)}$ and fill it with zeros.

Step 2. Boolean ($H^n(i,j)$) = 1 if there is a path of length $1\leq n$ from bus i to bus j. Boolean ($H^n(i,j)$) = 0, otherwise

Step 3. Remove the first column from matrix H (i.e., the slack bus).

where, H^n is number of walks of length n from bus i to bus j.

3.2.2 PF Formulation for radial networks

The radial arrangement of Figure 3-2 would be revealed if the dashed lines are removed.

Using Kirchoff current law (KCL), an incidence matrix can be constructed as follows.

$$b_1 = I_2 + I_3 + I_4 + I_5 + I_6 \tag{3-11}$$

$$b_2 = I_3 \tag{3-12}$$

$$b_3 = I_4 + I_5 + I_6 \tag{3-13}$$

$$b_4 = I_5 \tag{3-14}$$

$$b_5 = I_6 \tag{3-15}$$

Writing above equation into matrix form, we get.

$$\begin{bmatrix} b_1 \\ b_2 \\ b_3 \\ b_4 \\ b_5 \end{bmatrix} = \begin{bmatrix} 1 & 1 & 1 & 1 & 1 \\ 0 & 1 & 0 & 0 & 0 \\ 0 & 0 & 1 & 1 & 1 \\ 0 & 0 & 0 & 1 & 0 \\ 0 & 0 & 0 & 0 & 1 \end{bmatrix} \begin{bmatrix} I_2 \\ I_3 \\ I_4 \\ I_5 \\ I_6 \end{bmatrix} \tag{3-16}$$

$$B = H \times I \tag{3-17}$$

For bus m its demand current can be written as follows.

$$I_m = a I_m^r + b I_m^i + c I_m^p \tag{3-18}$$

where r, i and p scripts stands for constant resistance, constant current, and constant power load respectively, and a, b, and c are the coefficients of constant resistance, constant current, and constant power load current percentage of consumption at bus m, respectively.

The sum of $a + b + c = 1$, such as for a CPL $a = b = 0$ and $c = 1$.

The injected current for bus m can be calculated as follows.

$$I_m = \text{-}inv\left[V_m\right] \times P_m \tag{3-19}$$

The net current for bus m for a RIP load model can be calculated as follows.

$$I_m = a_m g_m V_m + b_m \left|P_m\right| + c_m \left({P_m}/{V_m} \right) \tag{3-20}$$

The voltage drops on each branch can be calculated as follows.

$$\Delta \mathrm{V} = \Re_{\mathrm{p}} \times \mathrm{B} \tag{3-21}$$

where $\Delta V \in \mathbb{R}^{b \times 1}$ is the vector that contains the voltage drop of all branches.

The slack bus voltage (V_s) is known (by default equals to 1 *pu*). For the remaining buses, the voltage drops from a given bus to the slack bus can be calculated by applying the Kirchoff voltage law (KVL) on the closed paths in between the bus and slack bus.

$$V = V_s - H^T \times \Delta V \tag{3-22}$$

Note that matrix H is an upper triangular matrix, hence its transpose will be lower triangular matrix. From (3-17), (3-19), (3-21) and (3-22) we can get.

$$V = V_s + H^T \times \Re_p \times H \times I \tag{3-23}$$

Let us define Laplacian matrix (LM) as follows.

$$\Phi = H^T \times \Re_{\mathrm{p}} \times H \tag{3-24}$$

where Φ is a LM which is weighted by branch resistances of the network. For a connected network, Φ is always non-singular whether the incidence matrix H is a square matrix or not. Equation (3-23) can be re-written as follows.

$$V = V_s + \Phi \times I \tag{3-25}$$

Equation (3-25) is a non-linear expression for the PF solution of a radial DC network. The presence of CPLs in the network according to C-2, makes (3-25) nonlinear, which means it can only be solved by an iterative numerical method. The iterative solution updates the V vector as follows.

$$V^{(t+1)} = V_s + \Phi \times I^{(t)} \tag{3-26}$$

where *t* is the iteration count.

3.2.3 PF Formulation for meshed networks

Now let us consider Figure 3-2 with dashed lines (tie-lines) connected, which transforms the network architecture from radial to meshed. A new incidence matrix is required to model the loops created by tie-lines. The loops do not affect the bus current injection, but new branch currents need to be added in the network. Taking the new branches into account, the current injections of buses 3, 5 and 6 can be written as:

$$I_3^{new} = I_3 + B_6 \tag{3-27}$$

$$I_5^{new} = I_3 - B_6 + B_7 \tag{3-28}$$

$$I_6^{new} = I_6 - B_7 \quad (3\text{-}29)$$

By incorporating the loops in the formulation, the following expression is achieved.

$$B = H \times I + L \times B_l \quad (3\text{-}30)$$

where $L \in \mathbb{R}^{b\times l}$ is the second incidence matrix which contains the loops. $B_l \in \mathbb{R}^{l\times 1}$ is a vector of tie-line currents, and *l* is the number of tie-lines.

The matrix L can be constructed with the following algorithm.

Step 1. Construct the matrix $L \in \mathbb{R}^{b\times l}$ and fill it with zeros.

Step 2. For a tie-line between bus *m* and *n*, subtract column *m* in H from column *n* and place the result in column *l* of L.

Step 3. Repeat step-2 for all tie lines.

For the network shown in Figure 3-2, the matrix L is given below.

$$[L] = \begin{bmatrix} 0 & 0 \\ 1 & 0 \\ -1 & 0 \\ -1 & 1 \\ 0 & -1 \end{bmatrix} \quad (3\text{-}31)$$

The voltage drops at tie-lines in each loop are calculated by applying KCL as follows.

$$B_6R_{35} - B_4R_{54} - B_3R_{42} + B_2R_{23} = 0 \quad (3\text{-}32)$$

$$B_7R_{56} - B_5R_{64} + B_4R_{45} = 0 \quad (3\text{-}33)$$

By using matrix L, a relationship is built for tie-line voltage drops as follows.

$$\begin{bmatrix} 0 & 1 & -1 & -1 & 0 \\ 0 & 0 & 0 & 1 & -1 \end{bmatrix} \times \Re_p \times B + \begin{bmatrix} R_{35} & 0 \\ 0 & R_{56} \end{bmatrix} \times \begin{bmatrix} B_6 \\ B_7 \end{bmatrix} = \begin{bmatrix} 0 \\ 0 \end{bmatrix} \quad (3\text{-}34)$$

$$\mathrm{L}^{\mathrm{T}} \times \Re_p \times \mathrm{B} + \mathrm{R}_l \times \mathrm{B}_l = 0 \quad (3\text{-}35)$$

where, R_l is the diagonal matrix of the tie-line resistances.

It is possible to determine tie-line currents based on branch currents by rearranging (3-35).

$$S = \frac{H}{\left(U_b + L \times R^{-1} \times L^T \times \Re_p\right)} \quad (3\text{-}36)$$

Where, U_b is identity matrix of dimension b.

C-1 guarantees that the primitive resistive matrix is non-singular matrix, so its inverse exists. The relationship vector "B" between branch currents to nodal injection will take the following form.

$$B = S \times I \tag{3-37}$$

Finally, the PF equations for meshed configuration can be written as follows.

$$V^{(t+1)} = V_s + H^T \times \Re_p \times S \times I^{(t)} \tag{3-38}$$

$$I^{(t)} = -\left[\frac{P_m}{V_m^{(t)}}\right]_{\forall m \in (n-1)} \tag{3-39}$$

$$\Phi = H^T \times \Re_{\mathrm{p}} \times S \tag{3-40}$$

$$V^{(t+1)} = V_s + \Phi \times I^{(t)} \tag{3-41}$$

The PF expression in (3-41) is valid for both radial and meshed configurations. For radial network, the matrix S will be equal to matrix H. The matrices H and S remain constant during iterative process.

Total power loss of the network can be calculated as follows.

$$P_{loss} = B^T \times \Re_{\mathrm{p}} \times B \tag{3-42}$$

3.2.4 MATLAB Pseudo code of LM PF solver

TABLE 3-1 shows the MATLAB pseudo code of the proposed PF algorithm. Algorithm 1 starts with the flat start (FS) while algorithm 2 starts with random initial guess (within user defined specific range). As the bad initial guess may cause a divergence of the PF solution, the proposed algorithm is tested with random initial guess to test its robustness. In both algorithms "*l*" is the number of loops (for radial network the value of "*l*" will be zero).

3.2.5 Convergence proof of LM PF solver

A classical reference for the convergence includes contraction mapping [126], which is used to prove the existence and uniqueness of the PF solution. The contraction mapping has only fixed-point and according to BFPT, any contraction mapping on a non-empty metric space has a unique fixed point. Hence, a non-linear function converges to that unique point with an iterative process.

TABLE 3-1. MATLAB pseudo code of LM PF solver

Algorithm 1: flat start (1 pu)	**Algorithm 2:** random start

Data: Load the network data (n, b, l, P, $\Re_p$, R_l)
Construct and store H, B
Construct and store L, S, Φ
if (l == 0)
S = **H**; % Radial Network
else
S = **S**; % Meshed Network ($l > 0$)
end
Define: V = ones (n - 1, 1), (@ t = 0), ε, t_{max}, Vs = 1.
iter = 0;
tic
for t = 0: t_{max}
iter = *iter* + 1;
Calculate I^t from (3-39);
Evaluate V^{t+1} in (3-41);
if max ($\left\|V^{t+1}-V^{t}\right\| \le \varepsilon$)
return $V = V^{t+1}$
break
end
end
Processing_time = toc;
	Data: Load the network data (n, b, l, P, $\Re_p$, R_l)
	Construct and store H, B
	Construct and store L, S,
	if (l == 0)
	S = **H**; % Radial Network
	else
	S = **S**; % Meshed Network ($l > 0$)
	end
	Define: Vs = 1; t_{max}, ε;
	tic
	for m = 1: 20
	V = (1 + rand (n-1, 1) - 0.5) ; % @ t = 0,
	for t = 0: t_{max}
	Calculate I^t from (3-39);
	Evaluate V^{t+1} in (3-41);
	if max ($\left\|V^{t+1}-V^{t}\right\| \le \varepsilon$)
	return $V = V^{t+1}$
	break
	end
	error (m, t) = norm (($V^{t+1} - V^{t}$), inf);
	end
	end
	Processing_time = toc;

Remark 1: The matrix Φ is a LM which is weighted by network resistances. It has the characteristics of diagonal dominant and positive definite. Therefore, $|\varphi_{mm}| \geq |\varphi_{mn}|, \forall m \neq n$.

Equation (3-41) in terms of bus voltages can be written as.

$$V^{(t+1)} = V_s + \Phi \times \left[V^{(t)} \right]^{-1} \times P \tag{3-43}$$

Equation (3-43) is a recursive formulation of the PF problem; the BFPT [127-129] is used to prove the existence and uniqueness of (3-43).

Theorem: The recursive PF formulation in (3-43) is stable and a contraction mapping can be formed.

$$V^{(t+1)} = f(V^{(t)}) = V_s + \Phi \left[{P_m}/{V_m^{(t)}} \right]^{T}_{\forall m \in (n-1)} \tag{3-44}$$

For any V that contained in closed box $(0 \le v_{min} \le v \le v_{max})$ according to C-3, regardless of the initial condition, let $X \in \mathbb{R}^{(n-1)\times 1}$ be the solution of the PF, such that:

$$\left\| f\left(\mathrm{V}^{0}\right) - f\left(\mathrm{X}\right) \right\| \le \psi \left\| \mathrm{V}^{0} - \mathrm{X} \right\| \tag{3-45}$$

where, Ψ is a contraction constant also known as Lipschitz constant whose value lies between zero and one ($0 < \Psi \le 1$), and "≤" is called Lipschitz inequality.

Proof: Expression in (3-45) is a recursive function like BFPT, which is a mapping of "V" to itself. According to BFPT, the solution "X" of the PF problem satisfying $X = f(X)$, exists and is unique if and only if $f(V)$ is a contraction mapping on V. Fixed-point theorem is valid for any Banach algebra so from expression (3-44) and (3-45) following result can be deduced.

$$\left\| \mathrm{V}^{(t+1)} - \mathrm{X} \right\| = \left\| f\left(\mathrm{V}^{(t)}\right) - f\left(\mathrm{X}\right) \right\| = \left\| [\Phi][\mathrm{P}] \left[{}^{1}\!/_{\mathrm{X_m}} - {}^{1}\!/_{\mathrm{V_m^{(t)}}} \right]^{\mathrm{T}} \right\| \le \left\| [\Phi][\mathrm{P}] \left[\frac{\mathrm{V_m^{(t)}} - \mathrm{X_m}}{\mathrm{V_m^{(t)}}\mathrm{X_m}} \right]^{\mathrm{T}} \right\| \le \psi \left\| \mathrm{V}^{(t)} - \mathrm{X} \right\| \tag{3-46}$$

The contraction constant (Ψ) can be calculated as follows.

$$\Psi = \left\| \frac{\Phi \times \mathrm{P}}{v_{\min}^{2}} \right\| \tag{3-47}$$

As mentioned before Φ is a diagonal dominant matrix, that guarantees that $\|\Phi\| \le max\{\varphi_{mm}\}$, which allows us to rewrite (3-47) as follows.

$$\psi = max \left\| \frac{[\varphi_{\mathrm{mm}}][\mathrm{P_m}]}{v_{\min}^{2}} \right\|_{\forall m \in (n-1)} \tag{3-48}$$

where φ_{mm} is the Thevenin equivalent resistance.

The Lipschitz constant can be expressed in terms of maximum allowable load and short circuit current.

$$\psi = max \left\{ \frac{\mathrm{P}_m / v_{min}}{v_{min} / \varphi_{mm}} \right\} < 1 \tag{3-49}$$

Remark 2: The proof is completed here. From expression (3-49), it can be concluded that the value of contraction constant will be less than one as defined earlier in C-4 (short circuit current is greater than normal operation current).

Remark 3: From (3-46) and (3-48), it can be concluded that a PF solution may not be obtained when the value of Ψ approaches to unity. In addition, smaller $\Phi \times P$ means a smaller Ψ that implies a stronger network which allows a larger permissible region for the proposed method. The Lipschitz constant has physical meaning here which is directly related to the network configuration, loading conditions, and voltage limitations defined for a given network.

3.3 ILM based PF Solver

The LM based PF solver requires two incidence matrices to solve a meshed network [100]. This section proposes an improved formulation of the LM (ILM) PF solver for better computational speed. Let's consider the arbitrary DC-DN illustrated in Figure 3-3 with *N* number buses and *L* number of lines to demonstrate the ILM formulation.

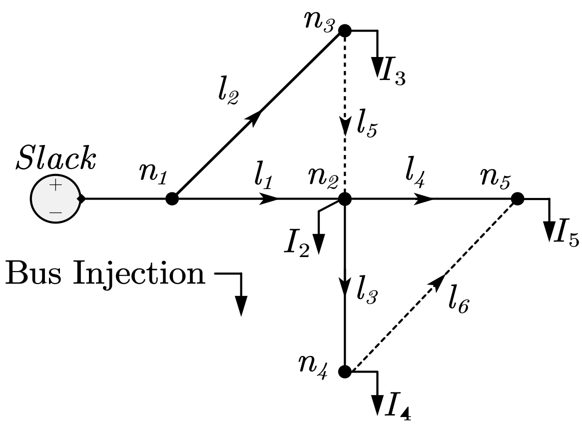

Figure 3-3. Arbitrary DC-DN to demonstrate ILM formulation.

The dotted lines in Figure 3-3 are tie lines that creates a meshed configuration. The main difference between the LM and ILM method is that the LM technique requires a separate connectivity matrix to accommodate loops, whereas the ILM method requires just one connectivity matrix to solve both radial and meshed networks.

The algorithm to construct the connectivity matrix is illustrated in Figure 3-4. If the network connections are assumed to be as shown in Figure 3-3, the connectivity matrix $C \in \mathbb{R}^{N \times L}$ for a radial network (ignoring dotted lines) will be as follows.

$$C = \begin{bmatrix} +1 & +1 & 0 & 0 \\ -1 & 0 & +1 & +1 \\ 0 & -1 & 0 & 0 \\ 0 & 0 & -1 & 0 \\ 0 & 0 & 0 & -1 \end{bmatrix} \tag{3-50}$$

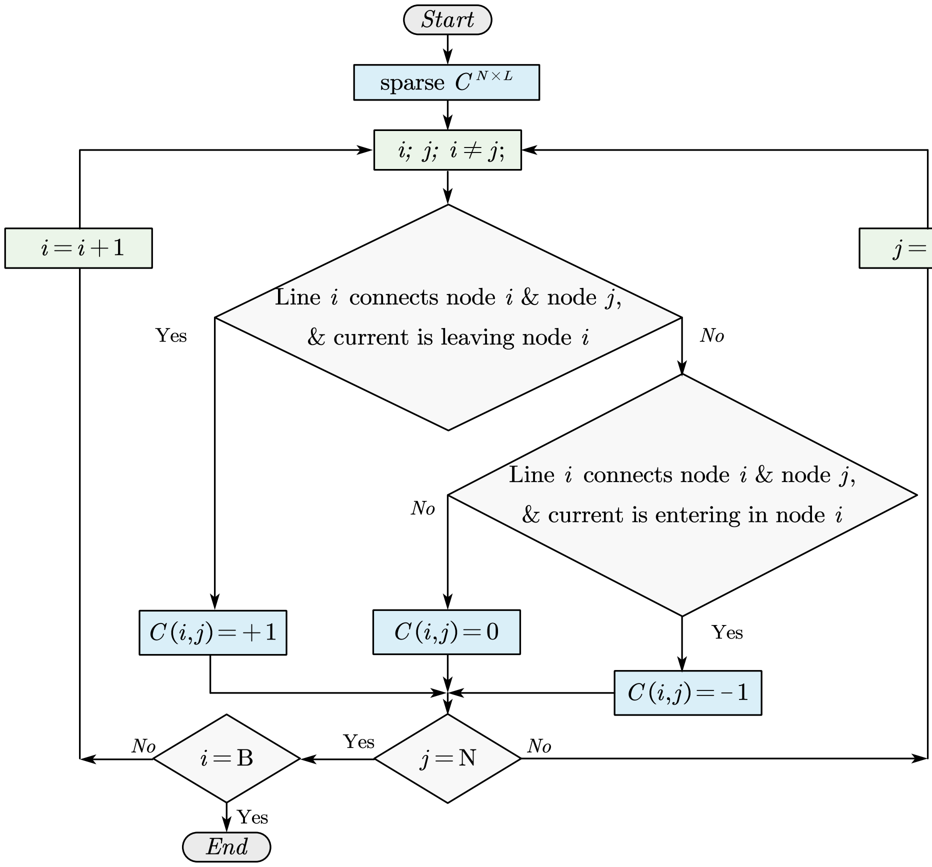

Figure 3-4. Algorithm to form connectivity matrix for ILM PF solver.

Now, if we consider the dotted lines in Figure 3-4, which transform the network into a meshed configuration, the modified connectivity will take the following form.

$$C = \begin{bmatrix} +1 & +1 & 0 & 0 & 0 & 0 \\ -1 & 0 & +1 & +1 & -1 & 0 \\ 0 & -1 & 0 & 0 & +1 & 0 \\ 0 & 0 & -1 & 0 & 0 & +1 \\ 0 & 0 & 0 & -1 & 0 & -1 \end{bmatrix} \tag{3-51}$$

Two important points to emphasize here, 1- The connectivity matrix of radial network is upper triangular matrix, while the connectivity matrix of meshed network is not upper triangular, 2- The entries in each column of connectivity matrix have equal number of positive and negative values. DC-DNs typically have two types of buses: viz; 1- Constant voltage bus (υ), 2- Constant power bus (ρ). According to the bus type, the connectivity matrix can be split into two sub matrices as follows.

$$C = \begin{bmatrix} C_{\upsilon} & C_{\rho} \end{bmatrix} \tag{3-52}$$

where, $C_{\upsilon} \in \mathbb{R}^{\upsilon \times L}$,$C_{\rho} \in \mathbb{R}^{\rho \times L}$ and $N = \rho + \upsilon$

The objective is to find the unknown voltage vector V_{ρ}, while V_{υ} is the known voltage vector. The relationship between branch currents and the bus injected currents can also be built using a connectivity matrix as follows.

$$I = C \times K \tag{3-53}$$

where, I is a vector of bus current injections ($I \in \mathbb{R}^{N \times 1}$) and K is a vector of branch currents ($K \in \mathbb{R}^{L \times 1}$).

The vector of bus injection currents I can be split into two sub-matrices as well, using the connectivity matrix corresponding to different bus types.

$$I = \begin{bmatrix} I_{\upsilon} & I_{\rho} \end{bmatrix} \tag{3-54}$$

where I_{υ} is the vector of the source currents of ideal voltage sources and I_{ρ} is the vector of the demand current of constant power buses.

If $\mathrm{G} = \Re^{-1}$, then the network resistance-weighted LM can be constructed as follows.

$$\Phi_{\rho\upsilon} = C_{\rho} \times G \times C_{\upsilon}^{T} \tag{3-55}$$

$$\Phi_{\rho\rho} = C_{\rho} \times G \times C_{\rho}^{T} \tag{3-56}$$

where,

$\Phi_{\rho\upsilon}$: all conductive couplings between constant voltage and constant power buses.

$\Phi_{\rho\rho}$: conductive couplings associated with constant power buses, also known as the demand matrix.

The injected current for a constant power bus in terms of bus voltages can be written as follows.

$$I_{\rho} = V_{\rho} \times \Phi_{\rho v} + V_{\rho} \times \Phi_{\rho\rho} \tag{3-57}$$

The goal is to solve for unknown voltages (V_{ρ}).

$$V_\rho = \left(\frac{1}{\Phi_{\rho\rho}} \times \frac{P_\rho}{diag(V_\rho)} \right) - \left(\frac{\Phi_{\rho v} \times V_v}{\Phi_{\rho\rho}} \right) \tag{3-58}$$

The power of a DG (P_{dg}) can be incorporated in the formulation easily as given below.

$$V_\rho = \left(\frac{1}{\Phi_{\rho\rho}} \times \frac{P_{dg} - P_\rho}{diag(V_\rho)} \right) - \left(\frac{\Phi_{\rho v} \times V_v}{\Phi_{\rho\rho}} \right) \tag{3-59}$$

With the presence of CPL in the network, the expression (3-59) becomes nonlinear and must be solved iteratively. Let us augment (3-59) with an iterative counter (t) that begins with a FS and iterates until the requisite convergence tolerance is met.

$$V_\rho^{(t+1)} = \left(\frac{1}{\Phi_{\rho\rho}} \times \frac{P_{dg} - P_\rho}{diag(V_\rho^{(t)})} \right) - \left(\frac{\Phi_{\rho v} \times V_v}{\Phi_{\rho\rho}} \right) \tag{3-60}$$

The flow chart of the proposed ILM PF solver is given in Figure 3-5.

3.3.1 Convergence proof of ILM-PF solver

The proof to guarantee the convergence given in section 3.2.5 holds true for this formulation as well, provided that the criteria established in section 3.2.5 are met. Furthermore $\Phi_{\rho\rho}$, is a diagonal dominant matrix.

The contraction constant for the ILM method can be written as follows.

$$\Psi = max \left\{ \frac{\left| P_{\rho(m)} \right|}{v_{min}} \Big/ \frac{v_{min}}{\Re_{thv(m,m)}} \right\} \forall m \in \rho \tag{3-61}$$

where, $\mathcal{R}_{thv(m,m)} = \Phi_{\rho(m,m)}^{-1}$ is the Thevenin equivalent resistance.

During normal operation, the load current is always less than the short-circuit current, which guarantees that $0 \leq \Psi \leq 1$. This implies that the recursive formulation converges to a unique PF solution. This observation is quite valuable, especially when several iterations are required for a PF solution. The value of contraction constant provides the insights on the allowable loading in terms of network parameters, for which the ILM method can ensure convergence. It is worth noting that the contraction constant can be calculated prior to execute the entire PF algorithm. Convergence cannot be ensured using the proposed method for any value of the contraction constant greater than unity. If such situation occurs, decreasing the load, increasing the generation, or finding an appropriate combination can be considered to ensure convergence. An updated PF algorithm to confirm the convergence of a given system is given in Figure 3-6.

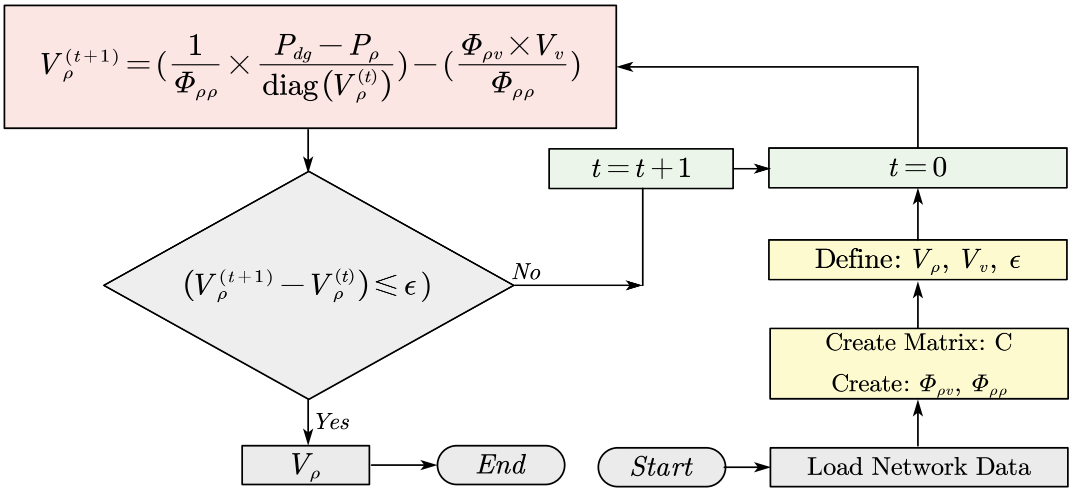

Figure 3-5. Flow chart of proposed ILM PF solver

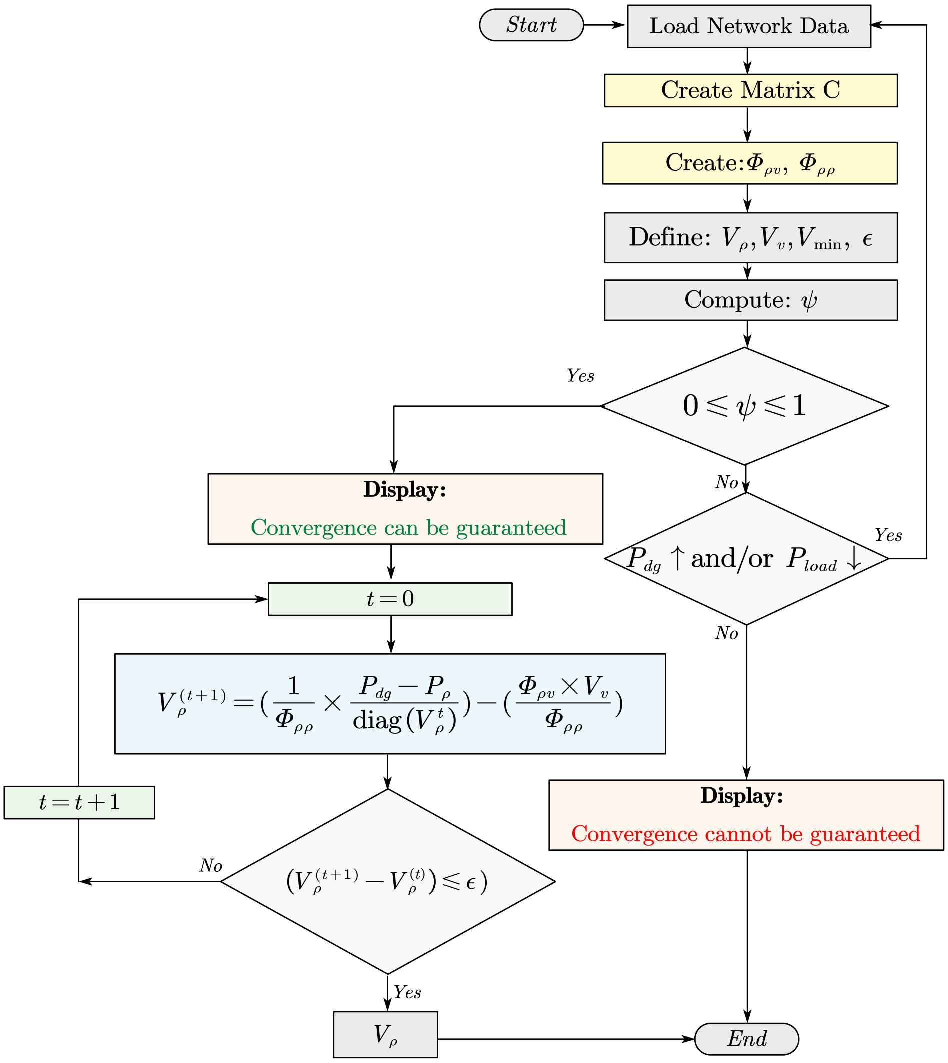

Figure 3-6. Updated ILM algorithm

3.4 Performance Comparison of LM and ILM PF solvers

A modified IEEE 33 bus test feeder is utilized to validate and compare the performance of PF solvers. The modified test feeder is shown in Figure 3-7 and its data can be found in Appendix A.

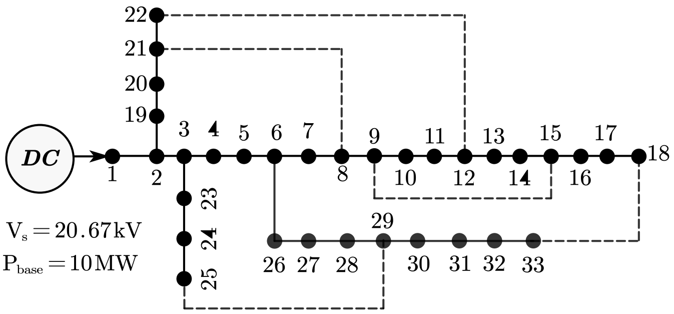

Figure 3-7. Modified IEEE 33 bus test feeder.

This is originally an AC feeder and it modified to DC feeder as follows.

1. The reactance of the lines is neglected.
2. Equivalent DC resistance of line is computed from AC resistance using following expression

$$R_{dc} = \frac{\pi r^2 - \pi\left(r-\delta\right)^2}{\pi r^2} \times R_{ac} \tag{3-62}$$

r: cross sectional area of the conductor, δ: skin depth of the conductor

3. Reactive power is set to zero.
4. Active AC loads are treated as constant power DC loads.
5. DC converters are added in the network.

Under various loading scenarios, the ILM and LM methods are compared in terms of CPU processing time and the number of iterations required. Figure 3-8 and show the error as a function of number of iterations required for both radial and meshed configurations at nominal loadings. For radial configuration, both solvers have the similar performance. However, the ILM outperforms the LM method in terms of number of iterations required to achieve the required accuracy threshold for a meshed network.

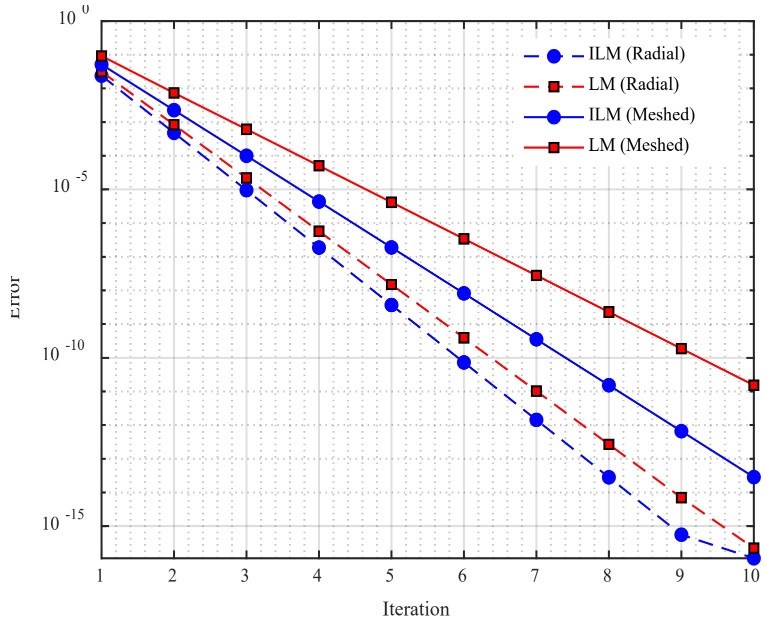

Figure 3-8. Performance comparison of LM and ILM at nominal loadings (error as a function of iterations)

It should be noted that ILM requires one connectivity matrix to solve a meshed network whereas LM requires two matrices. This difference is more prominent under heavy loading conditions, as shown in Figure 3-9.

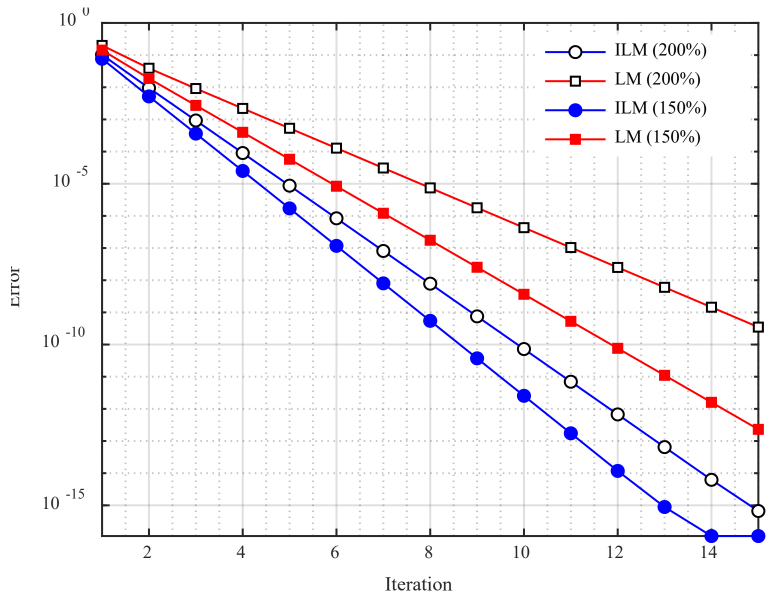

Figure 3-9. Performance comparison of LM and ILM at different loadings (error as a function of iterations)

The detailed comparison of both solvers in terms of number of iterations and CPU is presented in TABLE 3-2. The proposed ILM method converges faster than the LM method for a meshed configuration as expected.

TABLE 3-2. Detailed performance comparison of LM and ILM

Loading (%)	**Configuration**	**PF Method**	**Iterations**	**Time (*msec*)**
100	Radial	LM	7	1.815
		ILM	6	1.382
	Meshed	LM	10	1.904
		ILM	8	1.574
150	Radial	LM	8	1.857
		ILM	7	1.584
	Meshed	LM	12	2.104
		ILM	9	1.673
200	Radial	LM	10	2.016
		ILM	9	1.654
	Meshed	LM	16	2.517
		ILM	10	1.798

To ensure the unique PF solution, the plot of contraction constant at nominal and 250% loadings are illustrated in Figure 3-10.

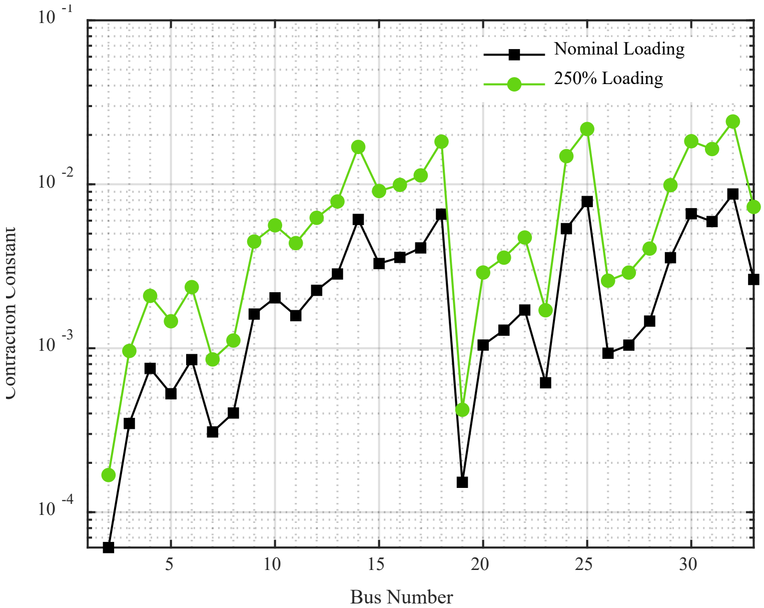

Figure 3-10. Value of contraction constant at each bus (Meshed Network)

The results shown in Figure 3-10 implies that the LM and ILM PF solvers can guarantee convergence even at heavy loading as long as the contraction constant value is within the limits. To evaluate the robustness of the proposed solvers, they are also tested with a random initial guess. Three random points ranging from 0.5 to 1.5 *pu* are considered, and for these random initial guesses, the PF algorithm is simulated for nominal and for 200% loading as shown in Figure 3-11.

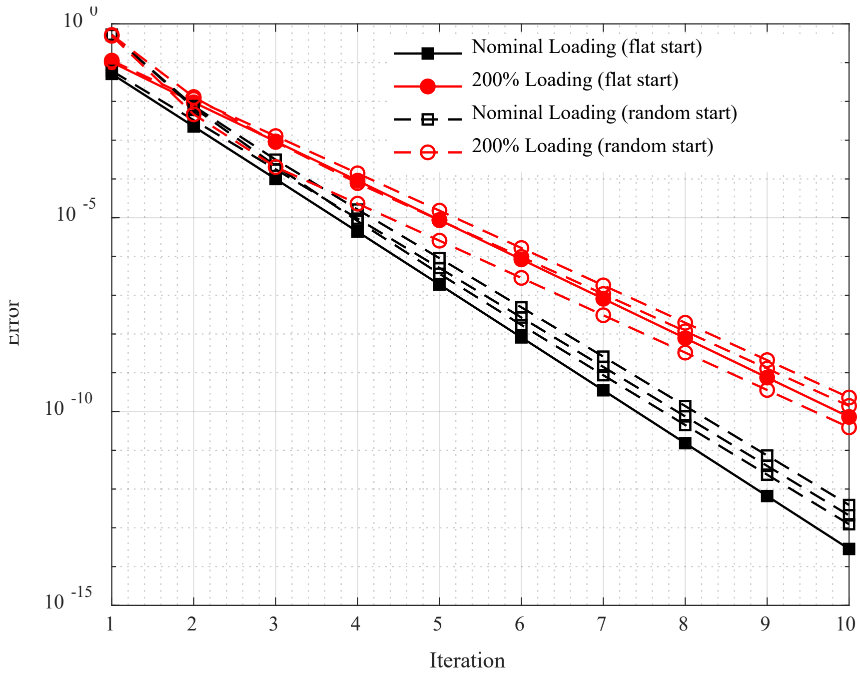

Figure 3-11. Convergence from random initial guesses

The proposed solvers converged with random initial guesses, for both nominal and high loading conditions. This implies that the proposed solvers are robust and can converge even without a FS.

3.5 Integration of DC/DC Converter Models into ILM Formulation

As shown in previous section, ILM has better performance compared to LM based PF solver. In this section DC/DC converter models developed in chapter 2 will be added into ILM formulation for a generalized ILM based PF solver for DC networks. This solver can handle any arbitrary DC network configuration. To generalize the formulation let's define some parameters.

m: sending bus (B).

n: Receiving bus.

L_{mn}: Line connecting bus m and n.

K: Binary bus type vector (simple DC or with Buck converter)

K = 0: for simple DC bus, K = 1: for Buck-DC bus

T: Binary bus type vector (simple DC or with Boost converter)

T = 0: for simple DC bus, T = 1: for Boost-DC bus

L: Binary line type matrix (simple DC line or with converter)

L_{mn} = 0: for simple DC line L_{mn} = 1 for DC line with converter

TABLE 3-3 shows the binary values for all possible connection in a DC network.

TABLE 3-3. Binary values for all possible interconnection in DC network

B_m	B_n	K_m	T_m	L_{mn}	K_n	T_n
DC	DC	0	0	0	0	0
Buck	DC	1	0	1	0	0
Boost	DC	0	1	1	0	0
Buck-Boost	DC	1	1	1	0	0
DC	Buck	0	0	1	1	0
DC	Boost	0	0	1	0	1
DC	Buck-Boost	0	0	1	1	1

The possible connections of loads (l) and generators (g) with a DC bus m are shown in Figure 3-12.

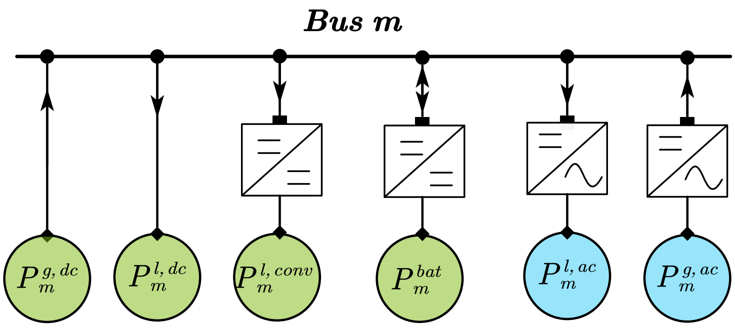

Figure 3-12. Possible load and generator connections with a DC bus

The general expression for the specified powers at bus m are as follows.

$$P_m^{sp} = \left(P_m^{g,dc} - P_m^{l,dc} - \frac{P_m^{l,conv}}{\eta_{m,conv}} - \gamma \frac{P_m^{bat}}{\eta_{m,ch}} + \bar{\gamma}\,\eta_{m,dis} P_m^{bat} + \eta_{m,rec} P_m^{g,ac} - \frac{P_m^{l,ac}}{\eta_{m,inv}} \right) \tag{3-63}$$

where, γ and $\bar{\gamma}$ are the binary coefficients for charging and discharging i.e., γ = 1 for charging and $\bar{\gamma} = 1 - \gamma$ for discharging. The scripts "*conv*", "*rec*" "*inv*", "*bat*", "*ch*" and "*dis*" indicate converter, rectifier, inverter, battery, charging, and discharging respectively. The bar on the binary elements in (3-63) and hereafter is used for their binary complement.

The possible interconnections between DC buses are shown in Figure 3-13. As the sending bus may have different types of connections with receiving buses, the summation of the line flows is used rather than the bus power injections.

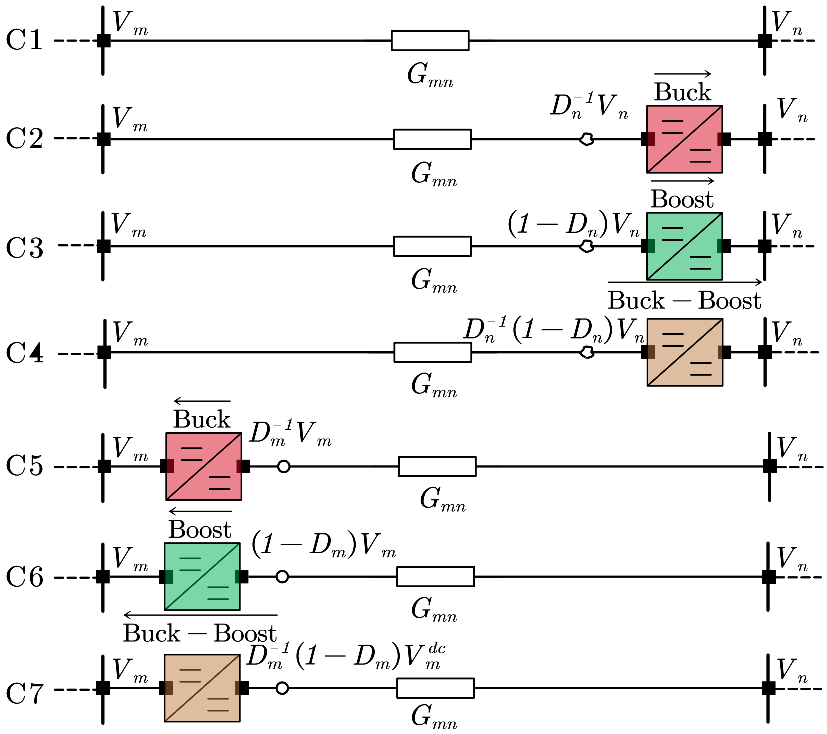

Figure 3-13. Possible interconnections between DC buses

The line flows for all possible interactions shown in Figure 3-13 can be found in Chapter 2 (Case 11 to Case 17). The active power is calculated (*cal*) using (3-64) at each iteration.

$$P_m^{cal} = \sum_{\substack{n=1 \\ n\neq m}}^{N} [C_{mn}] \begin{bmatrix} \bar{K}_m \bar{T}_m \bar{L}_{mn} \bar{K}_n \bar{T}_n \left[P_{mn}^{C1}\right] + K_m \bar{T}_m L_{mn} \bar{K}_n \bar{T}_n \left[P_{mn}^{C5}\right] \\ +\bar{K}_m T_m L_{mn} \bar{K}_n \bar{T}_n \left[P_{jk}^{C6}\right] + K_m T_m L_{mn} \bar{K}_n \bar{T}_n \left[P_{mn}^{C7}\right] \\ +\bar{K}_m \bar{T}_m L_{mn} K_n \bar{T}_n \left[P_{jk}^{C2}\right] + \bar{K}_m \bar{T}_m L_{mn} \bar{K}_n T_n \left[P_{mn}^{C3}\right] \\ +\bar{K}_n \bar{T}_m L_{mn} K_n T_n \left[P_{mn}^{C4}\right] \end{bmatrix} \tag{3-64}$$

Finally, the mismatch vector can be written in terms of network unknowns as follows.

$$F(V_\rho) = P_m^{sp} - P_m^{cal} \quad , \quad \forall m \in N \tag{3-65}$$

Please see Figure 3-6 for algorithm flow chart.

3.5.1 Test network and simulation results

To test the proposed method, a modified version of the IEEE 33 bus test feeder is simulated. The operating voltage of this test feeder is 20.67 kV DC, whereas voltage in buck, boost and buck-boost regions are 6.89 kV, 24.8 kV, and 22.7 kV, respectively as shown in Figure 3-14. The test feeder becomes radial when the dotted lines are out of service. The test feeder data can be found in Appendix A.

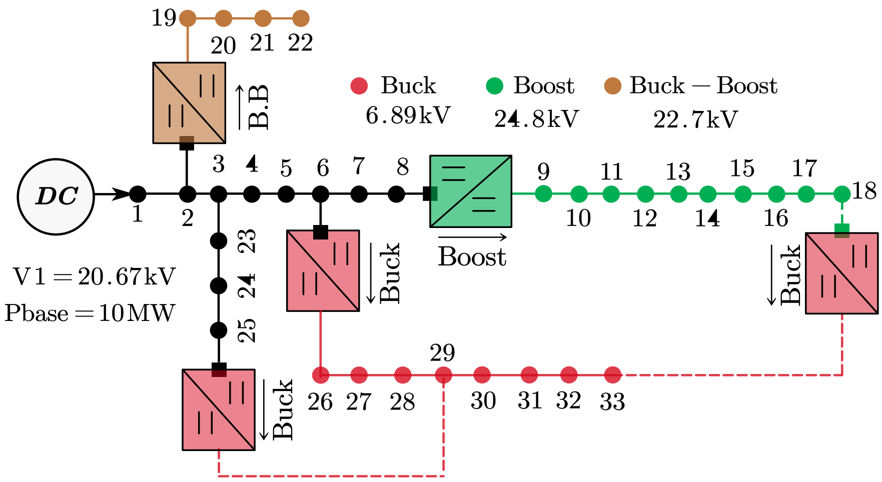

Figure 3-14. Modified IEEE 33 bus test feeder.

To validate the accuracy of the proposed method, the test network is also simulated in EMT software. The voltage profile of the test network shown in Figure 3-15 confirms the accuracy of the proposed method. The voltage profiles are plotted in *pu* and the different voltage bases are highlighted in Figure 3-15 with different marker styles.

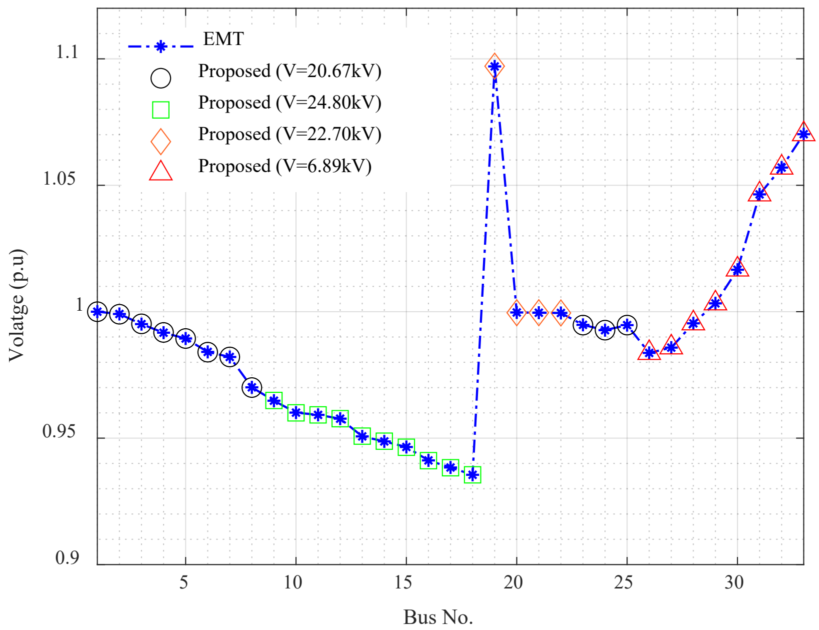

Figure 3-15. Voltage profiles of the test network

To evaluate the robustness of the proposed method, simulations are also performed under different loading conditions. Figure 3-16 shows the errors as a function of the number of iterations. The load is increased in 5 steps from the nominal load to 5 times, with a 100%

increase in each step. The convergence tolerance is set to 10^{-8}. Results in Figure 3-16 show that the proposed method converged in 5 iterations for nominal loading, and it successfully converged within 10 iterations even for stressed network. The convergence characteristics of the proposed algorithm are further investigated by calculating the contraction constant. Figure 3-17 shows the contraction constant values for various loading conditions at each bus. The convergence tolerance is set to 8 decimal places.

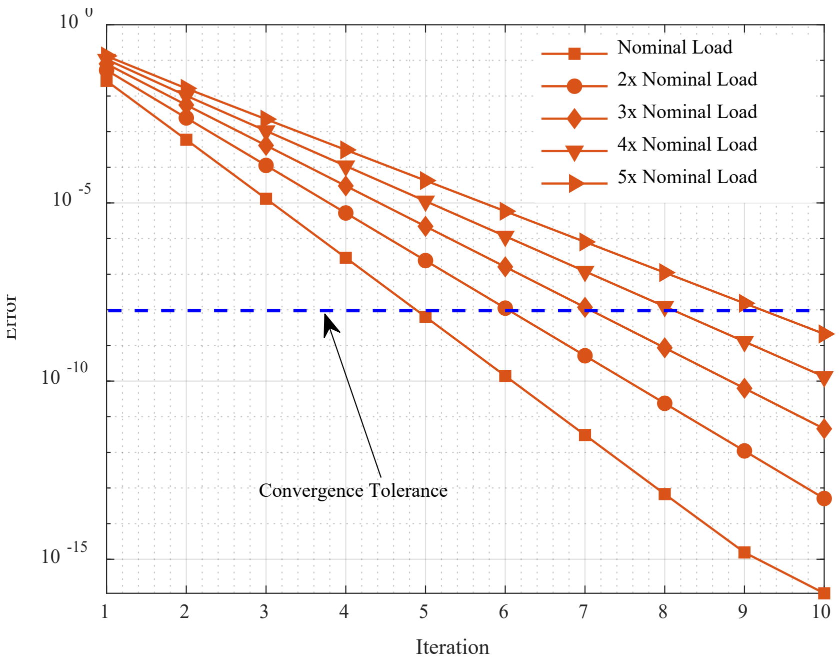

Figure 3-16. Errors as a function of number of iterations

The proposed solution will remain convergent as long as the contraction constant is less than unity. As illustrated in Figure 3-17, the maximum value of the contraction constant is less than unity even at 500% loading, indicating that the proposed method has the potential to achieve convergence in highly stressed networks. The bus number 25 has the highest value of contraction constant. The convergence of the proposed method is also tested with random initial guesses. To simulate the worst scenarios, 10 random points (between 1.5 *pu* and 0.5 *pu*) are chosen as initial guesses. As shown in Figure 3-18, for all the initial guesses, the proposed method converged successfully.

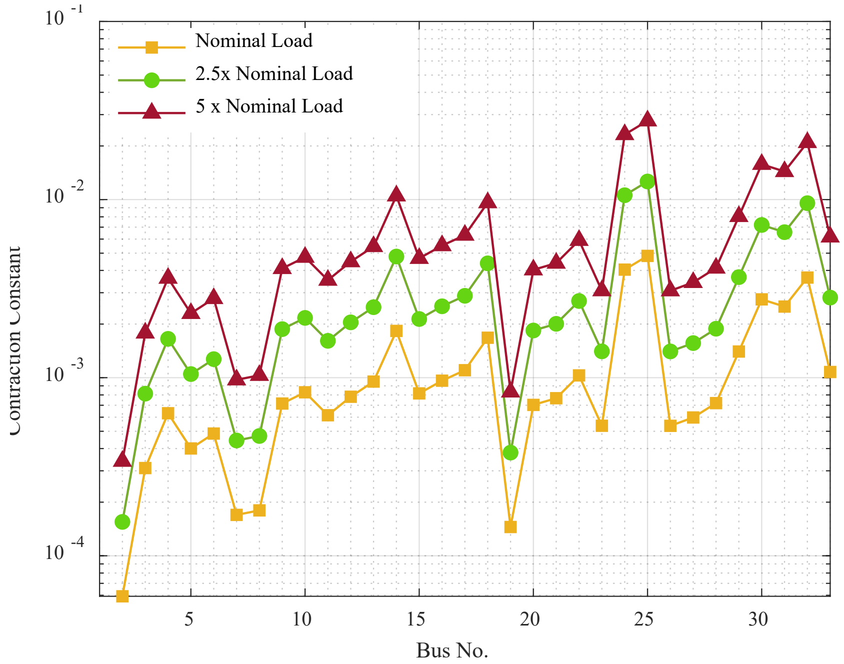

Figure 3-17. Value of Contraction Constant at each bus at different loadings

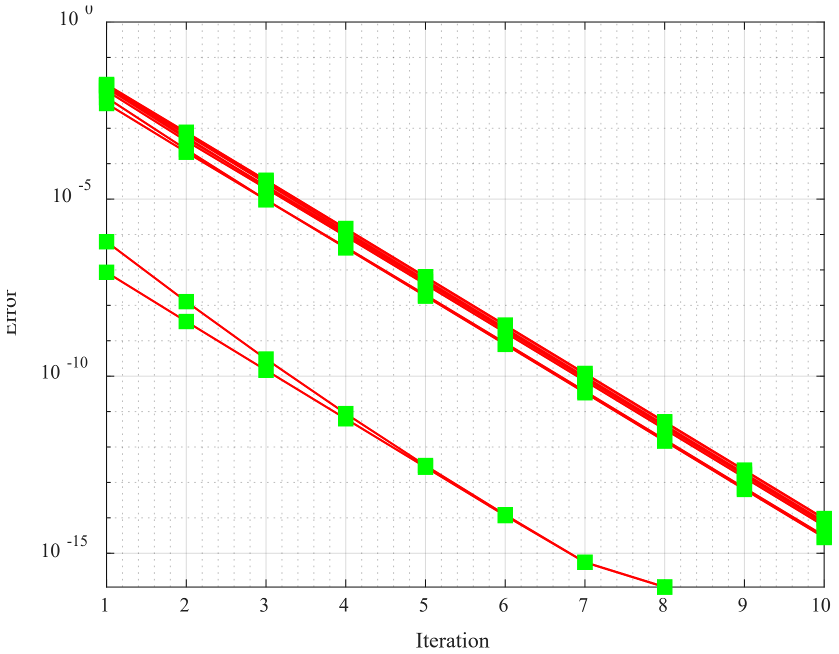

Figure 3-18. Convergence from random initial guesses (error as function of number of iterations)

3.6 Chapter Summary

Graph theory-based PF solvers are developed in this chapter for DC networks hosting CPLs. Results suggests that the proposed ILM outperforms the LM method in terms of number of iterations and processing time required to achieve the same level of accuracy. The reason for this improvement is that ILM can solve meshed networks with only one connectivity matrix, whereas LM requires two matrices. The convergence of these solvers has also been taken into consideration with the BFPT. This is a very useful observation that can be utilized to check the convergence criterion where a large number of iterations are required for a PF solution.

The convergence results are in agreement with the analytically evaluated guarantee of convergence using the BFPT for the proposed PF solvers. Furthermore, the robustness of these methods is demonstrated considering random initial guess and different loading conditions. The DC/DC converter models are also integrated into the ILM formulation to develop a generic PF solver. The formulation considers all the potential network topologies between DC buses.

3.7 Publications

[1] **Javid, Zahid**, Ulas Karaagac, Ilhan Kocar, and Ka Wing Chan. "Laplacian matrix-based power flow formulation for LVDC grids with radial and meshed configurations." *Energies* 14, no. 7 (2021): 1866.

[2] **Javid, Zahid**, Ulas Karaagac, and Ilhan Kocar. “Improved Laplacian Matrix based power flow solver for DC distribution networks.” *Energy Reports* 8 (2022): 528-537.

[3] **Javid, Zahid**, Tao Xue, Karaagac Ulas, and Ilhan Kocar. "Efficient Graph Theory Based Load Flow Solver for DC Distribution Networks Considering DC/DC Converter Models." *In 2022 IEEE 9th International Conference on Power Electronics Systems and Applications (PESA)*, pp. 1-5. IEEE, 2022.

CHAPTER 4. MANA Based PF Solver for DC Grids

In literature, either approximations are made, or non-derivative methods are utilized for the PF solution of DC-DNs. In this chapter, the PF method based on MANA formulation [65, 130] with NR algorithm is developed. MANA formulation method is capable of handling arbitrary network topologies and can be easily expanded to accommodate various network component models. It also avoids many theoretical complications by providing a systematic method for deriving the Jacobian matrix terms. The results are validated with EMT simulations and with HE-PFM [75]. The details of HE-PFM can be found in [74].

4.1 DC-MANA Formulation

The Jacobian matrix in MANA formulation can be expanded to accommodate independent device models and arbitrary constraints. The simplified version of MANA for a DC-DN can be written as follows.

$$\begin{bmatrix} G_{aug} & C_{\upsilon}^{T} \\ C_{\upsilon} & 0 \end{bmatrix} \begin{bmatrix} V_d \\ I_{\upsilon} \end{bmatrix} = \begin{bmatrix} I_d \\ V_{\upsilon} \end{bmatrix} \tag{4-1}$$

where G_{aug} is augmented conductance matrix (see Section 4.2.2). C_v is column of connectivity matrix that represents ideal voltage sources. I_d and V_d are the current and voltage of the demand buses respectively. I_v and V_v are the current and voltage of the ideal voltage sources respectively.

In the steady state form of MANA, the lines and the load contribute to the conductance matrix (G). A DC-DN can have three types of buses as shown in Figure 4-1viz: constant voltage (v), constant resistance (r), and constant power demand (d).

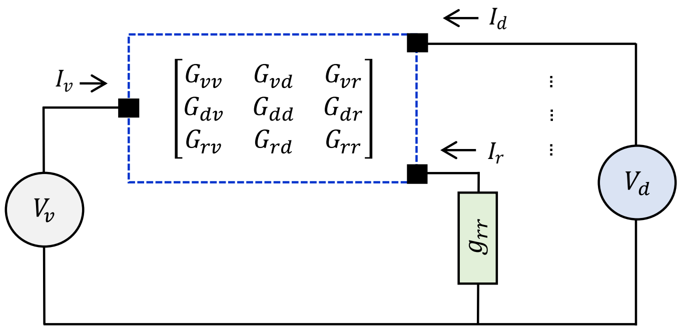

Figure 4-1. Type of buses in DC-DN

The DC network shown in Figure 4-1 can be formulated as follows.

$$\begin{bmatrix} I_\upsilon \\ I_d \\ I_r \end{bmatrix} = \begin{bmatrix} G_{\upsilon\upsilon} & G_{\upsilon d} & G_{\upsilon r} \\ G_{d\upsilon} & G_{dd} & G_{dr} \\ G_{r\upsilon} & G_{rd} & G_{rr} \end{bmatrix} \begin{bmatrix} V_\upsilon \\ V_d \\ V_r \end{bmatrix} \tag{4-2}$$

where,

G_{vv} : all conductive effects associated with constant voltage buses (v),

G_{dd} : all conductive effects associated with constant power buses (d),

G_{rr} : all conductive effect associated with constant resistance buses (r),

G_{vd} : all conductive coupling between v and d buses,

G_{vr} : all conductive coupling between v and r buses,

G_{dr} : all conductive coupling between d and r buses.

To remove the buses with zero current injection, the Kron`s reduction method can be used [131].

$$I_r = -g_{rr} \times V_r \tag{4-3}$$

New terms can be written as follows:

$$G_{d\upsilon} = G_{d\upsilon} - G_{dr}(G_{rr} + g_{rr})^{-1} G_{r\upsilon} \tag{4-4}$$

$$G_{dd} = G_{dd} - G_{dr}(G_{rr} + g_{rr})^{-1} G_{rd} \tag{4-5}$$

The injected current for demand buses can be written as follows.

$$I_d = G_{d\upsilon} \times V_\upsilon + G_{dd} \times V_d \tag{4-6}$$

4.1.1 Jacobian Formation in DC-MANA

MANA formulation allows to add arbitrary constraints into Jacobian matrix. This study considers the following constraints: the network Kirchoff’s current law, ideal voltage source constraint, and load constraint as given below.

$$f_{kcl}^{(t)} = [G \quad C_\upsilon^T \quad C_d] \begin{bmatrix} V_d \\ I_\upsilon \\ I_d \end{bmatrix}^{(t)} - I_d \tag{4-7}$$

$$f_\upsilon^{(t)} = C_\upsilon \times V_d^{(t)} - V_\upsilon \tag{4-8}$$

$$f_d^{(t)} = P_d^{sp} \left[\frac{V_d^{(t)}}{V_d^{sp}} \right]^\lambda - \left(V_d \times I_d \right)^{(t)} \tag{4-9}$$

where C_d is the connectivity matrix terms for constant power demand buses and λ is the type of the load defined in Chapter 2, Section 2.6.

The expressions (4-7) to (4-9) forms the Jacobian matrix of MANA as given below:

$$\begin{bmatrix} G & C_{\upsilon}^{T} & C_d \\ C_{\upsilon} & 0 & 0 \\ \dfrac{\partial f_d}{\partial V_d} & 0 & \dfrac{\partial f_d}{\partial I_d} \end{bmatrix}^{(t)} \begin{bmatrix} \Delta V_d \\ \Delta I_{\upsilon} \\ \Delta I_d \end{bmatrix}^{(t)} = -\begin{bmatrix} f_{kcl} \\ f_v \\ f_d \end{bmatrix} \tag{4-10}$$

The generalized expression for the load constraint matrix f_d and its partial derivatives for all type of loads are written as follows.

$$\frac{\partial f_d}{\partial V_d} = \left(\lambda \times P_{rated} \times \frac{\left(V_d\right)^{\frac{\lambda}{2}-1}}{\left(V_{rated}\right)^{\lambda}} \right) - I_d \tag{4-11}$$

$$\frac{\partial f_d}{\partial I_d} = -V_d \tag{4-12}$$

The CPLs create a non-linear vector function in PF equations that expresses I_d as a function of their voltages V_d and controlled power demand P_d as follows.

$$I_d = diag\left(V_d\right)^{-1} \times P_d \tag{4-13}$$

The objective is to solve for state variables V_d, where P_d and V_v are known values. The ensuing non-linear function can be written as.

$$F\left(V_d\right) = diag\left(V_d\right)^{-1} \times P_d - \left(G_{d\upsilon} \times V_{\upsilon}\right) - \left(G_{dd} \times V_d\right) \tag{4-14}$$

4.1.2 Convergence of MANA

The convergence of NR method depends on inherent characteristics of the function given in (4-14). If $F\colon \mathbb{R}^n \to \mathbb{R}^n$ is a differentiable vector function, then the aim is to find a vector such that: $V_d \in \mathbb{R}^n\colon F(V_d) = 0$. To do so, the NR method is used, which entails assessing from a starting point $V_d^{(0)}$ using an iterative procedure as follows.

$$V_d^{(t+1)} = V_d^{(t)} - \left[dF\left(V_d^{(t)}\right)^{-1} FV_d^{(t)} \right] \tag{4-15}$$

The Kantorovich theorem can be used to explore the convergence characteristics of (4-15). The Kantorovich theorem is a mathematical statement on the convergence of Newton's method. Newton's method constructs a sequence of points that under certain conditions will converge to a solution ($F(V_d) = 0$ in this case). The Kantorovich theorem gives conditions on the initial point of this sequence. If these conditions are satisfied, then a solution exists close to the initial point and the sequence converges to that point. The details of Kantorovich theorem and its application to NR method can be found in [62]. The implementation of the theorem is given below.

Let $V_d^{(0)}$ be a point in real space $\mathbb{R}^n$ and $F: E_o \to \mathbb{R}^n$ a differentiable map with its derivative $dF(V_d)$ invertible, then:

$$\Delta V_d^{(0)} = \left[dF\left(V_d^{(0)}\right)^{-1} FV_d^{(0)} \right] \tag{4-16}$$

$$V_d^{(1)} = V_d^{(0)} - \Delta V_d^{(0)} \tag{4-17}$$

$$E_0 = \left\{ V_d : \left\| V_d - V_d^{(0)} \right\| \right\} \leq \left\| \Delta V_d^{(0)} \right\| \tag{4-18}$$

If the Lipschitz inequality is satisfied by the Jacobian, then:

$$\left\| dF\left(V_d\right) - dF\left(U_d\right) \right\| \leq \xi \left\| V_d - U_d \right\|, \forall V_d, U_d \in E \tag{4-19}$$

where ξ is the contraction constant for non-linear mapping and U_d is a unity vector.

A lower estimation of the basin of attraction for NR method can be written as follows.

$$\delta = \left\| F\left(V_d^{(0)}\right) \right\| \left[dF\left(V_d^{(0)}\right) \right]^{-1} \xi \leq 0.5 \tag{4-20}$$

If the preceding Lipschitz inequality holds, then the function $F(V_d) = 0$ will have a solution in E_0 and the convergence of the NR-MANA can be assured with initial condition $V_d^{(0)}$. In addition, even if $\delta < 0.5$ the convergence can be guaranteed with NR-MANA.

4.1.3 Application of Kantorovich theorem under practical conditions

Let's define constants to utilize conditions derived in prior section with Kantorovich's theorem which make sense for an electrical network.

$R_{thv} = \left\| G_{dd}^{-1} \right\|$: Network equivalent Thevenin resistance

$I_{sc} = \left\| G_{d\upsilon} \times V_\upsilon \right\|$: Short circuit current,

$\rho = max \left\| P_d \right\|$: Maximum load

$I_d^{(0)} = \left\| I_{sc} + G_{dd} \times U_d \right\|$: FS initialization

where, U_d: is a unity vector $U_d \in \mathbb{R}^{d\times 1}$.

If the graph is connected, which indicates that G_{dd} is invertible, and the sum of nodal powers is less than $inv(R_{thv})$, then the PF solution will be unique and can be computed with NR-MANA. In terms of network parameters, a lower estimation of the NR method's basin of attraction can be stated as follows.

$$\delta = \frac{\left(\rho \times \left(R_{thv}\right)^2\right) \times \left(1-\rho \times R_{thv}\right) \times \left(\rho - I_d^{(0)}\right)}{\left(\left(1-2\rho \times R_{thv}\right) - \left(I_d^{(0)} - R_{thv}\right)\right)^3} < \sigma \tag{4-21}$$

where σ is the boundary value for a specific network. The solution lies in $E_o = \{V_d : \|V_d - U_d\| < \sigma\}$ where value of σ can be realized with network parameters as follows.

$$\frac{\left(\rho + I_d^{(0)}\right) \times R_{thv}}{\left(1-\rho \times R_{thv}\right)} \le \sigma < 1 \tag{4-22}$$

Quadratic convergence can be guaranteed with NR-MANA if $\delta < \sigma$. The expression in (4-21) is solely dependent on the network parameters and loading conditions. The guaranteed convergence range can be calculated before executing the whole PF iterative process for any loading condition (ρ). This is a very useful insight for practical applications. If the condition in (4-21) is satisfied, then we can guarantee a minimum voltage larger than $1 - \sigma$ with σ given by (4-22). It is another useful observation as it provides the boundary for minimum voltage for a specific network. From (4-21) the maximum loading of a system can be written as below.

$$P(\rho) = \rho \times \left(R_{thv}\right)^2 \left(1-\rho \times R_{thv}\right)\left(\rho + I_d^{(0)}\right) - \sigma \times \left(1 - 2\rho - I_d^{(0)} \times R_{thv}\right)^3 \tag{4-23}$$

Moreover, if all the roots of $P(\rho)$ are real and satisfy the condition in (4-24), then the convergence with NR-MANA is guaranteed.

$$|\rho| < P(\rho) \tag{4-24}$$

4.1.4 Results and discussion

The modified IEEE 33 bus test feeder is used to validate the proposed method (DC-

MANA). The test network is shown in Chapter 3 (Figure 3-7), and test network data is given in Appendix A. NR-MANA is compared with ILM, LM, HE-PFM and classical GS methods in terms of CPU processing time and number of iterations/terms required. The convergence tolerance is set to 13 decimal places. The solution of this test network has already been validated through EMT simulation in Chapter 3. In the simulation scenarios, the loading is increased up to 3 times of the original load. The impact of loading conditions is illustrated in Figure 4-2 for the meshed configuration. For the radial configuration, both LM and ILM use one incidence matrix; hence, there is no significant performance difference.

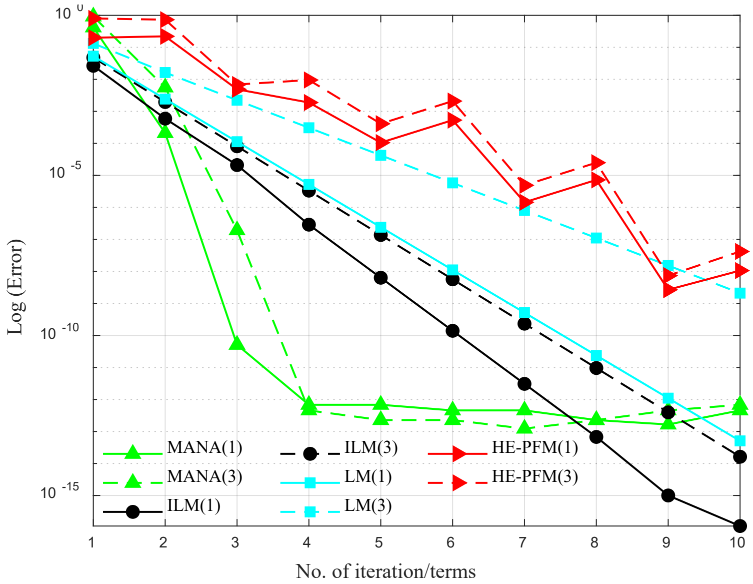

Figure 4-2. Error as a function of number of iterations/terms (1 and 3 in the brackets indicate *pu* loading).

ILM outperforms the LM in the meshed configuration and the performance difference becomes more significant at high loading conditions. Unlike LM, ILM, and HE-PFM, NR-MANA is a Jacobian based technique and offers quadratic convergence. Its convergence characteristics are not affected significantly with the network configuration and increased loading conditions if the loading is within the guaranteed convergence range. Equations (4-21) and (4-22) give an insight into the convergence property of NR-MANA method. As shown in Figure 4-3, quadratic convergence is guaranteed for loadings up to 232% of the original as $\delta<\sigma$. The theoretical guaranteed convergence range is above 250% of the original loading as $\delta<1/2$. It should be noted that the condition given in (4-23) depends on the network parameters which define the boundary of the system.

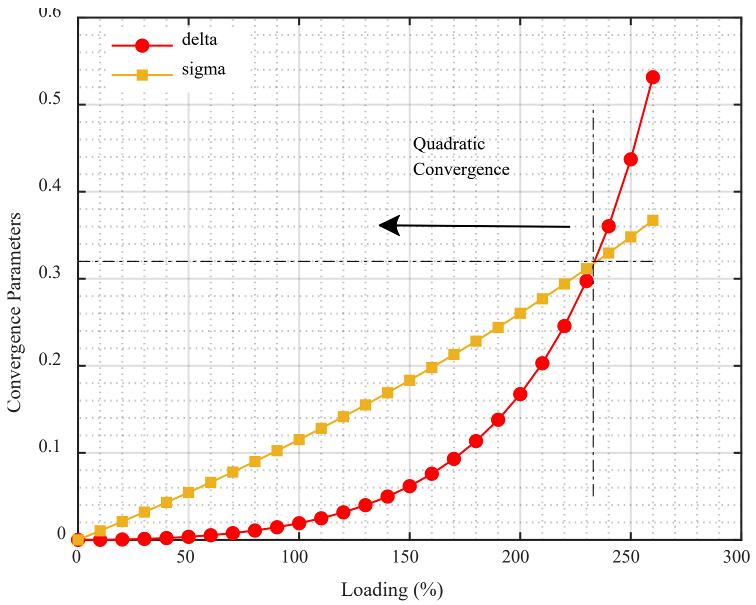

Figure 4-3. Relationship between sigma and delta in terms of network loading (Meshed Network)

If the boundary condition is relaxed the guaranteed convergence range offered by NR-MANA will increase accordingly. In addition, the guaranteed convergence range offered by NR-MANA is more than enough for practical network parameters. The convergence characteristics of the ILM algorithm can be investigated by calculating the contraction constant as demonstrated in Chapter 3. The value of contraction constant for the same test network for radial and meshed network at nominal loading and 300% loading is shown in Figure 4-4.

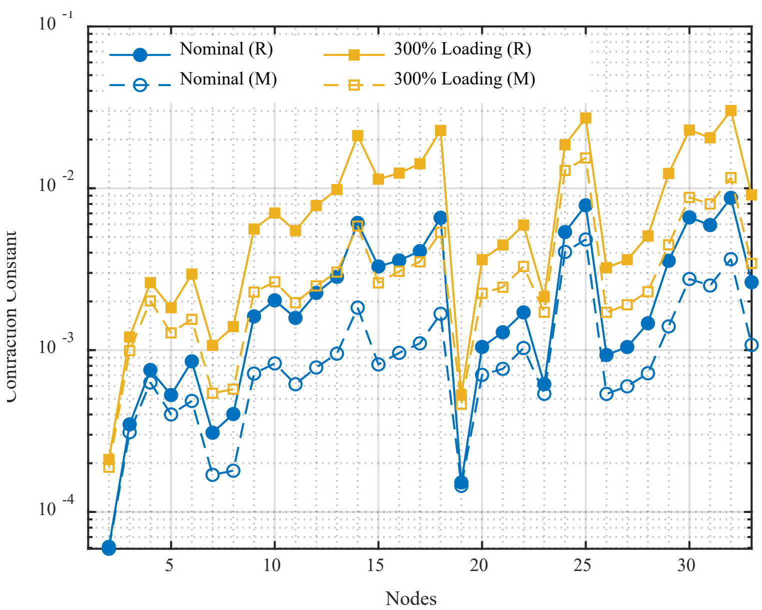

Figure 4-4. Value of contraction constant at different loading conditions (R=Radial, M=Meshed)

The ILM offers a larger theoretical guaranteed convergence range. However, it is a non-derivative method, and its convergence rate is much slower compared to NR-MANA. Although the theoretical guaranteed convergence range of NR-MANA is lower than ILM, it is more than sufficient for practical applications. The HE-PFM gives an early indication about the solution convergence or divergence, but it has computational speed disadvantage due to the computational burden while finding roots. Calculating the Pade approximation only makes sense when the roots of the denominator are also calculated. Root searching of high polynomials incurs an additional computational burden. In addition, if the number of power terms is very large, numerical errors in calculating the Pade approximation may lead to spurious poles [99].

4.1.5 Performance comparison of NR-MANA, LM, ILM, GS and HE-PFM PF solvers

A detailed performance comparison of NR-MANA with ILM, LM, HE-PFM and classical GS methods is presented in TABLE 4-1 for IEEE 33 bus test feeder and a large network which is created by cascading the IEEE 33 bus test feeders (see Figure 4-5). Five IEEE 33 bus test feeders are connected to a common substation bus bar as illustrated in Figure 4-5. Feeder-2 and Feeder-4 have radial configuration, whereas Feeder-1, Feeder-3 and Feeder-5 have meshed configuration. Bus 18 of Feeder-2 is connected to bus 18 of Feeder-3. Bus 30 of Feeder-3 is connected to bus 33 of Feeder-4. Bus 1 of each feeder is connected to Thevenin equivalent that represents the remaining part of the network. The convergence related parameters of the considered test networks are also given in TABLE 4-1.

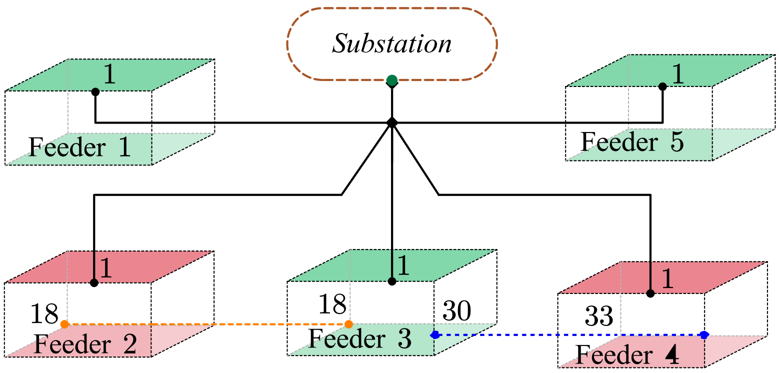

Figure 4-5. 167-bus Test Network

The value of $P(\rho)$ for the base case is 1.23 per unit (pu). It is important to note that the value of $P(\rho)$ is unique for every network and is solely determined by network configuration and line parameters. It indicates how strong or weak the network is in terms of load bearing capacity, i.e., higher value of $P(\rho)$ means a stronger network. The maximum loading capacity for any network can be determined by this factor.

TABLE 4-1. Detailed comparison of PF methods for DC network

Loading (%)	**PF Method**	**Number of Iterations/terms**	**Time (*msec*)**	**δ**	**σ**	**ρ**
100% (33 bus)	GS	712	9.68	0.019	0.115	0.42
	HE-PFM	11	4.34			
	LM	10	1.90			
	ILM	8	1.58			
	MANA	3	1.16			
300% (33 bus)	GS	827	12.46	1.204	0.448	1.26
	HE-PFM	18	6.12			
	LM	17	2.63			
	ILM	11	1.99			
	MANA	4	1.25			
100% (167 bus)	GS	1209	43.56	0.095	0.575	0.42
	HE-PFM	23	19.51			
	LM	16	9.90			
	ILM	11	7.49			
	MANA	5	3.21			
300% (167 bus)	GS	1472	57.32	4.98	2.03	1.26
	HE-PFM	32	28.16			
	LM	27	11.26			
	ILM	15	8.988			
	MANA	5	3.35			

As seen in TABLE 4-1, for 33 bus test feeder the NR-MANA converges to the PF solution in 4 iterations even for 300% of the original loading condition although it is beyond the theoretical convergence range. Other methods require more iterations with the increase in loading. Therefore, the performance differences between NR-MANA and others PF solvers become more significant with the increase in loading. At original loading, the improvements in simulation speed for 33 bus network is around 22%, 38%, 73 % and 88% compared to

ILM, LM, HE-PFM and GS based PF solvers, respectively. At 300% of original loading conditions, the improvements increase to 37%, 44%, 80% and 90%. These improvements are even more prominent for 167 bus network, the improved values at 100% loading are around 57%, 68%, 83%, and 93% compared to ILM, LM, HE-LFM and GS respectively. The improvements increase to 63%, 70%, 88% and 95% at 300% loading for 167 bus network.

4.2 Integration of DC/DC Converter Models into DC-MANA Formulation

This section reformulates DC-MANA to add DC/DC converter models into PF equations. Moreover, the proposed formulation is generalized in order to handle any arbitrary network configuration with DC/DC converters. The DC/DC converter models developed Chapter 2 are utilized. All the potential DC bus interconnections are illustrated in Chapter 3. Similar to the ILM method, sum of line flows are used instead of bus power injections in DC-MANA formulation. The line flows and associated partial derivatives of all DC cases (see Figure 3-13) can be found in Chapter 2, Section 2.4 (Case 11 to Case 17)

4.2.1 DC-MANA Reformulation to account for DC/DC Converters

In this section, the DC-MANA is reformulated to integrate DC/DC converter model in DC networks. MANA takes not only voltages but also currents of “non-constitutive elements” (NCE) as state variables. The term NCE refers to network elements with current expressions that are hard to write as a function of their terminal voltages alone. The MANA formulation can be summarized below.

$$F(x) = G_{aug} \times u + I_{cpt} - I_{gen} - W \tag{4-25}$$

where x is the vector of state variables. I_{cpt} and I_{gen} are the augmented vector of currents for constant power terminals and generator buses, respectively. W is the vector of independent voltage sources and currents. G_{aug} is an augmented conductance matrix as given below.

$$\left[G_{aug}\right] = \begin{bmatrix} G & A_1 \\ A_2 & A_3 \end{bmatrix} \tag{4-26}$$

where, G is the conductance matrix, A_1, A_2, and A_3 are the matrices that represent the voltage-current relationship of the NCE, which are not represented with their conductance models in G.

The simplified version of MANA for a DC-DN is given in Eq. 4-1 in section 4.1. In (4-25), the slack bus is modelled as a voltage source. Like classical NA formulation, the constant resistive load (CRL) is directly incorporated in G_{aug}. The presence of CPTs in the system makes PF equations non-linear and non-convex, so an iterative method is needed. The NR algorithm is used to solve the proposed MANA formulation.

TABLE 4-2 presents the type buses with associated known (✓) and unknown (✗) quantities used for realizing DC-DN PF formulation. Bus type 1 is a slack bus, bus type 2 is a load bus, bus type 3 is a voltage-controlled bus, and bus 4 is a voltage-controlled bus through a DC/DC converter.

TABLE 4-2. Type of buses in DC-DN

Bus (m)	**Type**	**V_m**	**P_m**	**D_m**
1	Slack	✓	✗	-
2	P_{dc}	✗	✓	-
3	P_{dc}	✓	✗	-
4	$P_{dc} - V_{dc}$	✓	✗	✗

The vector of state variables (x) can be written as follows.

$$x = \begin{bmatrix} V_i & \cdots & D_j & \cdots \end{bmatrix}^T, \forall i \in type\,2, \forall j \in type\ 4 \tag{4-27}$$

Active power limits for a DC voltage-controlled bus are as follows.

$$V_{dc} \rightarrow \begin{Bmatrix} P^g > P^g_{(max)} & , & P^g = P^g_{(max)} \\ P^g < P^g_{(min)} & , & P^g = P^g_{(min)} \end{Bmatrix}$$

If the active power limits of a DC voltage-controlled bus are violated, it will act as a DC load bus with the active power equals to the violated limit. When the active power limits are violated, the bus type will change, and voltage magnitude of that bus appears as a variable in the unknown vector. The related mismatch vector and Jacobian matrix is also updated accordingly.

To generalize the presented approach, so that any arbitrary network configuration can be solved with DC/DC converters, the binary variables shown in TABLE 4-3 are introduced. In the formulation, the bar for binary elements stands for binary complement.

TABLE 4-3. Binary variables and their binary values

Variable	Type	Operation	Converter	No converter
K	bus type vector	buck	1	0
T	bus type vector	boost	1	0
KT	bus type vector	buck-boost	1	0
L	line type matrix	buck/ boost/ buck-boost	1	0

All the possible interconnections of the load (l) and generator (g) in a DC network are illustrated in Figure 4-7.

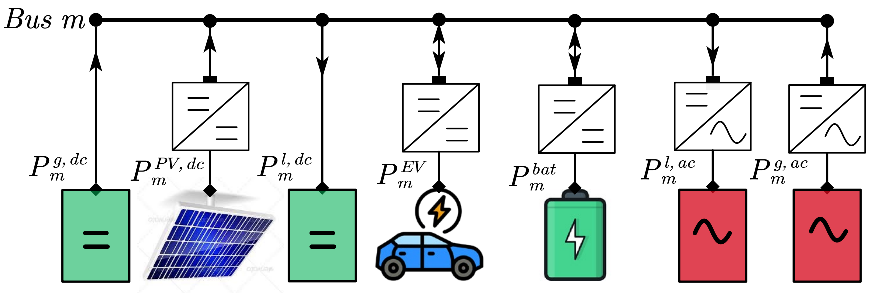

Figure 4-6. Load and generation possible connections with DC bus.

The generalized expression for the specified (sp) and calculated (cal) active power at sending bus "m" can be written as follows.

$$P_m^{sp} = \begin{bmatrix} P_m^{g,dc} + \eta_{m,PV} P_m^{PV,dc} - P_m^{l,dc} - \tau \dfrac{P_m^{EV}}{\eta_{m,EV}} + \bar{\tau}\, \eta_{m,EV} P_m^{EV} \ldots \\ -\gamma \dfrac{P_m^{bat}}{\gamma_{m,bat}} \bar{\gamma} + \eta_{m,bat} P_m^{bat} + \eta_{m,rec} P_m^{g,ac} - \dfrac{P_m^{l,ac}}{\eta_{m,inv}} \end{bmatrix} \tag{4-28}$$

$$P_m^{cal} = \sum_{\substack{n=1 \\ n \neq m}}^{N} [C_{mn}] \begin{bmatrix} \bar{K}_m \bar{T}_m \bar{L}_{mn} \bar{B}_n \bar{T}_n \left[P_{mn}^{C1}\right] + K_m \bar{T}_m L_{mn} \bar{K}_n \bar{T}_n \left[P_{mn}^{C5}\right] + \ldots \\ \bar{K}_m T_m L_{mn} \bar{K}_n \bar{T}_n \left[P_{mn}^{C6}\right] + K_m T_m L_{mn} \bar{K}_n \bar{T}_n \left[P_{mn}^{C7}\right] + \ldots \\ \bar{K}_m \bar{T}_m L_{mn} K_n \bar{T}_n \left[P_{mn}^{C2}\right] + \bar{K}_m \bar{T}_m L_{mn} \bar{K}_n T_n \left[P_{mn}^{C3}\right] + \bar{K}_m \bar{T}_m L_{mn} K_n T_n \left[P_{mn}^{C4}\right] \end{bmatrix} \tag{4-29}$$

where, τ, $\bar{\tau}$, γ, and $\bar{\gamma}$: binary coefficients for the charging and discharging operation of EVs and batteries, respectively. N is the number of buses in the network. The superscript C in line flows is illustrated in Figure 3-13 (Chapter 3).

The Jacobian in section 4.1.1 is extended to include the generalized load model defined in Chapter 2, Section 2.6. Moreover, the convergence proof given in sections 4.1.2 and 4.1.3 holds for this extended formulation as long as the conditioned defined in (4-21) and (4-24) are satisfied.

4.2.2 Results and Discussion

This section compares CPU processing times and required iterations of the extended version of ILM method (e-ILM) and the extended version of MANA for DC-DNs with DC/DC converter models. The tolerance convergence is set to 10 decimal places. The load is increased to 2.5 times of the original load. The modified IEEE 33 bus test feeder shown in Figure 3-14 in Chapter 3 is used to test the proposed method.

Figure 4-7 shows the errors at each iteration and Figure 4-8 shows the related processing times for various loading conditions. The MANA based PF solver converges to the solution faster than the e-ILM as expected. The improvements in simulation time are 56% and 64% at the 100% and 250% loading conditions, respectively.

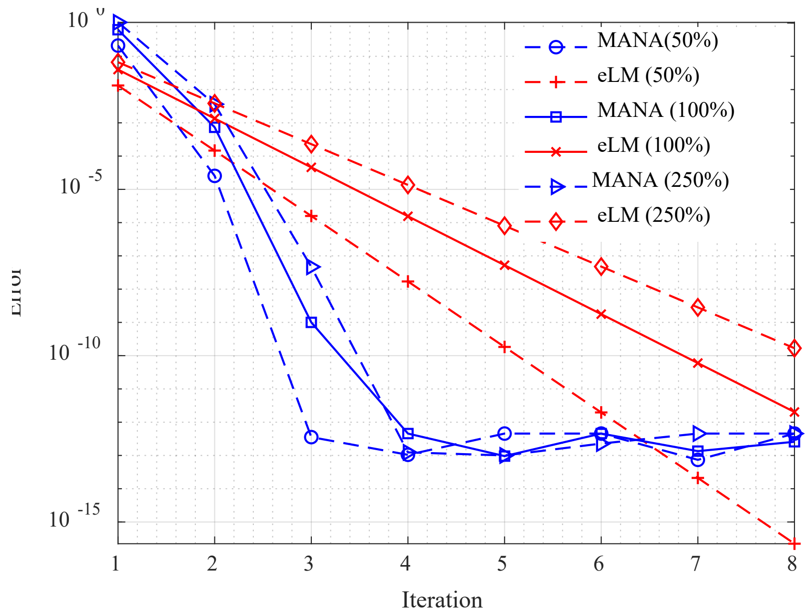

Figure 4-7. Error as a function of number of iterations

The proposed method's convergence is demonstrated using Kantorovich's theorem. The value of convergence parameters (σ and δ) are plotted and the guaranteed quadratic convergence region is indicated in Figure 4-9 at different loading conditions. The e-ILM PF solver can assure convergence if the value of contraction constant is less than unity.

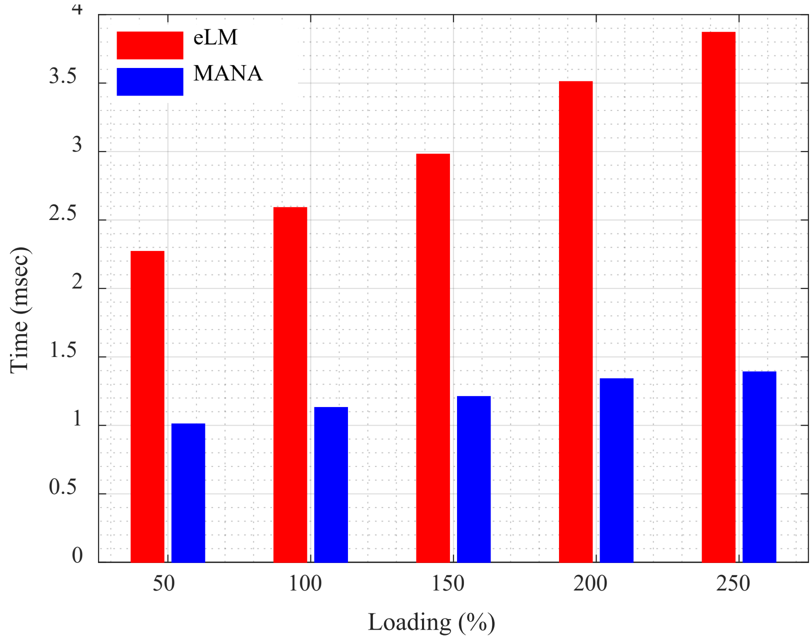

Figure 4-8. Comparison of processing time

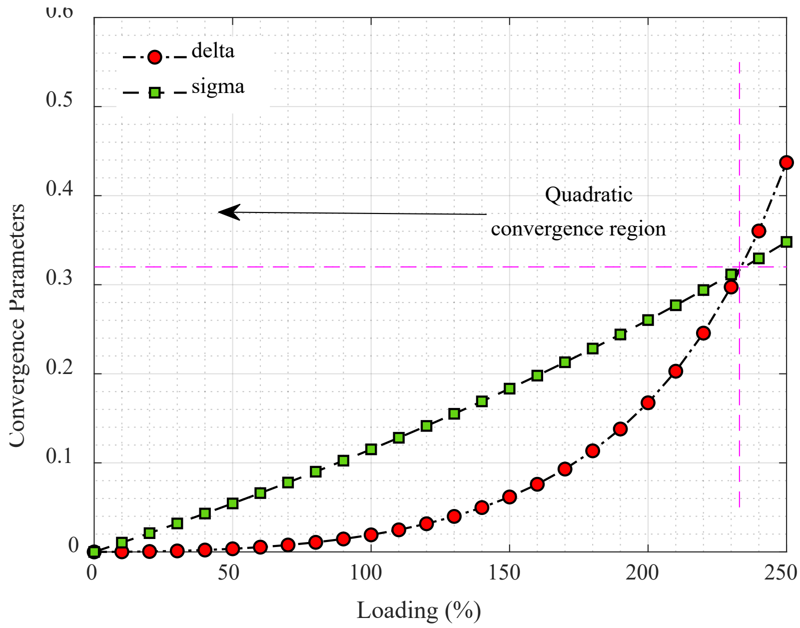

Figure 4-9. Convergence parameters of MANA for different loadings

The convergence of the e-ILM is demonstrated with BFPT by plotting the values of contraction constant at different loadings in Figure 4-10. It can be seen from the results that both PF methods provide a wide range of convergence. MANA offers quadratic convergence, whereas the convergence of the e-ILM methods is linear. Therefore, MANA outperforms e-ILM in terms of simulation speed.

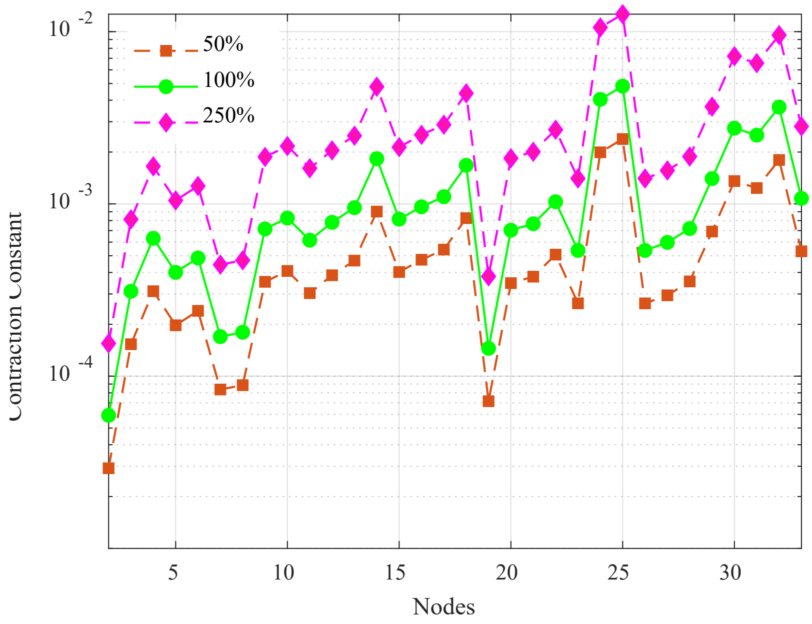

Figure 4-10. Value of contraction constant for different loadings

4.3 Chapter Summary

In this chapter, a PF solver for DC-DNs hosting CPLs is formulated. The proposed solver uses MANA formulation and NR algorithm. The uniqueness of solution and the conditions for guaranteed convergence are derived using Kantorovich's theorem. Calculating the guaranteed convergence range gives an insight to user without executing the PF routine. For the considered test networks, the calculated guaranteed convergence range is well above the practical loading conditions.

The simulations also demonstrated that the proposed method offered best convergence property and simulation speed. The improvements in simulation speeds for 33 bus networks are around 30%, 42%, 77% and 89% compared to ILM, LM, HE-PFM and GS based PF solvers, respectively. These improvements increased around 45%, 69%, 85% and 94 for 167 bus networks. This formulation is extended to accommodate DC/DC converter models into PF formulation. Results show that MANA offered best simulation speed as compared to e-ILM PF solver. The improvements in simulation time of 33 bus test feeder (meshed configuration) are 56% and 64% at 100% and 250% loading conditions, respectively.

4.4 Publications

[1] **Javid, Zahid**, Ulas Karaagac, and Ilhan Kocar. "MANA Formulation Based Load Flow Solution for DC Distribution Networks." *IEEE Transactions on Circuits and Systems II: Express Briefs* (2023).

[2] **Javid, Zahid**, Ulas Karaagac, Ilhan Kocar and Tao Xue. “DC Grid Load Flow Solution Incorporating Generic DC/DC Converter Topologies.” *Energy Reports*, 2023 (Accepted for Publication).

CHAPTER 5. Unified Power Flow Solver for Hybrid AC/DC Distribution Networks

In this chapter, the PF method based on the MANA formulation and the NR algorithm for hybrid AC/DC DNs is presented. The proposed algorithm is implemented in MATLAB and tested on three different test networks for various configurations. These test networks are the modified IEEE 33 bus test feeder (test network 1), 167 bus test network (test network 2) obtained by interconnecting five of the modified IEEE 33 bus test feeders with different configurations, and 3880 bus test network (test network 3) obtained by modifying the Turkish power system in [132]. The PF solutions of modified IEEE 33 bus test feeder are compared with EMT simulations for accuracy validation. Furthermore, the convergence characteristics of classical NA-NR and MANA-NR are compared on the test network 3 for various loading conditions and X/R ratios. This comparison together with the inspection of the Jacobian condition number give important insights regarding the superior performance of the MANA-based solutions.

5.1 AC-DC MANA Formulation

TABLE 5-1 presents the bus types with associated known (✓) and unknown (✗) quantities used for realizing hybrid AC/DC DN PF formulation. Slack, PV, and PQ buses in TABLE 5-1 are conventional AC buses. Bus types 4, 5, 6, and 7 are AC buses where a VSC is connected. The VSC is controlling V_{dc} and V_{ac} at bus type 4, P and V_{ac} at bus type 5, V_{dc} and Q at bus type 6, and P and Q at bus type 7. Bus types 8, 9 and 10 are DC buses. Bus type 8 is a DC load bus. The bus type 9 controls the DC voltage. The bus type 10 contains constant power generation and controls the DC voltage through duty cycle ratio. The MANA formulation can be summarized below.

$$F(x)=\left[Y_{Aug}\right]\left[x\right]+[I]_{(PQ)}-[I]_{(gen)}-[W] \tag{5-1}$$

where x is the vector of state variables. I_{PQ} and I_{gen} are the augmented vector of currents for PQ loads and generator buses, respectively. W is the vector of independent current and voltage sources

TABLE 5-1. Different type of buses in hybrid AC/DC network

Bus (m) Type			V_m	θ_m	P_m	Q_m	M_m	D_m
AC	1	Slack	✓	✓	×	×	-	-
	2	PQ	×	×	✓	✓	-	-
	3	PV	✓	×	✓	×	-	-
	4	V_{dc}-V_{ac}	✓	×	×	×	✓	-
	5	P-V_{ac}	✓	×	✓	✓	×	-
	6	V_{dc}-Q	×	×	×	✓	✓	-
	7	P-Q	×	×	✓	✓	✓	-
DC	8	P_{dc}	×	-	✓	-	-	-
	9	V_{dc}	✓	-	×	-	-	-
	10	P_{dc}-V_{dc}	✓	-	✓	-	-	×

The Y_{Aug} is given below.

$$\left[Y_{Aug}\right]=\begin{bmatrix}[Y] & [A_1]\\ [A_2] & [A_3]\end{bmatrix} \tag{5-2}$$

where Y is the admittance matrix of hybrid AC/DC network. A_1, A_2 and A_3 are the matrices that represent the voltage-current relationship of the network components, which are not represented with their admittance model.

The slack bus is modelled as a voltage source in (5-1). Like classical NA formulation, the constant impedance load is directly incorporated in the admittance matrix Y [66]. Due to the non-linearities of PQ loads and DG integration, an iterative method is required to solve (5-1). The NR algorithm is utilized as shown below.

$$\left[(\Delta x)\right]^{(t)}=-\left[(J)^{(t)}\right]^{-1}\left[F(x)\right]^{(t)} \tag{5-3}$$

$$[x]^{(t+1)}=[x]^{(t)}+\left[(\Delta x)\right]^{(t)} \tag{5-4}$$

where J is the Jacobian matrix and t is the iteration number.

The generic form of the vector of state variables can be written as follows.

$$x=\left[\theta_i\cdots V_j\cdots V_k\cdots M_m\cdots D_n\right]^T \rightarrow \begin{cases}\forall i\in PV, PQ, V_{dc}-V_{ac},\ldots\\ \quad P-V_{ac}, V_{dc}-Q, P-Q\\ \\ \forall j\in PQ, V_{dc}-Q, P-Q\\ \forall k\in P_{dc}\\ \forall m\in P-V_{ac}\\ \forall n\in P_{dc}-V_{dc}\end{cases} \tag{5-5}$$

5.1.1 Interconnections of buses in hybrid AC/DC grids

Like the DC-MANA, the summation of line flows and their associated derivatives are used in PF formulation. The line flow equations for all the possible interconnection cases shown in Figure 5-1 and Figure 5-2 can be found in Chapter 2.

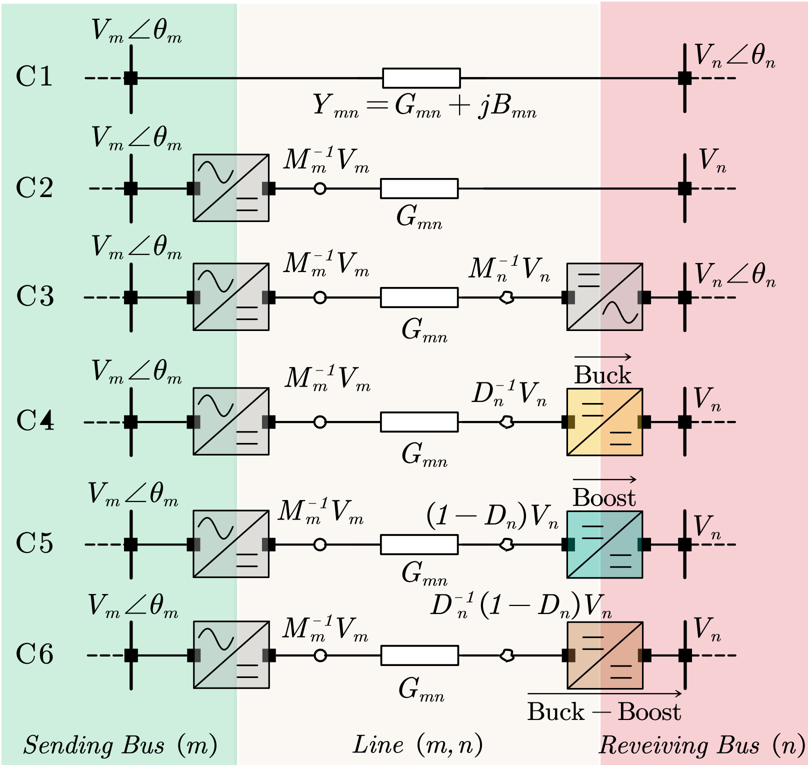

Figure 5-1. Possible configurations in hybrid AC/DC network with AC as sending bus

5.1.2 Generic PF formulation of hybrid AC/DC networks

Before presenting the generic PF formulation, which can handle any arbitrary hybrid AC/DC network configuration, it is essential to define the following parameters where subscripts *m* and *n* indicate the sending and receiving buses, respectively.

N = Total number of buses in the network, B = Bus type

C_{mn}: Binary element of connectivity matrix C of line connecting sending bus *m* and receiving bus *n*,

C_{mn} = 1: If there is a line between bus *m* and *n*,

C_{mn} = 0: If there is no connection between bus *m* and *n*,

Γ: Bus type vector (AC or DC); Γ = 0: for AC bus, Γ = 1 for DC bus

L: Line type matrix (AC or DC); L_{mn} = 0: for AC, L_{mn}= 1 for DC

K: Bus type vector (simple DC or with buck converter)

K = 0 (simple DC bus), K = 1, (DC bus with buck operation)

T: Bus type vector (simple DC or with boost converter)

$T = 0$ (simple DC bus), $T = 1$, (DC bus with boost operation)

K = 0 & T = 0 (simple DC bus)

K = 1 & T = 1 (DC bus with buck-boost operation)

E: Line type matrix (simple DC line or with DC converter)

E_{mn} = 0: for simple DC line

E_{mn} = 1 for DC line with converter operation.

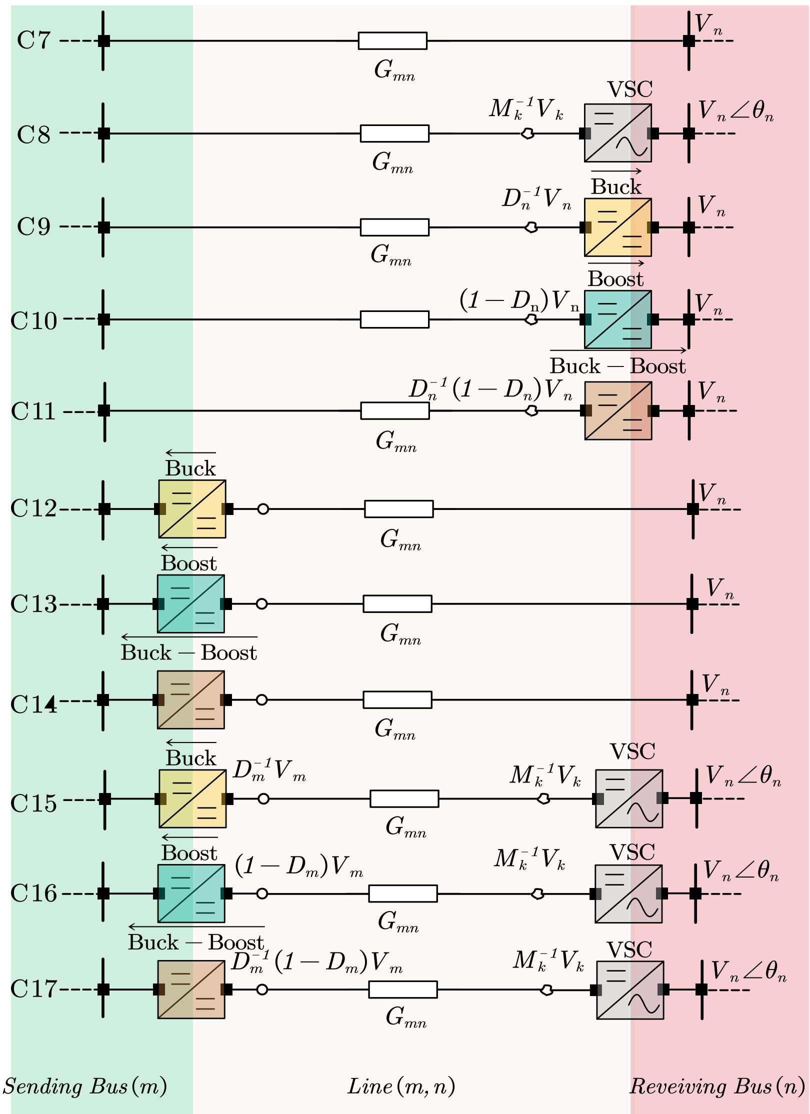

Figure 5-2. Possible configurations in hybrid AC/DC network with DC as sending bus

TABLE 5-2 shows the values of binary variables for all possible interconnections between AC and DC buses. TABLE 5-2 will help the readers to understand the formation of the Eqs. (5-6) - (5-9).

TABLE 5-2. Binay values in PF formulation of hybrid AC/DC network

C_{mn}	B_m	L_{mn}	B_n	Γ_m	L_{mn}	Γ_n	K_m	T_m	E_{mn}	K_n	T_n
1	AC	AC	AC	0	0	0	-	-	-	-	-
	AC	DC	AC	0	1	0	-	-	0	-	-
	AC	DC	DC	0	1	1	-	-	0	0	0
	AC	DC	Buck	0	1	1	-	-	1	1	0
	AC	DC	Boost	0	1	1	-	-	1	0	1
	AC	DC	Buck-Boost	0	1	1	-	-	1	1	1
	DC	DC	AC	1	1	0	0	0	0	-	-
	Buck	DC	AC	1	1	0	1	0	1	-	-
	Boost	DC	AC	1	1	0	0	1	1	-	-
	Buck-Boost	DC	AC	1	1	0	1	1	1	-	-
	DC	DC	DC	1	1	1	0	0	0	0	0
	Buck	DC	DC	1	1	1	1	0	1	0	0
	Boost	DC	DC	1	1	1	0	1	1	0	0
	Buck-Boost	DC	DC	1	1	1	1	1	1	0	0
	DC	DC	Buck	1	1	1	0	0	1	1	0
	DC	DC	Boost	1	1	1	0	0	1	0	1
	DC	DC	Buck-Boost	1	1	1	0	0	1	1	1
0	-	-	-	-	-	-	-	-	-	-	-

The general expression for specified powers at bus "m" can be written as follows.

$$\begin{aligned} P_m^{sp} = &\overline{\Gamma}_m \left(P_m^{g,ac} - P_m^{l,ac} + \eta_{m,inv} P_m^{g,dc} - \eta_{m,rec}^{-1} P_m^{l,dc} \right) + \dots \\ &\Gamma_m \left(P_m^{g,dc} - P_m^{l,dc} + \eta_{m,rec} P_m^{g,ac} - \eta_{m,inv}^{-1} P_m^{l,ac} \right), \quad \forall m \in N \end{aligned} \tag{5-6}$$

$$Q_m^{sp} = \overline{\Gamma}_m \left(Q_m^{g,ac} - Q_m^{l,ac} + Q_{m,conv}^{g,dc} - Q_{m,conv}^{l,dc} \right) + \Gamma_m \times 0, \ \forall m \in N \tag{5-7}$$

where the superscripts "*sp*" "*g*" and "*l*" indicate the specified, generation and load, respectively. The subscripts "*conv*", "*rec*" and "*inv*" indicate converter, rectifier, and inverter, respectively.

The active and reactive powers can be calculated using (5-8) and (5-9) at each iteration. For superscripts in the line flows C1 to C17, the reader should refer to Figure 5-1 and Figure 5-2. Three types of load models are considered in the formulation, viz: CPL, CCL, CIL. The constraint equation for these load models will remain the same.

$$
P_m^{cal} = \sum_{\substack{n=1 \\ n \neq m}}^{N} \left[C_{mn} \right] \begin{bmatrix} \bar{\Gamma}_m \bar{L}_{mn} \bar{\Gamma}_n \left[P_{mn}^{C1} \right] + \bar{\Gamma}_m L_{mn} \bar{\Gamma}_n \left[P_{mn}^{C3} \right] + \bar{\Gamma}_m L_{mn} \Gamma_n \begin{bmatrix} \bar{K}_m \bar{E}_{mn} \bar{T}_n \left[P_{mn}^{C2} \right] + \\ K_m E_{mn} \bar{T}_n \left[P_{mn}^{C4} \right] + \\ \bar{K}_m E_{mn} T_n \left[P_{mn}^{C5} \right] + \\ K_m E_{mn} T_n \left[P_{mn}^{C6} \right] \end{bmatrix} + \ldots \\ \Gamma_m L_{mn} \bar{\Gamma}_n \begin{bmatrix} \bar{K}_m \bar{E}_{mn} \bar{T}_n \left[P_{mn}^{C8} \right] + \\ K_m E_{mn} \bar{T}_n \left[P_{mn}^{C15} \right] + \\ \bar{K}_m E_{mn} T_n \left[P_{mn}^{C16} \right] + \\ K_m E_{mn} T_n \left[P_{mn}^{C17} \right] \end{bmatrix} + \Gamma_m L_{mn} \Gamma_n \begin{bmatrix} \bar{K}_m \bar{T}_m \bar{E}_{mn} \bar{K}_n \overline{T}_n \left[P_{mn}^{C7} \right] + \ldots \\ K_m \bar{T}_m E_{mn} \bar{K}_n \overline{T}_n \left[P_{mn}^{C12} \right] + \ldots \\ \bar{K}_m T_m E_{mn} \bar{K}_n \overline{T}_n \left[P_{mn}^{C13} \right] + \ldots \\ K_m T_m E_{mn} \bar{K}_n \overline{T}_n \left[P_{mn}^{C14} \right] + \ldots \\ \bar{K}_m \bar{T}_m E_{mn} K_n \overline{T}_n \left[P_{mn}^{C9} \right] + \ldots \\ \bar{K}_m \bar{T}_m E_{mn} \bar{K}_n T_n \left[P_{mn}^{C10} \right] + \ldots \\ \bar{K}_m \bar{T}_m E_{mn} K_m T_n \left[P_{mn}^{C11} \right] \end{bmatrix} \end{bmatrix}
$$

(5-8)

$$
Q_m^{cal} = \sum_{\substack{n=1 \\ n \neq m}}^{N} \left[C_{mn} \right] \begin{bmatrix} \bar{\Gamma}_m \bar{L}_{mn} \bar{\Gamma}_n \left[Q_{mn}^{C1} \right] + \bar{\Gamma}_m L_{mn} \bar{\Gamma}_n \left(\left[P_{mn}^{C3} \right] \tan \varphi_c \right) + \ldots \\ \bar{\Gamma}_m L_{mn} \Gamma_n \begin{bmatrix} \bar{K}_n \bar{E}_{mn} \bar{T}_n \left[P_{mn}^{C2} \right] + \ldots \\ K_n E_{mn} \bar{T}_n \left[P_{mn}^{C4} \right] + \ldots \\ \bar{K}_n E_{mn} T_n \left[P_{mn}^{C5} \right] + \ldots \\ K_n E_{mn} T_n \left[P_{mn}^{C6} \right] \end{bmatrix} \times \left(\tan \varphi_c \right) \end{bmatrix} \tag{5-9}
$$

The active and reactive load constraint equations are given below.

$$
f_L(L_p) = P_m^{(t)} - real\left(I_L^* V_L \right)^{(t)} \tag{5-10}
$$

$$
f_L(L_q) = Q_m^{(t)} - imag\left(I_L^* V_L \right)^{(t)} \tag{5-11}
$$

In the equations above, L_p and L_q are the indices for P and Q loads, I_L and V_L are the load current and voltage. $P_m^{(t)}$, and $Q_m^{(t)}$, are the real and reactive power of m^{th} load at t^{th} iteration as given below.

$$
P_m^{(t)} = P^{sp} \left(\left| V_L^{(t)} \right| / V^{sp} \right)^{\lambda_p} \tag{5-12}
$$

$$Q_m^{(t)} = Q^{sp}\left(\left|V_L^{(t)}\right| / V^{sp}\right)^{\lambda_q} \tag{5-13}$$

where λ_p and λ_q define the load characteristics (see Chapter 2, Section 2.6).

In MANA formulation, the CPL and CCL currents are also independent variables. The generic formulation for the contribution of the loads in the Jacobian can be written as follows.

$$\frac{\partial f_L(L_p)}{\partial V_{L,real}} = \frac{\lambda_p \times P_{rated} \times V_{L,real} \times \left(V_{L,img}^2 + V_{L,real}^2\right)^{\frac{\lambda_p}{2}-1}}{\left(V_{rated}\right)^{\lambda_p}} - I_{L,real} \tag{5-14}$$

$$\frac{\partial f_L(L_p)}{\partial V_{L,img}} = \frac{\lambda_p \times P_{rated} \times V_{L,img} \times \left(V_{L,img}^2 + V_{L,real}^2\right)^{\frac{\lambda_p}{2}-1}}{\left(V_{rated}\right)^{\lambda_p}} - I_{L,img} \tag{5-15}$$

$$\frac{\partial f_L(L_p)}{\partial I_{L,real}} = -V_{L,real} \tag{5-16}$$

$$\frac{\partial f_L(L_p)}{\partial I_{L,imag}} = -V_{L,imag} \tag{5-17}$$

$$\frac{\partial f_L(L_q)}{\partial V_{L,real}} = \frac{\lambda_q \times Q_{rated} \times V_{L,real} \times \left(V_{L,img}^2 + V_{L,real}^2\right)^{\frac{\lambda_q}{2}-1}}{\left(V_{rated}\right)^{\lambda_q}} + I_{L,img} \tag{5-18}$$

$$\frac{\partial f_L(L_q)}{\partial V_{L,img}} = \frac{\lambda_q \times Q_{rated} \times V_{L,img} \times \left(V_{L,img}^2 + V_{L,real}^2\right)^{\frac{\lambda_q}{2}-1}}{\left(V_{rated}\right)^{\lambda_q}} - I_{L,real} \tag{5-19}$$

$$\frac{\partial f_L(L_q)}{\partial I_{L,real}} = -V_{L,img} \tag{5-20}$$

$$\frac{\partial f_L(L_q)}{\partial I_{L,img}} = V_{L,real} \tag{5-21}$$

The above formulation except the reactive power related terms, will remain same for the DC buses. Finally, the mismatch vector can be written as follows.

$$F(x) = \begin{cases} P_m^{sp} - P_m^{cal} & , \quad \forall m \in N \\ Q_m^{sp} - Q_m^{cal} & , \quad \forall m \in N \end{cases} \tag{5-22}$$

It should be noted that the reactive power is not defined in DC network. Hence, reactive power related terms do not exist for DC buses. The convergence criteria consider maximum deviation in bus voltage magnitudes at each iteration as given below.

$$|V^{(t)} - V^{(t-1)}| < tolerance \tag{5-23}$$

5.1.3 Simulation results and discussion

The modified IEEE 33 bus test feeder shown in Figure 5-3 is simulated for both radial and meshed configurations. The accuracy of the PF solutions is validated through EMT simulations. The VSCs are represented with their average value models (AVMs)[133] in EMT simulations.

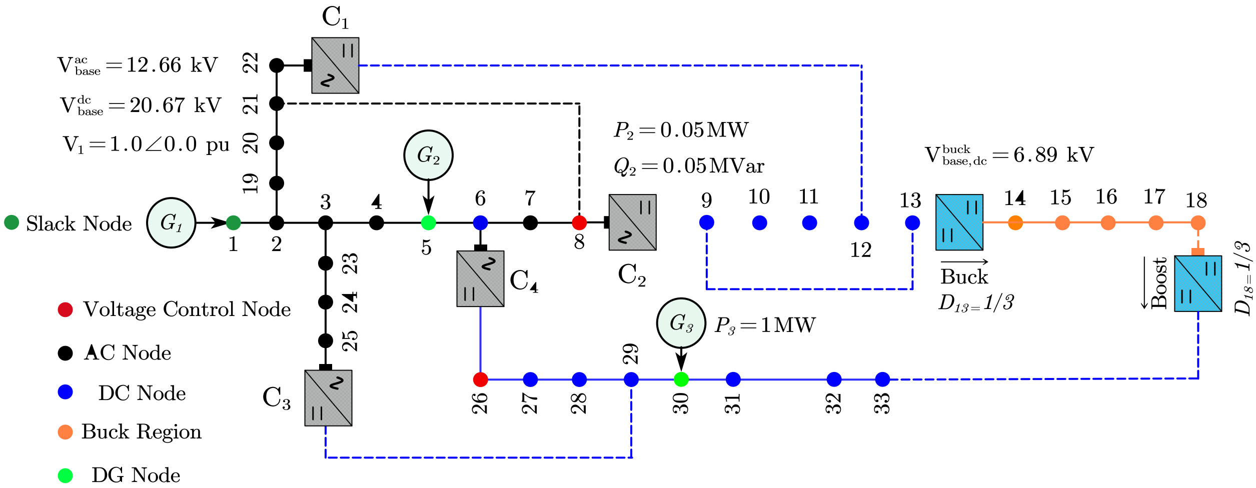

Figure 5-3. Modified IEEE 33 bus test feeder (Test network 1)

The RL representation of the loads is manually adjusted in EMT to achieve PF constraints. The constant powers for load and generation are explored in EMT as shown in Figure 5-4. The sign of constant power is negative for the load and positive for the generation.

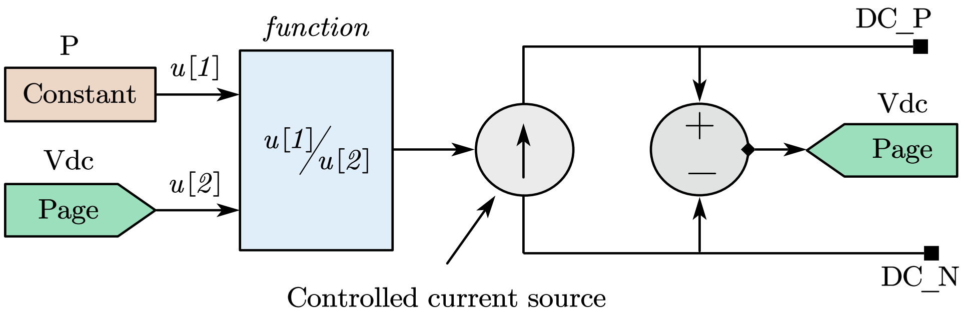

Figure 5-4. Constant power source EMT model

The test network 1 consists of AC/DC and DC/DC converters as well as DGs. The AC base voltage is 12.66 kV, and DC base voltage is 20.67 kV. The VSCs control operations are as follows:

C_1: is operating under V_{dc}-Q control,

C_2: is operating under P-V_{ac} control,

C_3: is operating under P-Q control,

C_4: is operating under V_{dc}-V_{ac} control.

The solid lines form the radial configuration (Configuration-1), and the meshed configuration (Configuration-2) is obtained by adding the dashed lines. The average X/R ratio of this network is 0.63. The simulation results presented in Figure 5-5 and TABLE 5-3 confirm the accuracy of the PF solution.

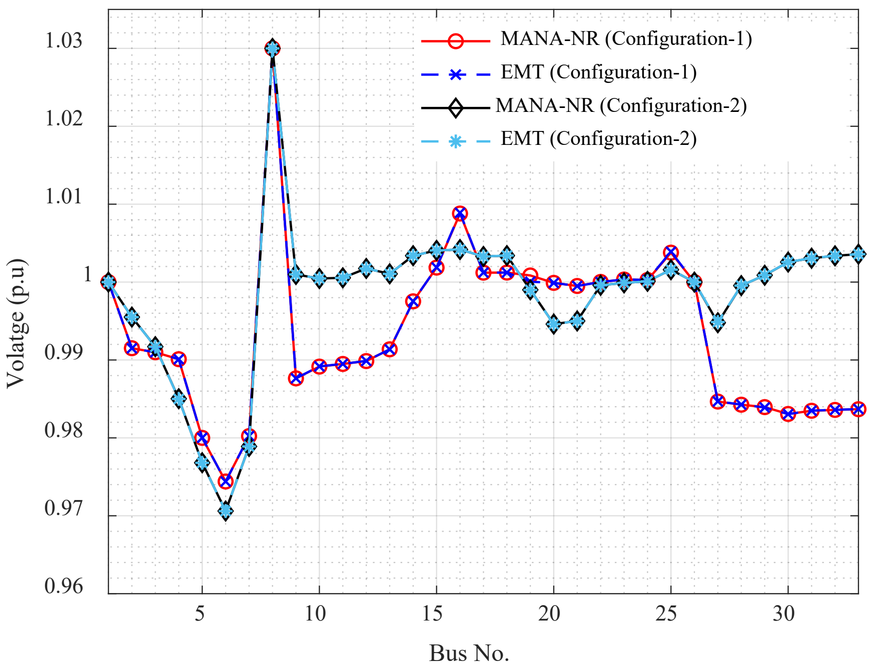

Figure 5-5. Voltage profile of different configurations

The maximum error in bus voltages is less than 0.001%. The PF solution converges from the FS in five iterations with 10^{-10} tolerance, and the total simulation time is less than 3 *ms* for both configurations.

TABLE 5-3. Line flows of test network 1 (Configuration 2)

From Bus	To Bus	MANA-NR P(kW)	MANA-NR Q(kvar)	EMT P(kW)	EMT Q(kvar)
1	2	2029.13	1049.11	2029.13	1049.10
2	3	1418.12	674.25	1418.12	674.25
3	4	344.72	159.07	344.72	159.06
4	5	223.70	78.55	223.70	78.54
5	6	329.95	81.67	329.95	81.66
6	7	-268.10	-60.08	-268.09	-60.06
7	8	-67.81	-40.86	-67.81	-40.86
8	9^{dc}	192.92	0.00	192.91	0.00
9^{dc}	10^{dc}	-36.76	0.00	-35.96	0.00
10^{dc}	11^{dc}	-96.76	0.00	-96.79	0.00
11^{dc}	12^{dc}	-141.97	0.00	-140.99	0.00
12^{dc}	13^{dc}	108.01	0.00	108.00	0.00
13^{dc}	14^{dc}	-218.48	0.00	-218.49	0.00
14^{dc}	15^{dc}	-99.79	0.00	-99.78	0.00
15^{dc}	16^{dc}	37.44	0.00	37.45	0.00
16^{dc}	17^{dc}	-45.96	0.00	-45.96	0.00
17^{dc}	18^{dc}	-80.99	0.00	-80.98	0.00
2	19	-502.0	-310.19	-502.0	-310.19
19	20	410.94	269.17	410.92	269.16
20	21	-314.10	-222.95	-314.03	-222.95
21	22	90.13	40.20	90.13	40.18
3	23	-960.44	-472.98	-960.44	-472.96
23	24	80.39	56.09	80.39	56.08
24	25	-424.11	-203.21	-424.10	-203.21
6^{dc}	26^{dc}	-796.23	0.00	-796.23	0.00
26^{dc}	27^{dc}	742.01	0.00	742.01	0.00
27^{dc}	28^{dc}	-680.11	0.00	-680.11	0.00
28^{dc}	29^{dc}	-625.11	0.00	-625.11	0.00
29^{dc}	30^{dc}	-68.81	0.00	-68.81	0.00
30^{dc}	31^{dc}	-58.98	0.00	-58.98	0.00
31^{dc}	32^{dc}	-44.67	0.00	-44.67	0.00
32^{dc}	33^{dc}	-23.56	0.00	-23.57	0.00
8	21	332.39	241.01	332.39	241.01
9^{dc}	13^{dc}	65.66	0.00	65.66	0.00
12^{dc}	22	98.39	0.00	98.40	0.00
18^{dc}	33^{dc}	105.56	0.00	105.58	0.00
25	29^{dc}	100.03	0.00	100.04	0.00

5.1.4 Performance comparison with classical NA-NR method

One reason to implement NR with MANA is to improve its convergence characteristics. The convergence of the NR method depends on how it is implemented as NR method have divergence issues especially for ill-conditioned Jacobian matrix. To compare the performance of MANA with classical NA formulation, two large test networks are simulated.

Test Network 2: The formation of test network 2 is as follows: a 167-bus test network (test network 2) is formed by connecting five modified 33 bus test feeders to a common substation busbar as illustrated in Figure 5-6. Feeder-2 and Feeder-4 have radial configuration, whereas Feeder-1, Feeder-3, and Feeder-5 have meshed configuration. Bus 18 of Feeder-2 is connected to bus 18 of Feeder-3. Bus 30 of Feeder-3 is connected to bus 33 of Feeder-4. Bus 1 of each feeder is connected to the Thevenin equivalent, representing the remaining part of the AC network.

Test Network 3: The test network 3 shown in Figure 5-7 is a part of Turkish power system [132]. Each load in test network 3 is replaced by the required number of test network 2 (the hybrid AC/DC DN in Figure 5-6) considering the busbar loadings and step-down transformers. The data of test network 3 is given in Appendix B.

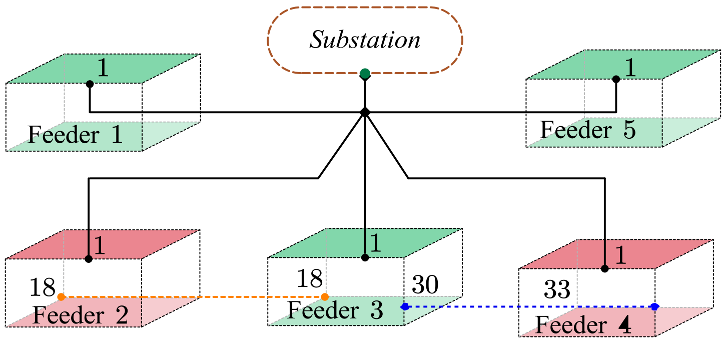

Figure 5-6. Test network 2 (167-bus)

The main difference between MANA-NR and classical NA-NR is Jacobian matrix formation. In classical NA-NR, the Jacobian matrix only contains the partial derivatives of state variables, and current is not considered as a state variable. However, the Jacobian matrix has a unique modular structure containing the explicit device models in MANA-NR. As initial conditions have a significant impact on the convergence characteristics of the NR algorithm, the Tuned Start (T.S.) method in [91] is also implemented to test the solver.

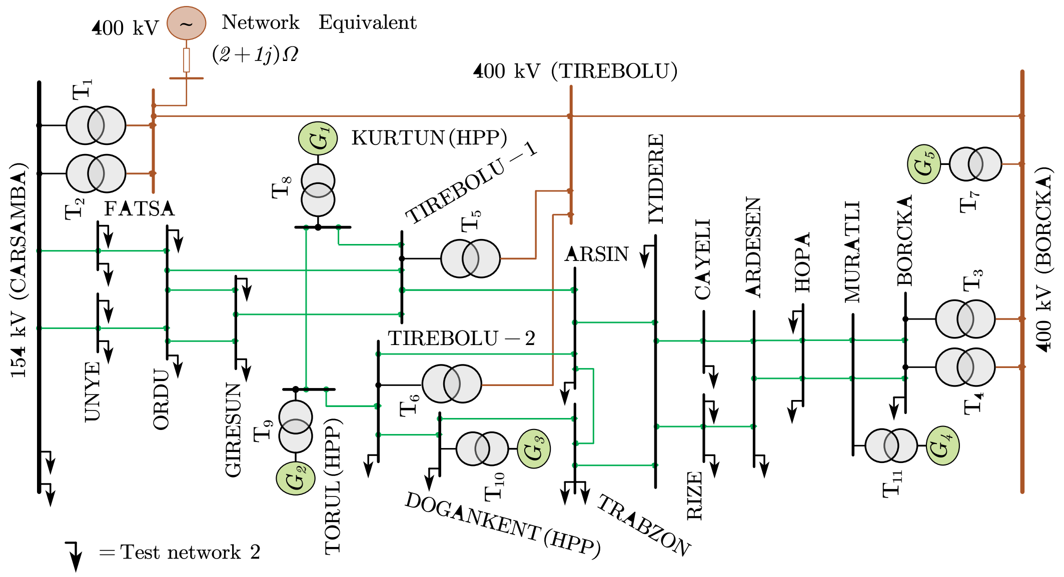

Figure 5-7. Test network 3 (3880-bus) [132]

The estimates for T.S are achieved by performing the well-known DC PF. The values obtained after the first iteration in DC PF solution then used for the T.S. The test network 2 is simulated for different loading conditions and the results are presented in TABLE 5-4. MANA formulation improves the convergence characteristics of the NR algorithm. Even with T.S, the classical NA-NR method's convergence characteristics are well below the MANA-NR with FS. The non-zero (nz) pattern of test network 3 (3880-bus network) is shown in Figure 5-8.

TABLE 5-4. Comparison of convergence results of test network 2 with FS and T.S (Nominal X/R)

Loading Factor (%)	**MANA-NR (FS)**	**Classical NR (FS)**	**MANA-NR (TS)**	**Classical NR (TS)**
0.4	8 iterations	8 iterations	7 iterations	7 iterations
0.7	8 iterations	8 iterations	7 iterations	7 iterations
1	8 iterations	8 iterations	7 iterations	7 iterations
1.3	8 iterations	diverged	7 iterations	7 iterations
1.6	8 iterations	diverged	7 iterations	7 iterations
1.9	8 iterations	diverged	7 iterations	7 iterations
2.2	8 iterations	diverged	7 iterations	diverged
2.5	8 iterations	diverged	7 iterations	diverged
2.8	8 iterations	diverged	7 iterations	diverged
3.0	8 iterations	diverged	7 iterations	diverged
3.3	diverged	diverged	7 iterations	diverged
3.5	diverged	diverged	7 iterations	diverged

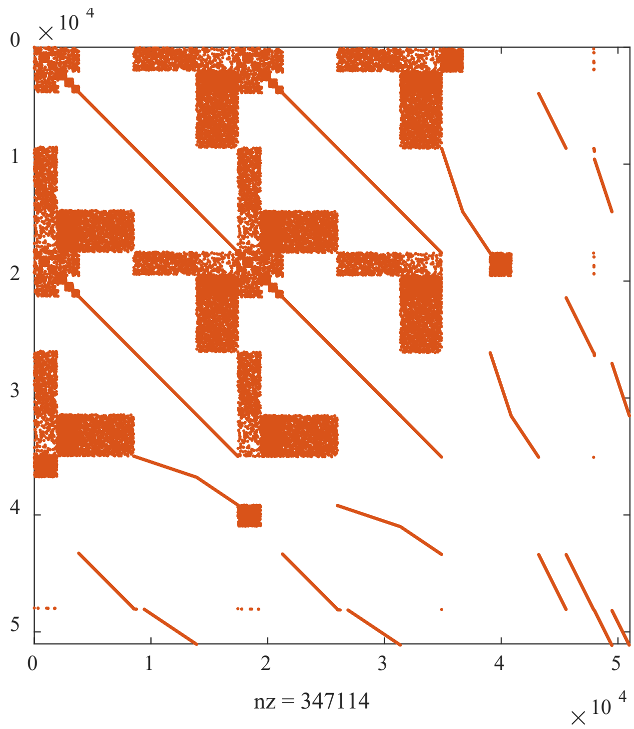

Figure 5-8. Non-zero pattern of Jacobian matrix (Test network 3)

The X/R ratio of test network varies from 0.5 to 2 with 0.1 increment in each simulation to test the robustness of the proposed PF solver. Test network 3 is simulated to confirm the applicability of the proposed PF solver for larger networks. The loading is increased from 40% to 350%. The TABLE 5-5 and TABLE 5-6 show the results at X/R ratios of 2 and 0.5 respectively.

TABLE 5-5. Comparison of convergence results of test network 3 with FS and TS (X/R = 2)

Loading Factor (%)	MANA-NR (FS)	Classical NR (FS)	MANA-NR (TS)	Classical NR (TS)
0.4	11 iterations	12 iterations	9 iterations	12 iterations
0.7	11 iterations	13 iterations	9 iterations	12 iterations
1	11 iterations	13 iterations	9 iterations	12 iterations
1.3	11 iterations	diverged	9 iterations	12 iterations
1.6	11 iterations	diverged	9 iterations	13 iterations
1.9	11 iterations	diverged	9 iterations	diverged
2.2	11 iterations	diverged	9 iterations	diverged
2.5	11 iterations	diverged	9 iterations	diverged
2.8	11 iterations	diverged	9 iterations	diverged
3.0	12 iterations	diverged	9 iterations	diverged
3.3	diverged	diverged	10 iterations	diverged
3.5	diverged	diverged	10 iterations	diverged

The TABLE 5-5 and TABLE 5-6 also represent the best and worst observed convergence characteristics as expected. The performance of MANA-NR remained unchanged for both X/R ratios; however, the convergence range of NA-NR is affected.

TABLE 5-6. Comparison of convergence results of test network 3 with FS and T.S (X/R = 1/2)

Loading Factor (%)	**MANA-NR (FS)**	**Classical NR (FS)**	**MANA-NR (TS)**	**Classical NR (TS)**
0.4	11 iterations	13 iterations	9 iterations	13 iterations
0.7	11 iterations	14 iterations	9 iterations	13 iterations
1	11 iterations	14 iterations	9 iterations	13 iterations
1.3	11 iterations	diverged	9 iterations	14 iterations
1.6	11 iterations	diverged	9 iterations	diverged
1.9	11 iterations	diverged	9 iterations	diverged
2.2	11 iterations	diverged	9 iterations	diverged
2.5	11 iterations	diverged	9 iterations	diverged
2.8	11 iterations	diverged	9 iterations	diverged
3.0	12 iterations	diverged	9 iterations	diverged
3.3	diverged	diverged	10 iterations	diverged
3.5	diverged	diverged	10 iterations	diverged

5.1.5 Comparison of Jacobian condition number of MANA-NR versus NA-NR

The reason for this improved convergence with MANA-NR is the unique structure of the Jacobian matrix in the MANA. The MANA formulation renders the Jacobian well-conditioned, even for a stressed or ill-conditioned network. For a mathematical explanation, let's consider the general expression below.

$$A x = b \tag{5-24}$$

If matrix A is square, then x will have a unique solution if A is full rank. However, if A is singular $\det(A) = 0$ and b is beyond the range of A, then there is no solution [134]. In application, the condition number estimates how near A to become singular. Theoretically, the condition number for a singular matrix is infinite. The higher condition number indicates that the matrix is relatively ill-conditioned. The Jacobian matrix condition number can be expressed as [135].

$$cond(J) = \|J\| \times \|J^{-1}\| \tag{5-25}$$

where, $\|.\|$ is a matrix norm.

The formulation becomes more robust when the Jacobian matrix condition number is smaller. The Jacobian matrix condition number for test network 2 and test network 3 of the classical NA-NR method is more than 1500 and 1800 times larger than the one of MANA-NR method at all loading conditions (where both methods converged), respectively. This explains the superiority of MANA-NR convergence characteristics over classical NA-NR. On the other hand, classical NA-NR completes each iteration in a shorter time. MANA-NR formulation usage increases the simulation time as MANA-NR utilizes more variables than classical NA-NR. However, that increase is marginal as shown TABLE 5-7. The increase in simulation time is around 15% in test network 2 and 10% in test network 3.

TABLE 5-7. Average CPU time of 100 simulations

Solver	Test network 2	Test network 3
Classical NR (FS)	6.34 msec	38.53 msec
MANA-NR (FS)	7.49 msec	43.08 msec

The derivation and proof of MANA-NR convergence characteristics with Kantorovich theorem can be found in Chapter 4 (Section 4.1.2 and Section 4.1.3) [102]. It is worth noting that MANA also uses NR iterative algorithm. The size of Jacobian matrix is considerably larger in MANA-NR compared to the classical NA-NR. On the other hand, some of the variables (such as transformer, slack bus, and closed switch currents, etc.) are directly computed in MANA-NR but require additional post-processing in classical NA-NR. Hence, the difference in total simulation time is not very significant especially when an effective sparse solver is utilized.

5.2 SST-MANA Formulation

The SST PF model developed in Chapter 2; Section 2.5 is integrated into MANA formulation of hybrid AC/DC networks in this section.

The general expression for specified powers at bus "*m*" can be written as follows.

$$\begin{aligned} P_m^{sp} = \overline{\Gamma}_m \left(P_m^{g,ac} - P_m^{l,ac} + \eta_{m,SST} P_m^{g,dc} - \eta_{m,SST}^{-1} P_m^{l,dc} \right) + \ldots \\ \Gamma_m \left(P_m^{g,dc} - P_m^{l,dc} + \eta_{m,SST} P_m^{g,ac} - \eta_{m,SST}^{-1} P_m^{l,ac} \right), \quad \forall m \in N \end{aligned} \tag{5-26}$$

$$Q_m^{sp} = \overline{\Gamma}_m \left(Q_m^{g,ac} - Q_m^{l,ac} + Q_{m,SST}^{g,dc} - Q_{i,SST}^{l,dc} \right) + \Gamma_m \times 0, \quad \forall m \in N \tag{5-27}$$

The definition of binary variables used in the above equations can be found in Chapter

5 (Section 5.1.1). The active and reactive load constraint equations, and the load model is given in (5-10 – 5-13). The generalized expression to calculate the active and reactive powers at sending bus "*m*" can be written as follows.

$$P_m^{cal} = \sum_{\substack{n=1 \\ n \neq m}}^{N} [C_{mn}] \begin{bmatrix} \overline{\Gamma}_m \overline{L}_{mn} \overline{W}_n [P_{mn}] + \overline{\Gamma}_m L_{mn} \overline{\Gamma}_n [P_{mn}] + \dots \\ \overline{\Gamma}_m L_{mn} \Gamma_n [P_{mn}] + \Gamma_m L_{mn} \overline{\Gamma}_n [P_{mn}] + \Gamma_m L_{mn} \Gamma_n [P_{mn}] \end{bmatrix} \tag{5-28}$$

$$Q_m^{cal} = \sum_{\substack{n=1 \\ n \neq m}}^{N} [C_{mn}] \left[\overline{\Gamma}_m \overline{L}_{mn} \overline{\Gamma}_n [Q_{mn}] + \overline{\Gamma}_m L_{mn} \overline{\Gamma}_n [P_{mn}] (\tan \varphi_{SST}) + \overline{\Gamma}_m L_{mn} \Gamma_n [P_{mn}] (\tan \varphi_{SST}) \right] \tag{5-29}$$

where ϕ_{SST} is SST power factor angle.

In MANA formulation, the currents of CPL and CCL are also independent variables. The generic formulation for the contribution of the loads in the Jacobian are given in (5-14 - 5-21).

The mismatch equations for the hybrid AC/DC PF are given (5-22).

5.2.1 Simulation results and discussion

The modified IEEE 33 bus test feeder shown in Figure 5-9 is used to compare the computational efficiency of MANA formulation-based PF solver with the HE-PFM. The presented results in [118] are used for accuracy validation. This system is split into four zones and contains four SSTs with 500 kVA total capacity where the maximum rating of single SST is 150 kVA. The details of the test network and simulation data can be found in [118].

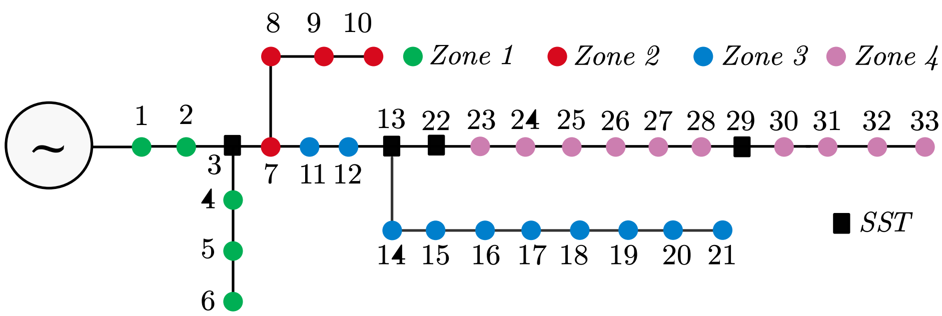

Figure 5-9. IEEE 33 bus feeder with sample SST locations

The voltage profiles and total network losses presented in Figure 5-10 and TABLE 5-8 confirm the accuracy of the proposed SST model and its formulation in both MANA based

PF solver and HE-PFM.

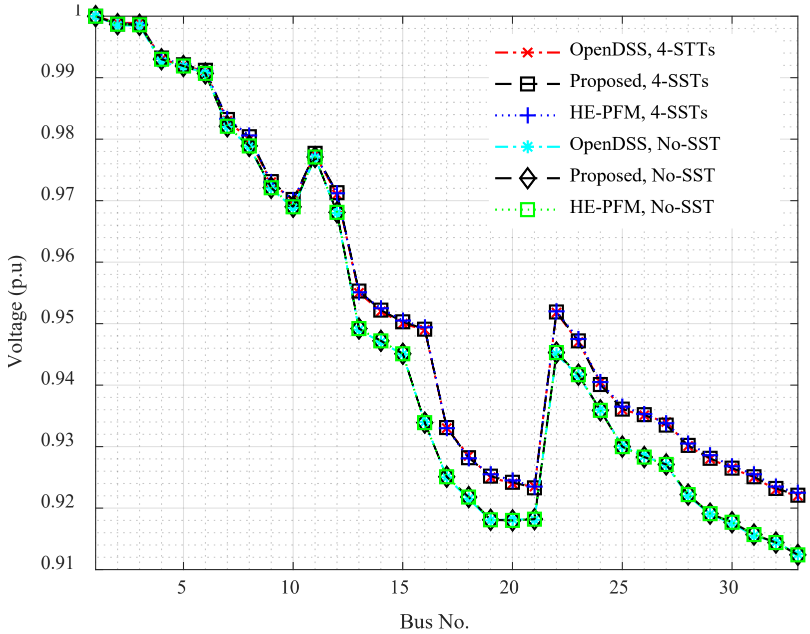

Figure 5-10. Voltage profiles

TABLE 5-8. Network losses comparison with four SSTs

Stage-1 Overrating (%)	SST Location	SST rating (kVA)	Losses (kW) Ref [117]	Losses (kW) Proposed	Losses (kW) HE-PFM
0	No-SST	-	202.67	202.67	202.67
5	3, 13, 22, 29	150, 144, 56, 150	181.59	180.99	181.05
10	3, 13, 22, 29	150, 144, 56, 150	176.89	176.54	176.41
15	3, 13, 22, 29	150, 144, 56, 150	174.49	174.36	174.28
20	3, 13, 22, 29	150, 144, 56, 150	173.23	172.96	172.98
25	3, 13, 22, 29	150, 144, 56, 150	171.12	170.01	170.00

Various multiple SST configurations shown in TABLE 5-9 has been also simulated for accuracy validation. The installed SST at bus 29 has a 500 kVA rating and each SST added to other buses has 100 kVA rating. The presented network losses in TABLE 5-9 also confirm the accuracy of the proposed SST model and its formulation in both MANA based PF solver and HE-PFM. The four SST test network with 5% overrating case (see TABLE 5-8) has been simulated for 100% and 300% loading conditions with MANA and HE-PFM to compare their computational performance. The convergence tolerance is set to five decimal places. As see in Figure 5-11 the MANA-PF method converges in 3 iterations for both loadings conditions, while HE-PFM takes 7 terms to converge. The MANA PF method also requires around 60% less time compared to HE-PFM to achieve the same level of accuracy as shown in Figure 5-12.

TABLE 5-9. Network losses comparison with multiple SSTs

No. of SSTs	Total installed rating (kVA)	SST(s) location	Losses (kW) Ref [117]	Losses (kW) Proposed	Losses (kW) HE-PFM
0	-	-	202.67	202.67	202.67
1	500	29	165.83	165.12	165.83
2	600	13, 29	162.65	162.28	162.27
3	700	13, 28, 29	160.02	159.92	160.94
4	800	7, 13, 28, 29	158.21	158.01	158.05
5	900	7, 13, 28, 29, 31	155.90	155.47	155.45
6	1000	7, 13, 28, 29, 30, 31	153.82	153.37	153.39
7	1100	7, 13, 24, 28, 29, 30, 31	152.90	152.89	152.92
8	1200	6, 7, 13, 24, 28, 29, 30, 31	151.49	151.14	151.18
9	1300	3, 6, 7, 13, 24, 28, 29, 30, 31	150.61	150.53	150.54
10	1400	1, 3, 6, 7, 13, 24, 28, 29, 30, 31	150.52	150.38	150.41
11	1500	1, 3, 6, 7, 13, 22, 24, 28, 29, 30, 31	149.28	149.20	149.19

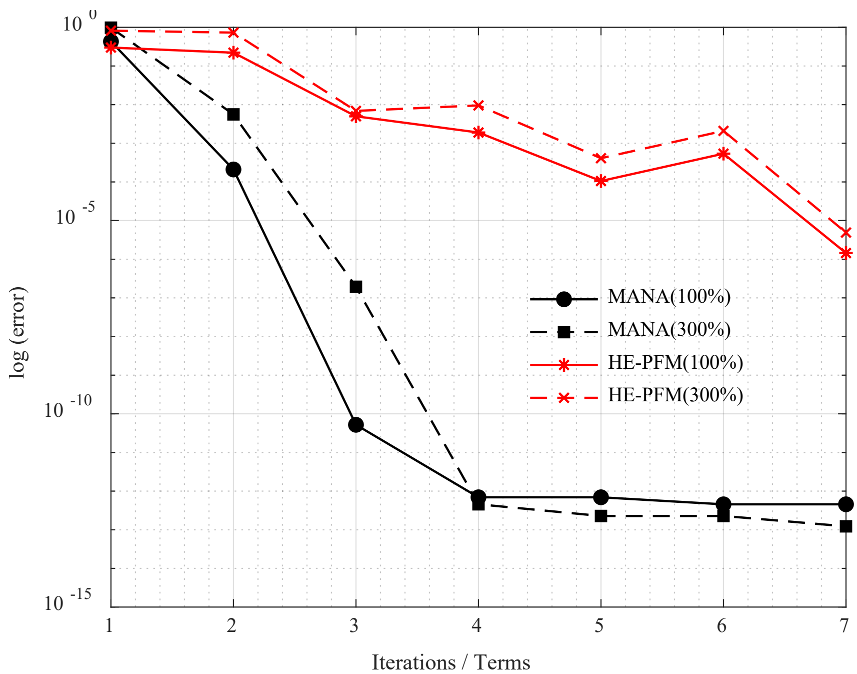

Figure 5-11. Error as function of number of iterations/terms

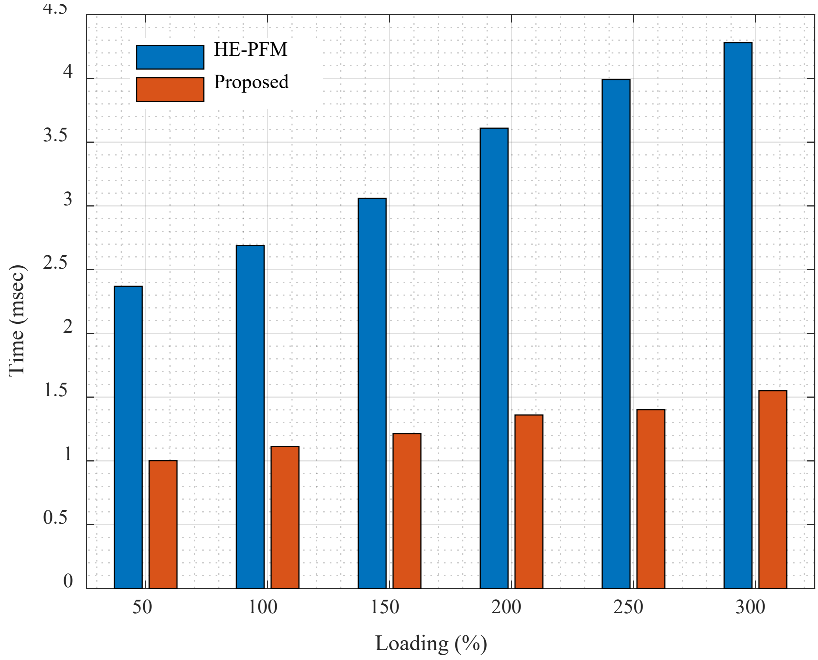

Figure 5-12. Time comparison of MANA and HE-PFM at different loadings

5.3 Chapter Summary

A unified power flow solver is formulated for hybrid AC/DC networks, incorporating explicit models of AC/DC and DC/DC converters in the power flow equations. The solver is based on the MANA formulation and utilizes the NR algorithm. Notably, the proposed solver does not require the presence of a DC slack bus, nor does it impose any network topology constraints. To validate the accuracy of the proposed solver, simulations are conducted on a modified IEEE 33 bus hybrid AC/DC test feeder, and the results are compared with EMT simulations. In addition, the convergence characteristics of the MANA formulation and the classical NA formulation are compared on a large hybrid AC/DC test network. This comparison is done under various loading conditions and X/R ratios, using FS and TS. The results show that the MANA-NR method exhibits significantly better convergence characteristics compared to the classical NA-NR method. This improvement is attributed to the well-conditioned Jacobian matrix provided by the MANA formulation, which enhances solvability and convergence robustness. Specifically, the Jacobian matrix condition number of the classical NA-NR method is found to be 1500 and 1800 times larger than that of the MANA-NR method for test network 2 and 3, respectively, across all loading conditions where both methods converge.

Furthermore, the SST PF model developed in Chapter 2 is integrated into the MANA and HE-PFM solvers for hybrid AC/DC networks with SST integration. The accuracy of THE solvers is validated on the modified IEEE 33 bus test feeder, with comparison against the solution presented in a previous study for multiple SST cases[118]. The results demonstrate that the MANA PF solver offers faster convergence compared to the HE-PFM solver, reducing simulation time by approximately 60%.

5.4 Publications

[1] **Javid Zahid**, Tao Xue, Ulas Karaagac, and Ilhan Kocar. "Unified Power Flow Solver for Hybrid AC/DC Distribution Networks." *IEEE Transactions on Power Delivery (2023*).

[2] **Javid Zahid**, Ulas Karaagac, Ilhan Kocar and William Holderbaum " Solid-State Transformer Modelling in Power Flow Calculation." *Energy Reports 2023, Vol: (Accepted for Publication*)

CHAPTER 6. Conclusions and Future Work

This thesis developed generic PF models of DC and hybrid AC/DC network components (such as AC/DC and DC/DC converters, and SST). Two types of DC PF solvers are proposed: 1-non-derivative based PF solver, 2- derivative based PF solver. The first type of solver is based on graph theory and uses LM to solve DC networks. At first a basic LM based solver is developed for DC networks, then this formulation is improved (ILM) to solve the meshed networks by using one connectivity matrix instead of two for better simulation speed. The ILM formulation is extended to include DC/DC converter models into PF formulation to obtain a generic DC PF solver. The uniqueness of the solution is demonstrated with BFPT for both LM and ILM PF solvers. The value of contraction constant provides insight into the convergence of the PF solution even before executing the whole PF algorithm. These solvers provide a wide range of convergence for DC networks.

The second type of PF solver is based on MANA formulation and uses NR algorithm. At first a PF solver for DC networks is developed, and then it is extended to add DC/DC converter models into PF equations. The uniqueness of solution and the conditions for guaranteed convergence are derived using Kantorovich's theorem. Calculating the guaranteed convergence range gives an insight to user prior to the whole PF simulation. The simulations demonstrated that, DC-MANA PF offered best convergence property and simulation speed. The improvements in simulation speeds for modified IEEE 33 bus test feeder are around 30%, 42%, 77% and 89% compared to ILM, LM, HE-PFM and GS based PF solvers, respectively. The accuracy validation is performed through EMT simulations. These improvements increased to 45%, 69%, 85% and 94 for the 167 bus test network.

Then a unified PF solver is developed with AC/DC and DC/DC converter models for hybrid AC/DC networks. The PF solver is based on MANA formulation and NR algorithm. The proposed PF solver does not need the existence of a DC slack bus, nor does it have network topology constraints. All possible AC/DC and DC/DC interconnections of hybrid AC/DC network are considered in the formulation. The modified IEEE 33 bus hybrid AC/DC test feeder is simulated for both radial and mesh configurations and validated through EMT simulations. The solver is also tested on larger networks to test its applicability to large-scale networks. The convergence characteristics of the MANA-NR formulation and the classical NA-NR formulation are compared on the large-scale hybrid AC/DC test networks with FS and TS at various loadings and X/R ratios. The proposed MANA-NR exhibits much better convergence characteristics than the classical NA-NR method. The MANA's unique Jacobian matrix structure resulted in a well-conditioned formulation, which increased solvability and convergence robustness. This is due to the much smaller Jacobian matrix condition number of the MANA formulation compared to the classical NA formulation. The Jacobian matrix condition number of the classical NA-NR is more than 1500 and 1800 times larger than the MANA-NR at all loading conditions where both methods converged for 167 bus and 3880 bus test networks, respectively. This formulation is also extended to add SST PF model in the formulation. The proposed MANA-NR formulation-based PF solver is robust and capable of providing an accurate solution for hybrid AC/DC networks with the flexibility and speed required for the future online smart-grid applications.

The converter models used in this study are for a positive sequence solver. However, they can be adapted and integrated into an unbalanced/multi-phase MANA formulation considering the control strategy in positive sequence. The negative sequence behavior of the converter strongly depends on the inner (current) loop control scheme and this work can be further extended for unbalanced/multi-phase AC grids by augmenting the AC/DC converters models to include various converter negative sequence control strategies. The solver can further be extended by considering the substation details of DGs and grid inverters (such as DG and grid inverter transformers) which are overlooked in the literature. It should be noted that, not only the voltage at the point of interconnection (POI) but also grid inverter and DG (if inverter-based-resource (IBR) type) voltage output can be unbalanced in an unbalanced system.

Future research can also target the optimal power flow (OPF) problem in DC and hybrid AC/DC networks.

Appendices

Appendix-A1: IEEE 33 Bus Test Feeder Line and Load Data

Branch No.	Bus (m)	Bus (n)	R (Ohm)	X (Ohm)	P_n (kW)	Q_n (kVAR)	a	b	c
1	1	2	0.0922	0.0477	100	60	0.025	0.51	0.465
2	2	3	0.4930	0.2511	90	40	0.31	0.345	0.345
3	3	4	0.3660	0.1864	120	80	0.11	0.69	0.20
4	4	5	0.3811	0.1941	60	30	1	0	0
5	5	6	0.8190	0.7070	60	20	0.20	0.70	0.10
6	6	7	0.1872	0.6188	200	100	0.10	0.20	0.70
7	7	8	1.7114	1.2351	200	100	1	0	0
8	8	9	1.0300	0.7400	60	20	0.51	0.465	0.025
9	9	10	1.0400	0.7400	60	20	0.20	0.11	0.69
10	10	11	0.1966	0.0650	45	30	1	0	0
11	11	12	0.3744	0.1238	60	35	0	0	1
12	12	13	1.4680	1.1550	60	35	0	0	1
13	13	14	0.5416	0.7129	120	80	0	0	1
14	14	15	0.5910	0.5260	60	10	0	0	1
15	15	16	0.7463	0.5450	60	20	0.20	0.15	0.65
16	16	17	1.2890	1.7210	60	20	0.345	0.31	0.345
17	17	18	0.7320	0.5740	90	40	0.025	0.51	0.465
18	2	19	0.1640	0.1565	90	40	0	0	1
19	19	20	1.5042	1.3554	90	40	0.40	0.05	0.55
20	20	21	0.4095	0.4784	90	40	0.51	0.465	0.025
21	21	22	0.7089	0.9373	90	40	0.05	0.55	0.40
22	3	23	0.4512	0.3083	90	50	0	0	1
23	23	24	0.8980	0.7091	420	200	0.10	0.20	0.70
24	24	25	0.8960	0.7011	420	200	0.40	0.05	0.55
25	6	26	0.2030	0.1034	60	25	0	0	1
26	26	27	0.2842	0.1447	60	25	0.51	0.465	0.025
27	27	28	1.0590	0.9337	60	20	0.20	0.70	0.10
28	28	29	0.8042	0.7006	120	70	1	0	0
29	29	30	0.5075	0.2585	200	600	0.51	0.465	0.025
30	30	31	0.9744	0.9630	150	70	0.20	0.11	0.69
31	31	32	0.3105	0.3619	210	100	0	0	1
32	32	33	0.3410	0.5302	60	40	0	0	1

Appendix-A2: IEEE 33 Bus Test Feeder Tie Lines Data

Bus (m)	**Bus (n)**	**R (Ohm)**	**X (Ohm)**
8	21	0.7325	0.5745
9	15	0.8047	0.7016
12	22	1.4688	1.1557
18	33	0.5436	0.7139
25	29	0.5911	0.5268

Appendix-B1: Test Network 3 Transformer and Generator Data

Transformer Data			
Number	Connection	Rating	Voltage
T_1-T_6	Y:Y	150MVA	400/154 kV
T_7	D:Y	175MVA	154/400 kV
T_8	D:Y	45MVA	10.5/154 kV
T_9	D:Y	25MVA	6.3/154 kV
T_{10}	D:Y	45MVA	10.5/154 kV
T_{11}	D:Y	65MVA	10.5/154 kV

Generator Data	
Number	Rating
G_1	30 MW
G_2	20 MW
G_3	35 MW
G_4	50 MW
G_5	140 MW

Appendix-B2: Test Network 3 Load Data

Bus Name	**P (MW)**	**Q (Mvar)**	**Bus Name**	**P (MW)**	**Q (Mvar)**
BORCA	4	2	TIREBOLU_2	17	6
HOPA	16	6	GIRESUN	23	6
ARDESEN	8	2	ORDU	29	3
CAYELI	15	2	UNYE	31	3
IYIDERE	13	5	FATSA	14	6
RIZE	16	6	ARSIN	10	4
ORDU	21	6	CARSAMBA	26	4
TRABZON	32	12	DOGANKENT	8	3

Appendix-B3: Test Network 3 Line Data

From Bus	To Bus	R (*pu*)	X (*pu*)
MURATLI	BORCKA	0.00318	0.0251
MURATLI	BORCKA	0.00352	0.02661
HOPA	MURATLI	0.00575	0.04534
HOPA	MURATLI	0.00575	0.04534
ARDESEN	HOPA	0.01757	0.08231
ARDESEN	HOPA	0.01757	0.08231
ARDESEN	CAYELI	0.00924	0.04137
ARDESEN	RIZE	0.01288	0.0614
ARDESEN	CAYELI	0.00924	0.04137
IYIDERE	RIZE	0.00801	0.03757
CAYELI	IYIDERE	0.01254	0.05979
ARSIN	IYIDERE	0.01382	0.06349
IYIDERE	TRABZON	0.01865	0.08751
ARSIN	TRABZON	0.0063	0.0283
ARSIN	TIREBOLU_2	0.03361	0.15774
ARSIN	TIREBOLU_1	0.03361	0.15774
ORDU	TIREBOLU_1	0.0311	0.14564
TIREBOLU_2	TRABZON	0.04756	0.14938
TIREBOLU_2	KURTUN	0.00915	0.07222
GIRESUN	TIREBOLU_1	0.01254	0.05979
GIRESUN	ORDU	0.02653	0.08332
ORDU	FATSA	0.01213	0.05683
ORDU	UNYE	0.01855	0.08687
CARSAMBA	FATSA	0.02946	0.138
CARSAMBA	UNYE	0.00171	0.00549
DOGANKENT	TORTUL	0.00303	0.02798

Reference

[1] T. McNichol, *AC/DC: The savage tale of the first standards war*. John Wiley & Sons, 2011.

[2] P. Fairley, "DC versus AC: The second war of currents has already begun [in my view]," *IEEE Power and energy magazine,* vol. 10, no. 6, pp. 104-103, 2012.

[3] D. Van Hertem, O. Gomis-Bellmunt, and J. Liang, *HVDC grids: for offshore and supergrid of the future*. John Wiley & Sons, 2016.

[4] D. Van Hertem and M. Ghandhari, "Multi-terminal VSC HVDC for the European supergrid: Obstacles," *Renewable and sustainable energy reviews,* vol. 14, no. 9, pp. 3156-3163, 2010.

[5] K. Nandini, N. Jayalakshmi, and V. K. Jadoun, "An overview of DC Microgrid with DC distribution system for DC loads," *Materials Today: Proceedings,* vol. 51, pp. 635-639, 2022.

[6] A. H. Sabry, A. H. Shallal, H. S. Hameed, and P. J. Ker, "Compatibility of household appliances with DC microgrid for PV systems," *Heliyon,* vol. 6, no. 12, p. e05699, 2020.

[7] S. Sivakumar, M. J. Sathik, P. Manoj, and G. Sundararajan, "An assessment on performance of DC–DC converters for renewable energy applications," *Renewable and Sustainable Energy Reviews,* vol. 58, pp. 1475-1485, 2016.

[8] E. Rodriguez-Diaz, J. C. Vasquez, and J. M. Guerrero, "Intelligent DC homes in future sustainable energy systems: When efficiency and intelligence work together," *IEEE Consumer Electronics Magazine,* vol. 5, no. 1, pp. 74-80, 2015.

[9] K. Aanesen, S. Heck, and D. Pinner, "Solar power: Darkest before dawn," *McKinsey on Sustainability & Resource Productivity,* vol. 14, 2012.

[10] M. M. Mahmoud, "Economic Applications for LED Lights in Industrial Sectors," in *Light-Emitting Diodes and Photodetectors-Advances and Future Directions*: IntechOpen, 2021.

[11] A. S. Kamat, R. Khosla, and V. Narayanamurti, "Illuminating homes with LEDs in India: Rapid market creation towards low-carbon technology transition in a developing country," *Energy Research & Social Science,* vol. 66, p. 101488, 2020.

[12] IEC. "LVDC: Electricity for the 21st Century, Technical Report 2018." https://www.iec.ch/basecamp/lvdc-electricity-21stcentury (accessed 6/2, 2023).

[13] J. M. Maza-Ortega, J. M. Mauricio, M. Barragán-Villarejo, C. Demoulias, and A. Gómez-Expósito, "Ancillary services in hybrid AC/DC low voltage distribution networks," *Energies,* vol. 12, no. 19, p. 3591, 2019.

[14] A. Sannino, G. Postiglione, and M. H. Bollen, "Feasibility of a DC network for commercial facilities," in *Conference Record of the 2002 IEEE Industry Applications Conference. 37th IAS Annual Meeting (Cat. No. 02CH37344)*, 2002, vol. 3: IEEE, pp. 1710-1717.

[15] D. J. Hammerstrom, "AC versus DC distribution systemsdid we get it right?," in *2007 IEEE Power Engineering Society General Meeting*, 2007: IEEE, pp. 1-5.

[16] F. Dastgeer, H. E. Gelani, H. M. Anees, Z. J. Paracha, and A. Kalam, "Analyses of efficiency/energy-savings of DC power distribution systems/microgrids: Past, present and future," *International Journal of Electrical Power & Energy Systems,* vol. 104, pp. 89-100, 2019.

[17] J.-Y. Jeon, J.-S. Kim, G.-Y. Choe, B.-K. Lee, J. Hur, and H.-C. Jin, "Design guideline of DC distribution systems for home appliances: Issues and solution," in *2011 IEEE International Electric Machines & Drives Conference (IEMDC)*, 2011: IEEE, pp. 657-662.

[18] D. Salomonsson and A. Sannino, "Low-voltage DC distribution system for commercial power systems with sensitive electronic loads," *IEEE Transactions on Power Delivery,* vol. 22, no. 3, pp. 1620-1627, 2007.

[19] M. E. Baran and N. R. Mahajan, "DC distribution for industrial systems: opportunities and challenges," *IEEE transactions on industry applications,* vol. 39, no. 6, pp. 1596-1601, 2003.

[20] R. Majumder, "Aggregation of microgrids with DC system," *Electric Power Systems Research,* vol. 108, pp. 134-143, 2014.

[21] W. Pei, W. Deng, X. Zhang, H. Qu, and K. Sheng, "Potential of using multiterminal LVDC to improve plug-in electric vehicle integration in an existing distribution network," *IEEE Transactions on Industrial Electronics,* vol. 62, no. 5, pp. 3101-3111, 2014.

[22] C. Hamilton *et al.*, "System architecture of a modular direct-DC PV charging station for plug-in electric vehicles," in *IECON 2010-36th Annual Conference on IEEE Industrial Electronics Society*, 2010: IEEE, pp. 2516-2520.

[23] D. Taylor, "Plugging in: Power sockets, standards and the valencies of national habitus," *Journal of Material Culture,* vol. 20, no. 1, pp. 59-75, 2015.

[24] M. Amin, Y. Arafat, S. Lundberg, and S. Mangold, "Low voltage DC distribution system compared with 230 V AC," in *2011 IEEE electrical power and energy conference*, 2011: IEEE, pp. 340-345.

[25] K. Techakittiroj and V. Wongpaibool, "Co-existance between AC-distribution and DC-distribution: in the view of appliances," in *2009 Second International Conference on Computer and Electrical Engineering*, 2009, vol. 1: IEEE, pp. 421-425.

[26] W. Yu, J.-S. Lai, H. Ma, and C. Zheng, "High-efficiency DC–DC converter with twin bus for dimmable LED lighting," *IEEE Transactions on Power Electronics,* vol. 26, no. 8, pp. 2095-2100, 2011.

[27] E. Rodriguez-Diaz, M. Savaghebi, J. C. Vasquez, and J. M. Guerrero, "An overview of low voltage DC distribution systems for residential applications," in *2015 IEEE 5th International Conference on Consumer Electronics-Berlin (ICCE-Berlin)*, 2015: IEEE, pp. 318-322.

[28] G. Lazaroiu and D. Zaninelli, "A control system for dc arc furnaces for power quality improvements," *Electric power systems research,* vol. 80, no. 12, pp. 1498-1505, 2010.

[29] E. Heitz, "DC electrochemical methods," *CORROSION TECHNOLOGY-NEW YORK AND BASEL-,* vol. 22, p. 435, 2006.

[30] P. S. Maniscalco, V. Scaini, and W. E. Veerkamp, "Specifying DC chopper systems for electrochemical applications," *IEEE Transactions on Industry Applications,* vol. 37, no. 3, pp. 941-948, 2001.

[31] C. Xu and K. W. E. Cheng, "A survey of distributed power system—AC versus DC distributed power system," in *2011 4th International Conference on Power Electronics Systems and Applications*, 2011: IEEE, pp. 1-12.

[32] G. AlLee and W. Tschudi, "Edison redux: 380 Vdc brings reliability and efficiency to sustainable data centers," *IEEE Power and Energy Magazine,* vol. 10, no. 6, pp. 50-59, 2012.

[33] N. Rasmussen and J. Spitaels, "A quantitative comparison of high efficiency ac vs. dc power distribution for data centers," *white paper,* vol. 127, 2007.

[34] P. Wang, L. Goel, X. Liu, and F. H. Choo, "Harmonizing AC and DC: A hybrid AC/DC future grid solution," *IEEE Power and Energy Magazine,* vol. 11, no. 3, pp. 76-83, 2013.

[35] M. Tabari and A. Yazdani, "A DC distribution system for power system integration of plug-in hybrid electric vehicles," in *2013 IEEE Power & Energy Society General Meeting*, 2013: IEEE, pp. 1-5.

[36] B. E. Noriega, R. T. Pinto, and P. Bauer, "Sustainable DC-microgrid control system for electric-vehicle

charging stations," in *2013 15th European Conference on Power Electronics and Applications (EPE)*, 2013: IEEE, pp. 1-10.

[37] B. N. W. Feng and R. Brown. "B. N. Wei Feng, Rich Brown. "Direct Current (DC) Buildings & Smart Grid." https://www.energy.gov/sites/default/files/2018/06/f52/94150c_Brown_050118-1100.pdf (accessed 3/10, 2022).

[38] D. MANDELL. "Three (3) "Whys" of DC Lighting." https://energycentral.com/c/em/three-3-%E2%80%9Cwhys%E2%80%9D-dc-lighting (accessed 5/10, 2022).

[39] D. L. Gerber, V. Vossos, W. Feng, C. Marnay, B. Nordman, and R. Brown, "A simulation-based efficiency comparison of AC and DC power distribution networks in commercial buildings," *Applied Energy,* vol. 210, pp. 1167-1187, 2018.

[40] D. Salomonsson and A. Sannino, "Load modelling for steady-state and transient analysis of low-voltage DC systems," *IET Electric Power Applications,* vol. 1, no. 5, pp. 690-696, 2007.

[41] K. Sun *et al.*, "Operation and control for multi-voltage-level dc network to improve the utilization rate of renewable energies," in *2017 IEEE Industry Applications Society Annual Meeting*, 2017: IEEE, pp. 1-8.

[42] E. Toklu, "Overview of potential and utilization of renewable energy sources in Turkey," *Renewable Energy,* vol. 50, pp. 456-463, 2013.

[43] F. Blaabjerg, Z. Chen, and S. B. Kjaer, "Power electronics as efficient interface in dispersed power generation systems," *IEEE transactions on power electronics,* vol. 19, no. 5, pp. 1184-1194, 2004.

[44] V. A. Boicea, "Energy storage technologies: The past and the present," *Proceedings of the IEEE,* vol. 102, no. 11, pp. 1777-1794, 2014.

[45] M. Stecca, L. R. Elizondo, T. B. Soeiro, P. Bauer, and P. Palensky, "A comprehensive review of the integration of battery energy storage systems into distribution networks," *IEEE Open Journal of the Industrial Electronics Society,* vol. 1, pp. 46-65, 2020.

[46] B. Normark, A. Shivakumar, and M. Welsch, "DC Power Production and Consumption in Households," *Europe's Energy Transition,* pp. 237-248, 2017.

[47] B. H. Kenny, R. Jansen, P. Kascak, T. Dever, and W. Santiago, "Integrated power and attitude control with two flywheels," *IEEE transactions on aerospace and electronic systems,* vol. 41, no. 4, pp. 1431-1449, 2005.

[48] D. J. Becker and B. Sonnenberg, "DC microgrids in buildings and data centers," in *2011 IEEE 33rd International Telecommunications Energy Conference (INTELEC)*, 2011: IEEE, pp. 1-7.

[49] B. Stott, J. Jardim, and O. Alsaç, "DC power flow revisited," *IEEE Transactions on Power Systems,* vol. 24, no. 3, pp. 1290-1300, 2009.

[50] O. D. Montoya, L. F. Grisales-Noreña, and W. Gil-González, "Triangular matrix formulation for power flow analysis in radial DC resistive grids with CPLs," *IEEE Transactions on Circuits and Systems II: Express Briefs,* 2019.

[51] O. D. Montoya, W. Gil-González, and A. Garces, "Power flow approximation for DC networks with constant power loads via logarithmic transform of voltage magnitudes," *Electric Power Systems Research,* vol. 175, p. 105887, 2019.

[52] O. D. Montoya, L. Grisales-Noreña, D. González-Montoya, C. Ramos-Paja, and A. Garces, "Linear power flow formulation for low-voltage DC power grids," *Electric Power Systems Research,* vol. 163, pp. 375-381, 2018.

[53] O. D. Montoya, V. M. Garrido, W. Gil-González, and L. F. Grisales-Noreña, "Power flow analysis in

DC grids: two alternative numerical methods," *IEEE Transactions on Circuits and Systems II: Express Briefs,* vol. 66, no. 11, pp. 1865-1869, 2019.

[54] O. D. Montoya, "On linear analysis of the power flow equations for DC and AC grids with CPLs," *IEEE Transactions on Circuits and Systems II: Express Briefs,* vol. 66, no. 12, pp. 2032-2036, 2019.

[55] S. Sepúlveda-García, O. D. Montoya, and A. Garcés, "Power Flow Solution in Bipolar DC Networks Considering a Neutral Wire and Unbalanced Loads: A Hyperbolic Approximation," *Algorithms,* vol. 15, no. 10, p. 341, 2022.

[56] H. Li, L. Zhang, and X. Shen, "A loop-analysis theory based power flow method and its linear formulation for low-voltage DC grid," *Electric Power Systems Research,* vol. 187, p. 106473, 2020.

[57] L. F. Grisales-Noreña, O. Garzon-Rivera, C. Ramírez-Vanegas, O. Montoya, and C. Ramos-Paja, "Application of the backward/forward sweep method for solving the power flow problem in DC networks with radial structure," in *Journal of Physics: Conference Series*, 2020, vol. 1448, no. 1: IOP Publishing, p. 012012.

[58] O. D. Montoya, V. M. Garrido, W. Gil-Gonzalez, and L. F. Grisales-Noreña, "Power flow analysis in DC grids: Two alternative numerical methods," *IEEE Transactions on Circuits and Systems II: Express Briefs,* vol. 66, no. 11, pp. 1865-1869, 2019.

[59] O. D. Montoya, W. Gil-González, and A. Garcés, "A successive approximations method for power flow analysis in bipolar DC networks with asymmetric constant power terminals," *Electric Power Systems Research,* vol. 211, p. 108264, 2022.

[60] J.-O. Lee, Y.-S. Kim, and J.-H. Jeon, "Generic power flow algorithm for bipolar DC microgrids based on Newton–Raphson method," *International Journal of Electrical Power & Energy Systems,* vol. 142, p. 108357, 2022.

[61] Z. Liu *et al.*, "Further results on Newton-Raphson method in feasible power-flow for DC distribution networks," *IEEE Transactions on Power Delivery,* vol. 37, no. 2, pp. 1348-1351, 2021.

[62] A. Garcés, "On the convergence of Newton's method in power flow studies for DC microgrids," *IEEE Transactions on Power Systems,* vol. 33, no. 5, pp. 5770-5777, 2018.

[63] L. L. de Sousa and I. D. Melo, "Interval power flow analysis of microgrids with uncertainties: an approach using the second-order Taylor series expansion," *Electrical Engineering,* vol. 104, no. 3, pp. 1623-1633, 2022.

[64] K. K. Dewangan and A. K. Panchal, "Power flow analysis using successive approximation and adomian decomposition methods with a new power flow formulation," *Electric Power Systems Research,* vol. 211, p. 108190, 2022.

[65] J. Mahseredjian, S. Dennetière, L. Dubé, B. Khodabakhchian, and L. Gérin-Lajoie, "On a new approach for the simulation of transients in power systems," *Electric power systems research,* vol. 77, no. 11, pp. 1514-1520, 2007.

[66] L. Wedepohl and L. Jackson, "Modified nodal analysis: an essential addition to electrical circuit theory and analysis," *Engineering Science & Education Journal,* vol. 11, no. 3, pp. 84-92, 2002.

[67] M. V. Kirthiga and S. A. Daniel, "Computational techniques for autonomous microgrid load flow analysis," *International Scholarly Research Notices,* vol. 2014, 2014.

[68] S. Taheri and V. Kekatos, "Power flow solvers for direct current networks," *IEEE Transactions on Smart Grid,* vol. 11, no. 1, pp. 634-643, 2019.

[69] O. D. Montoya, W. Gil-González, and A. Garces, "Numerical methods for power flow analysis in DC networks: State of the art, methods and challenges," *International Journal of Electrical Power & Energy*

Systems, vol. 123, p. 106299, 2020.

[70] L. F. Grisales-Noreña, O. D. Montoya, W. J. Gil-González, A.-J. Perea-Moreno, and M.-A. Perea-Moreno, "A Comparative Study on Power Flow Methods for Direct-Current Networks Considering Processing Time and Numerical Convergence Errors," *Electronics,* vol. 9, no. 12, p. 2062, 2020.

[71] U. Ghatak and V. Mukherjee, "An improved load flow technique based on load current injection for modern distribution system," *International Journal of Electrical Power & Energy Systems,* vol. 84, pp. 168-181, 2017.

[72] M. Shakarami, H. Beiranvand, A. Beiranvand, and E. Sharifipour, "A recursive power flow method for radial distribution networks: Analysis, solvability and convergence," *International Journal of Electrical Power & Energy Systems,* vol. 86, pp. 71-80, 2017.

[73] U. Ghatak and V. Mukherjee, "A fast and efficient load flow technique for unbalanced distribution system," *International Journal of Electrical Power & Energy Systems,* vol. 84, pp. 99-110, 2017.

[74] A. Trias, "The holomorphic embedding load flow method," in *2012 IEEE Power and Energy Society General Meeting*, 2012: IEEE, pp. 1-8.

[75] S. Rao, Y. Feng, D. J. Tylavsky, and M. K. Subramanian, "The holomorphic embedding method applied to the power-flow problem," *IEEE Transactions on Power Systems,* vol. 31, no. 5, pp. 3816-3828, 2015.

[76] I. Kocar, J. Mahseredjian, U. Karaagac, G. Soykan, and O. Saad, "Multiphase load-flow solution for large-scale distribution systems using MANA," *IEEE Transactions on Power Delivery,* vol. 29, no. 2, pp. 908-915, 2013.

[77] M. E. Nassar, A. A. Hamad, M. Salama, and E. F. El-Saadany, "A novel load flow algorithm for islanded AC/DC hybrid microgrids," *IEEE Transactions on Smart Grid,* vol. 10, no. 2, pp. 1553-1566, 2017.

[78] J. Beerten, S. Cole, and R. Belmans, "Generalized steady-state VSC MTDC model for sequential AC/DC power flow algorithms," *IEEE Transactions on Power Systems,* vol. 27, no. 2, pp. 821-829, 2012.

[79] R. Chai, B. Zhang, J. Dou, Z. Hao, and T. Zheng, "Unified power flow algorithm based on the NR method for hybrid AC/DC grids incorporating VSCs," *IEEE Transactions on Power Systems,* vol. 31, no. 6, pp. 4310-4318, 2016.

[80] B. Rehman and C. Liu, "AC/DC multi-infeed power flow solution," *IET Generation, Transmission & Distribution,* vol. 13, no. 10, pp. 1838-1844, 2019.

[81] F. Yalcin and U. Arifoglu, "A new sequential AC–DC power flow algorithm for multi-terminal HVDC systems," *IEEJ Transactions on Electrical and Electronic Engineering,* vol. 12, pp. S65-S71, 2017.

[82] J. Beerten and R. Belmans, "Development of an open source power flow software for high voltage direct current grids and hybrid AC/DC systems: MATACDC," *IET Generation, Transmission & Distribution,* vol. 9, no. 10, pp. 966-974, 2015.

[83] R. D. Zimmerman, C. E. Murillo-Sánchez, and R. J. Thomas, "MATPOWER: Steady-state operations, planning, and analysis tools for power systems research and education," *IEEE Transactions on power systems,* vol. 26, no. 1, pp. 12-19, 2010.

[84] A. Pizano-Martinez, C. R. Fuerte-Esquivel, H. Ambriz-Pérez, and E. Acha, "Modeling of VSC-based HVDC systems for a Newton-Raphson OPF algorithm," *IEEE Transactions on Power Systems,* vol. 22, no. 4, pp. 1794-1803, 2007.

[85] X.-P. Zhang, "Multiterminal voltage-sourced converter-based HVDC models for power flow analysis," *IEEE Transactions on Power Systems,* vol. 19, no. 4, pp. 1877-1884, 2004.

[86] T. Smed, G. Andersson, G. Sheble, and L. Grigsby, "A new approach to AC/DC power flow," *IEEE*

Transactions on Power Systems, vol. 6, no. 3, pp. 1238-1244, 1991.

[87] M. M. Rezvani and S. Mehraeen, "Unified AC-DC Load Flow Via an Alternate AC-Equivalent Circuit," *IEEE Transactions on Industry Applications,* vol. 57, no. 6, pp. 5626-5635, 2021.

[88] H. M. Ahmed, A. B. Eltantawy, and M. Salama, "A generalized approach to the load flow analysis of AC–DC hybrid distribution systems," *IEEE Transactions on Power Systems,* vol. 33, no. 2, pp. 2117-2127, 2017.

[89] P. A. Garcia, J. Pereira, S. Carneiro, M. P. Vinagre, and F. V. Gomes, "Improvements in the representation of PV buses on three-phase distribution power flow," *IEEE Transactions on Power Delivery,* vol. 19, no. 2, pp. 894-896, 2004.

[90] M. Karimi, A. Shahriari, M. Aghamohammadi, H. Marzooghi, and V. Terzija, "Application of Newton-based load flow methods for determining steady-state condition of well and ill-conditioned power systems: A review," *International Journal of Electrical Power & Energy Systems,* vol. 113, pp. 298-309, 2019.

[91] B. Stott, "Effective starting process for Newton-Raphson load flows," in *Proceedings of the institution of electrical engineers*, 1971, vol. 118, no. 8: IET, pp. 983-987.

[92] C.-W. Liu, C.-S. Chang, J.-A. Jiang, and G.-H. Yeh, "Toward a CPFLOW-based algorithm to compute all the type-1 load-flow solutions in electric power systems," *IEEE Transactions on Circuits and Systems I: Regular Papers,* vol. 52, no. 3, pp. 625-630, 2005.

[93] B. Johnson, "Extraneous and false load flow solutions," *IEEE Transactions on Power Apparatus and Systems,* vol. 96, no. 2, pp. 524-534, 1977.

[94] W. H. Kersting, "Application of Labber Network Theory to the Solution of Three-Phase radial Load Problems," in *IEEE PES winter meeting*, 1976, vol. 76044, no. 8.

[95] D. Shirmohammadi, H. W. Hong, A. Semlyen, and G. Luo, "A compensation-based power flow method for weakly meshed distribution and transmission networks," *IEEE Transactions on power systems,* vol. 3, no. 2, pp. 753-762, 1988.

[96] B. Cetindag, I. Kocar, A. Gueye, and U. Karaagac, "Modeling of Step Voltage Regulators in Multiphase Load Flow Solution of Distribution Systems Using Newton's Method and Augmented Nodal Analysis," *Electric Power Components and Systems,* vol. 45, no. 15, pp. 1667-1677, 2017.

[97] O. S. Nduka, Y. Yu, B. C. Pal, and E. N. Okafor, "A robust augmented nodal analysis approach to distribution network solution," *IEEE Transactions on Smart Grid,* vol. 11, no. 3, pp. 2140-2150, 2019.

[98] Y. Huang, X. Ai, J. Fang, W. Yao, and J. Wen, "Holomorphic embedding approach for VSC-based AC/DC power flow," *IET Generation, Transmission & Distribution,* vol. 14, no. 25, pp. 6239-6249, 2020.

[99] P. Gonnet, S. Guttel, and L. N. Trefethen, "Robust Padé approximation via SVD," *SIAM review,* vol. 55, no. 1, pp. 101-117, 2013.

[100] Z. Javid, U. Karaagac, I. Kocar, and K. W. Chan, "Laplacian matrix-based power flow formulation for LVDC grids with radial and meshed configurations," *Energies,* vol. 14, no. 7, p. 1866, 2021.

[101] Z. Javid, U. Karaagac, and I. Kocar, "Improved Laplacian Matrix based power flow solver for DC distribution networks," *Energy Reports,* vol. 8, pp. 528-537, 2022.

[102] Z. Javid, U. Karaagac, and I. Kocar, "MANA formulation based load flow solution for DC distribution networks," *IEEE Transactions on Circuits and Systems II: Express Briefs,* 2023.

[103] Z. Javid, T. Xue, K. Ulas, and I. Kocar, "Efficient Graph Theory Based Load Flow Solver for DC Distribution Networks Considering DC/DC Converter Models," in *2022 IEEE 9th International*

Conference on Power Electronics Systems and Applications (PESA), 2022: IEEE, pp. 1-5.

[104] Z. Javid, U. Karaagac, I. Kocar, and T. Xue, "DC grid load flow solution incorporating generic DC/DC converter topologies," *Energy Reports,* vol. 9, pp. 951-961, 2023.

[105] Z. Javid, T. Xue, U. Karaagac, and I. Kocar, "Unified Power Flow Solver for Hybrid AC/DC Distribution Networks," *IEEE Transactions on Power Delivery,* 2023.

[106] Z. Javid, U. Karaagac, I. Kocar, and W. Holderbaum, "Solid-State Transformer Modelling in Power Flow Calculation," *Energy Reports,* vol. Accepted for publication, 2023.

[107] E. Acha, B. Kazemtabrizi, and L. M. Castro, "A new VSC-HVDC model for power flows using the Newton-Raphson method," *IEEE Transactions on Power Systems,* vol. 28, no. 3, pp. 2602-2612, 2013.

[108] E. Acha and L. M. Castro, "A generalized frame of reference for the incorporation of, multi-terminal VSC-HVDC systems in power flow solutions," *Electric Power Systems Research,* vol. 136, pp. 415-424, 2016.

[109] U. Vargas, A. Ramirez, and M. A. Abdel-Rahman, "Two-port network equivalent of VSC-HVDC for power flow studies," *Electric Power Systems Research,* vol. 163, pp. 430-440, 2018.

[110] M. M. Rezvani and S. Mehraeen, "A Generalized Model For Unified Ac-Dc Load Flow Analysis," in *2021 IEEE Texas Power and Energy Conference (TPEC)*, 2021: IEEE, pp. 1-6.

[111] M. El-Hawary and S. Ibrahim, "A new approach to AC-DC load flow analysis," *Electric Power Systems Research,* vol. 33, no. 3, pp. 193-200, 1995.

[112] S. Rudraraju, S. C. Srivastava, A. K. Srivastava, and N. N. Schulz, "Modeling and simulation of voltage source converter–medium-voltage DC system for stability analysis," *Electric Power Components and Systems,* vol. 39, no. 11, pp. 1134-1150, 2011.

[113] Z. Li, Y. Li, P. Wang, H. Zhu, C. Liu, and W. Xu, "Control of three-phase boost-type PWM rectifier in stationary frame under unbalanced input voltage," *IEEE transactions on power electronics,* vol. 25, no. 10, pp. 2521-2530, 2010.

[114] W. Mcmurray, "Power converter circuits having a high frequency link," ed: Google Patents, 1970.

[115] Y. Zhuang *et al.*, "A Multiport DC Solid-State Transformer for MVDC Integration Interface of Multiple Distributed Energy Sources and DC Loads in Distribution Network," *IEEE Transactions on Power Electronics,* vol. 37, no. 2, pp. 2283-2296, 2021.

[116] M. S. Mollik *et al.*, "The Advancement of Solid-State Transformer Technology and Its Operation and Control with Power Grids: A Review," *Electronics,* vol. 11, no. 17, p. 2648, 2022.

[117] G. Guerra and J. A. Martinez-Velasco, "A solid state transformer model for power flow calculations," *International Journal of Electrical Power & Energy Systems,* vol. 89, pp. 40-51, 2017.

[118] I. Syed, V. Khadkikar, and H. H. Zeineldin, "Loss reduction in radial distribution networks using a solid-state transformer," *IEEE Transactions on Industry Applications,* vol. 54, no. 5, pp. 5474-5482, 2018.

[119] J.-H. Teng, "A direct approach for distribution system load flow solutions," *IEEE Transactions on power delivery,* vol. 18, no. 3, pp. 882-887, 2003.

[120] A. Marini, S. Mortazavi, L. Piegari, and M.-S. Ghazizadeh, "An efficient graph-based power flow algorithm for electrical distribution systems with a comprehensive modeling of distributed generations," *Electric Power Systems Research,* vol. 170, pp. 229-243, 2019.

[121] T. Shen, Y. Li, and J. Xiang, "A graph-based power flow method for balanced distribution systems," *Energies,* vol. 11, no. 3, p. 511, 2018.

[122] P. Aravindhababu, S. Ganapathy, and K. Nayar, "A novel technique for the analysis of radial distribution systems," *International journal of electrical power & energy systems,* vol. 23, no. 3, pp. 167-171, 2001.

[123] T.-Y. Hsieh, T.-H. Chen, and N.-C. Yang, "Matrix decompositions-based approach to Z-bus matrix building process for radial distribution systems," *International Journal of Electrical Power & Energy Systems,* vol. 89, pp. 62-68, 2017.

[124] P. De Oliveira-De Jesus, M. Alvarez, and J. Yusta, "Distribution power flow method based on a real quasi-symmetric matrix," *Electric power systems research,* vol. 95, pp. 148-159, 2013.

[125] A. W. Cirino, H. de Paula, R. C. Mesquita, and E. Saraiva, "Cable parameter determination focusing on proximity effect inclusion using finite element analysis," in *2009 Brazilian Power Electronics Conference*, 2009: IEEE, pp. 402-409.

[126] R. Baldick, *Applied optimization: formulation and algorithms for engineering systems*. Cambridge University Press, 2006.

[127] S. Shukla, S. Balasubramanian, and M. Pavlović, "A generalized Banach fixed point theorem," *Bulletin of the Malaysian Mathematical Sciences Society,* vol. 39, no. 4, pp. 1529-1539, 2016.

[128] S. Oltra and O. Valero, "Banach's fixed point theorem for partial metric spaces," 2004.

[129] L. Ćirić, "Solving the Banach fixed point principle for nonlinear contractions in probabilistic metric spaces," *Nonlinear Analysis: Theory, Methods & Applications,* vol. 72, no. 3-4, pp. 2009-2018, 2010.

[130] J. Mahseredjian, "Simulation des transitoires électromagnétiques dans les réseaux électriques," *Édition Les Techniques de l'Ingénieur,* 2008.

[131] M. K. Singh, S. Dhople, F. Dörfler, and G. B. Giannakis, "Time-Domain Generalization of Kron Reduction," *IEEE Control Systems Letters,* vol. 7, pp. 259-264, 2022.

[132] U. Karaagac, J. Mahseredjian, O. Saad, and S. Dennetière, "Synchronous machine modeling precision and efficiency in electromagnetic transients," *IEEE transactions on power delivery,* vol. 26, no. 2, pp. 1072-1082, 2010.

[133] S. R. Sanders, J. M. Noworolski, X. Z. Liu, and G. C. Verghese, "Generalized averaging method for power conversion circuits," *IEEE Transactions on power Electronics,* vol. 6, no. 2, pp. 251-259, 1991.

[134] W. H. Press, S. A. Teukolsky, W. T. Vetterling, and B. P. Flannery, *Numerical Recipes with Source Code CD-ROM 3rd Edition: The Art of Scientific Computing*. Cambridge University Press, 2007.

[135] R. Ebrahimian and R. Baldick, "State estimator condition number analysis," *IEEE Transactions on Power Systems,* vol. 16, no. 2, pp. 273-279, 2001.